

This electronic thesis or dissertation has been downloaded from the King's Research Portal at <https://kclpure.kcl.ac.uk/portal/>



Low temperature Cu-Cu bonding by sintering Cu nanoparticles for power electronics

Zuo, Yang

Awarding institution:
King's College London

The copyright of this thesis rests with the author and no quotation from it or information derived from it may be published without proper acknowledgement.

END USER LICENCE AGREEMENT



Unless another licence is stated on the immediately following page this work is licensed

under a Creative Commons Attribution-NonCommercial-NoDerivatives 4.0 International

licence. <https://creativecommons.org/licenses/by-nc-nd/4.0/>

You are free to copy, distribute and transmit the work

Under the following conditions:

- Attribution: You must attribute the work in the manner specified by the author (but not in any way that suggests that they endorse you or your use of the work).
- Non Commercial: You may not use this work for commercial purposes.
- No Derivative Works - You may not alter, transform, or build upon this work.

Any of these conditions can be waived if you receive permission from the author. Your fair dealings and other rights are in no way affected by the above.

Take down policy

If you believe that this document breaches copyright please contact librarypure@kcl.ac.uk providing details, and we will remove access to the work immediately and investigate your claim.

**Low temperature Cu-Cu bonding by sintering
Cu nanoparticles for power electronics**



Dissertation submitted to Physics Department of King's College

London

By Yang Zuo

Supervised by:

Prof. Samjid H. Mannan

Prof. Mark Green

July 2022

Abstract

Sintered Cu interconnection for power electronics has attracted considerable interest recently. Cu nanoparticles are promising interconnection material due to low cost and superior conductivity while they readily oxidize and need special processing and storing conditions. To solve these problems, a specific in situ reduction-sintering of both CuO and Cu nanoparticles by glycerol was developed in this thesis. The proposed method produces high sintered Cu joint strength of over 20 MPa but without the need for pressurized sintering or protective gas atmospheres. Meanwhile, this thesis employs a quasi-in-situ method combining scanning electron microscopy (SEM) observation and ion beam etching to investigate the mechanism of grain growth and twin formation in the bulk sintered Cu nanoparticle structure during sintering. A novel strengthening mechanism of grain boundary (GB) shifting which eliminates the high porosity bonding interface was found. The effect of sintering conditions on the grain and pore size, porosity and strength of the sintered Cu structure and the micro-fracture mechanism of the joint were investigated. Finally, this thesis investigates the reliability of sintered Cu joint by in situ reduction-sintering process under high temperature aging in air. The complex oxidation effect on the microstructure and strength of sintered Cu structure was unraveled. Kirkendall void (K-void), a typical defect in solder alloys, is found to form along the GBs in the bulk sintered Cu during aging and results in a degradation of joint strength.

Acknowledgements

I would like to thank my research supervisor, Prof. Samjid H. Mannan and second supervisor Prof. Mark Green for their support and guidance throughout my PhD study in King's College London. I am very grateful for letting me work on such an interesting project.

My gratitude goes to Bill Luckhurst, the technical services manager physics and engineering, for training me how to use the facilities in physics department. I also thank Dr. Ben Blackburn and Ms. Jennifer Train for teaching me on using the SEM and Atomic Force Microscope (AFM). I would like to acknowledge the assistance of Ana Robador and Martin Wickham (National Physical Laboratory) on the shear test. I would like to thank Martin Vickers (Department of Chemistry, University of London) for his help on X-ray diffraction (XRD) measurement.

Also, I would like to thank China Scholarship Council for funding my PhD study. I thank my parents, wife and son for their encouragement and support during my PhD study.

Happy people often do not settle for a comfortable life, they are going for an exceptional life. If you want to be happy, live boldly, push yourself. Do not settle.

Table of Contents

Abstract	i
Acknowledgements	ii
List of Tables	vii
List of Figures	viii
Abbreviation	xiii
Chapter 1: Introduction	1
Chapter 2: Literature review	7
<i>2.1 Sintering</i>	7
<i>2.1.1 Sintering stages</i>	7
<i>2.1.2 Driving force of sintering</i>	8
<i>2.1.3 Sintering mechanism</i>	8
<i>2.2 Cu nanoparticle based sintering</i>	11
<i>2.2.1 Effect of joining conditions</i>	11
<i>2.2.2 Copper oxide prevention and removal</i>	13
<i>2.2.2.1 Oxide removal and prevention</i>	13
<i>2.2.2.2 Reducing atmospheres</i>	14
<i>2.2.2.3 Laser sintering</i>	15
<i>2.2.3 Reduction sintering of Copper oxide</i>	15
<i>2.2.4 Particle size, shape and mixture</i>	17

2.2.5 Particle Surface modification and composite.....	19
2.3 Alternatives to sintering nanoparticles	19
2.4 Summary.....	21
Chapter 3: Methodology.....	23
3.1 Treatment of Cu substrate	23
3.2 Fabrication of CuO paste and interconnect.....	23
3.3 Fabrication of Cu paste and interconnect.....	24
3.4 Fabrication of interconnect for different sintering conditions and aging test.....	25
3.5 Characterization analysis	25
3.6 Grain size and pore size/number/shape and porosity measurement.....	26
3.7 Observation of microstructure during heating and aging	28
Chapter 4: In situ reduction-sintering of CuO nanoparticle.....	29
4.1 Background	29
4.2 Objectives	30
4.3 Methods	30
4.4 Results and Discussion.....	31
4.4.1 Comparison of different reducing agents	31
4.4.2 Effect of sintering time on the microstructure	34
4.4.3 Growth behavior of cuprous oxide	39
4.4.4 Variation in shear strength and fracture mechanism of joint	41
4.5 Conclusions	43

Chapter 5: In situ reduction-sintering of Cu nanoparticle	44
5.1 Background	44
5.2 Objectives	44
5.3 Methods	45
5.4 Results and discussion.....	45
5.4.1 Growth of Cu oxide during storage in air	45
5.4.2 Characterization of reduction- sintering structure of Cu nanoparticles.....	46
5.4.3 Consolidation behavior of Cu nanoparticles during sintering.....	50
5.5 Conclusions	52
Chapter 6: Quasi-in-situ observation of the grain growth and grain boundary movement during sintering.....	53
6.1 Background	53
6.2 Objectives	54
6.3 Methods	54
6.4 Results and discussion.....	54
6.4.1 Effect of sintering temperature on microstructure	54
6.4.2 Effect of sintering duration on microstructure	56
6.4.3 Sintering mechanism and modeling.....	59
6.4.4 Fracture mechanism of joint	61
6.4.5 Grain growth during sintering	62
6.4.6 Twin growth during sintering.....	66
6.4.7 Grain boundary shifting during sintering	67

6.5 Conclusions	70
Chapter 7: Unraveling the complex oxidation effect in sintered Cu nanoparticle interconnects during high temperature aging	72
7.1 Background	72
7.2 Objectives	72
7.3 Methods	72
7.4 Results and discussion.....	73
7.4.1 Effect of aging time on microstructure	73
7.4.2 Fracture mechanism of joint	74
7.4.3 Particle coarsening mechanism.....	78
7.4.4 Void growth during aging	80
Chapter 8: Conclusions	86
8.1 In situ reduction-sintering.....	86
8.2 Grain growth mechanism during sintering	87
8.2.1 Future work suggested from chapter 6 results	88
8.3 Oxidation effect on microstructure of sintering Cu structure	88
8.3.1 Future work suggested from chapter 7 results	89
Reference	90
Appendix	106

List of Tables

Table 2. 1 Plausible values for the constants in equations	10
Table 2. 2 Comparison of different interconnection material properties [90]	22
Table 2. 3 Comparison of different interconnection processes.....	22
Table 3. 1 Experimental design and distribution of factors.....	25

List of Figures

Figure 1. 1 Typical power module packaging architecture [26]	4
Figure 2. 1 Schematic illustration of sintering process [29]	7
Figure 2. 2 Schematic illustration of different sintering mechanisms [29]	9
Figure 3. 1 Schematic illustration (a) of the bonding process. SEM images of CuO (b) and Cu (c) nanoparticles. Comparison of cross section image (d) of sintered Cu under SE and BSE mode. Representative BSE cross section image (e) of sintered Cu structure for grain size measurement and corresponding converted binary image for porosity measurement. BSE cross section image (f) of interface for porosity measurement.....	24
Figure 4. 1 Thermal analysis of (a) ethylene glycol and CuO nanoparticle with and without ascorbic acid, PEG (b) and glycerol (c) respectively with and without CuO	32
Figure 4. 2 Morphology and EDS results of reduced Cu particle by ascorbic acid at 135 °C (a), PEG at 320 °C (b) and glycerol at 220 °C (c).....	33
Figure 4. 3 Morphology and size distribution of reduced Cu particle by glycerol at 200 °C (a), 210 °C (b), 220 °C (c) and 230 °C (d). Required reduction times are shown in figure	34
Figure 4. 4 XRD patterns (a) of fracture surfaces of joints with different mass ratios of CuO nanoparticle to glycerol, XRD patterns (b) and images (c) of fracture surfaces and shear strengths (d) of (3.5:6.5) joints for different bonding time. (Shear tests were performed in five replicates).....	36
Figure 4. 5 SEM fracture surface images of joints for 15 min (a), 20 min (b), 40 min (c) and 80 min (d).....	37
Figure 4. 6 SEM cross section images of joints bonded for 15 min (a, b, c) and 40 min (d, e, f, g, h), as well as corresponding EDS results (i)	38

Figure 4. 7 SEM images of interfaces between Cu particles and between Cu particle and disc for 15 min (a, e), 20 min (b, f), 40 min (c, g) and 80 min (d, h). Comparison of oxide thickness between 20 min (i), 40 min (j), 80 min (k) and 240 min (l)	40
Figure 4. 8 SEM images of fractures between Cu particle and disc (a, b), and between Cu particles (c, d), and corresponding schematic illustration of fracture mode.....	42
Figure 5. 1 XRD patterns (a) of Cu nanoparticles before and after exposure for different weeks. TEM image of Cu nanoparticles exposed for: (b) 0wk, (c) 1wk, (d) 2wk, (e) 6wk. (Inset image is Cu nanoparticles treated by acid).....	46
Figure 5. 2 Thermal analysis (a) of glycerol and ethylene glycol with/without CuO nanoparticle. XRD patterns (b) of fracture surfaces of joints with different mass ratios of Cu nanoparticle to glycerol.....	47
Figure 5. 3 SEM fracture surface of joints by glycerol and Cu nanoparticles exposed for (a, d) 0wk, (b, e) 1wk, (c) 2wk, (f) 6wk	48
Figure 5. 4 Shear strengths (a) of joints by gly and eth and XRD patterns (b) of joints fracture surface. (Shear tests were performed in five replicates)	49
Figure 5. 5 SEM cross section images of joints by glycerol (a, b) and ethylene glycol (c, d) mixed with 0wk exposure Cu nanoparticles, respectively.....	50
Figure 5. 6 TEM images of consolidation behavior of Cu nanoparticles of 0wk (a-h) and 2wk (i-k) during air-sintering	51
Figure 6. 1 XRD patterns (a) of Cu nanoparticles before and after reduction. Variation in porosity of bulk sintered Cu structure and interface (b), pore size/number and grain size of the bulk sintered structure and shear strength of joints (c) due to different temperatures (each for 5 min). Corresponding SEM cross section (d-g) and fracture surface images (h-k) of joints. (SEM cross section images of three replicates were used for measurement and shear tests were performed in five replicates)	56

Figure 6. 2 Variation in pore size/number and porosity of the bulk sintered Cu structure and interface (a), and grain size of the bulk sintered structure and shear strength of joints (b) due to different time at 220 °C and 310 °C. Corresponding SEM fracture surface images (c-h) of joints. Comparison of sintered structure at 220 °C/20 min (i) and 310 °C/10 min (j). (SEM cross section images of three replicates were used for measurement and shear tests were performed in five replicates).....58

Figure 6. 3 Schematic illustration (a) of two particle sintering model and comparison (b) of bulk sintered structure porosity of experimental results and modeling prediction due to different diffusion method ($0.1a-0.4a$ represent the diffusion thickness δ).....60

Figure 6. 4 Representative SEM fracture surface image of joint bonded at 220 °C for 20 min. Areas on Cu substrate: (a), (b) and (c), corresponding areas on Cu die: (d), (e) and the inset of (c). Representative SEM fracture image of joint cross section (f)62

Figure 6. 5 Time sequences of SEM observation showing sintering of Cu nanoparticles at 220 °C (a-b) and 310 °C (c-d). Grain size and boundary remain unchanged after heating and only twin (T) I and grain (II) in (a1) grows a little63

Figure 6. 6 Sequence of SEM observation showing sintering of Cu nanoparticles at elevated temperature (each for 5min). Grains with different orientation (a) as indicated by different brightness undergo orientation unification during coalescences, incomplete orientation unification causes twinning (b), larger grains (c-d) assimilate smaller grains64

Figure 6. 7 Twin percentage (a-b) in sintered Cu for different conditions. Sequence of SEM observation showing sintering of Cu nanoparticles (c-e) at elevated temperature (each for 5min). Twinning occurs in the assimilation of grains by twin particle (c). Twin forms (d-e) during coalescence due to incomplete orientation unification.....67

Figure 6. 8 Sequence of SEM observation showing the bonding interface at different temperature for 5min (a-b) and at 220 °C for different time (c-d). GB barely moves after heating and only GB in (b1) moves a little. GBs in (a1, c1 and d1) move away from the initial interface towards the sintered Cu side during early sintering stage.....68

Figure 6. 9 Representative SEM images (a) of the bonding interface showing GB moves towards Cu die side. Time sequences of SEM observation (b) showing the bonding interface at 310 °C, SEM fracture surface image (c) of corresponding joint after drop test. GB in (b1) moves away from voids after heating and fracture in (c) exactly appears at the GB not the initial bonding interface..... 70

Figure 7. 1 Variation in oxidation area (a) of joint and corresponding oxygen content (b), porosity and grain size and pore size/number of bulk sintered Cu (c) and shear strength of joints (d) due to different aging times. (SEM cross section images of three replicates were used for measurement and shear tests were performed in five replicates) 74

Figure 7. 2 SEM fracture surface images of joint before (a, b) and after (c, d) aging at 200 °C for 100 h.....75

Figure 7. 3 Representative SEM cross section images of joint before (a-c) and after (d-h) aging. Corresponding EDS mapping result (d1) of image (d) and P in (a), (e) and (g) represents porosity..... 77

Figure 7. 4 SEM fracture surface images (a-c) and porosity (d) of loose sintered areas for different aging times. SEM fracture surface images of joint aged for 100 h (e-f) and 500 h (g-h). Areas on Cu die: (e-e2) and (g-g2), corresponding areas on Cu substrate: (f-f2) and (h-h2)..... 79

Figure 7. 5 Schematic illustration of the coarsening process of sintered Cu structure... 80

Figure 7. 6 Time sequences of SEM observation showing the formation of void (a, c, d) and oxide (b) in sintered Cu structure during aging. Representative SEM image of joint

cross section showing the void line (e) along the GBs after aging for 24 h. Corresponding EDS mapping (b3) and (f) of image (b1) and (d2), respectively	81
Figure 7. 7 SEM images of joint cross section before (a) and after aging for 24 h (b) and 100 h (c). Variation in pore number (d) of sintered Cu due to different aging times and representative SEM cross section images of joint after aging for 100 h (e) and 500 h (f)	82
Figure 7. 8 Representative BSE cross section image (a) of sintered Cu before and after etching. Schematic illustration (b) of the Kirkendall void formation	83

Abbreviation

Grain boundary (GB)

Kirkendall void (K-void)

Wide-bandgap semiconductors (WBG)

Intermetallic compound (IMC)

Transient liquid phase (TLP)

Direct Cu-Cu bonding (DCB)

Electro-chemical migration resistance (EM)

Polyethylene glycol (PEG)

Differential scanning calorimetry (DSC)

X-ray diffraction (XRD)

Scanning electron microscopy (SEM)

Energy dispersive X-ray spectroscopy (EDS)

Back scattered electron (BSE)

Secondary electron (SE)

Transmission electron microscope (TEM)

Pore number (PN)

Intermediate (IM)

Reducing paste (gly)

Non-reducing paste (eth)

Chapter 1: Introduction

The present silicon (Si) technology is reaching the Si material's theoretical limits and fails to meet the requirements of recent developmental power electronics, such as higher breakdown voltages, switching frequencies, efficiency, and reliability. To overcome these limitations, new semiconductor materials for power device applications are needed. Wide-bandgap semiconductors (WBG) such as silicon carbide (SiC) gallium nitride (GaN), and diamond are emerging as a promising candidate to replace the silicon technology and take power electronics performance to the next level [1]. WBG semiconductors can be used to build significantly smaller-sized components but with comparable performance to the silicon semiconductor due to their low power losses and high switching frequency. The wide band gap and high thermal conductivity allow WBG devices to be operated at temperatures over 200 °C higher than silicon. Therefore, this new technology is of particular interest for the fields ranging from aircraft, electric vehicle, deep oil/gas extraction, and space exploration where high temperature power electronics are required [2, 3]. Furthermore, the urgent demand for electric or hybrid electric vehicles enhances the significance of high power electronics in these vehicles, where the electronics needs to operate in harsh environment, with the most detrimental condition being high temperature. However, the current lead-free solders fail to satisfy the packaging requirement of these WBG based power devices due to their intrinsic low melting point, low creep resistance and weak intermetallic compound (IMC) interface [4]. The next generation of lead-free interconnection material is required to survive at high temperature over 200 °C and possess good conductivity and bonding strength.

High temperature packaging techniques are key for the widespread use of WBG based power electronics and other industrial components and assemblies which require a high level of quality and reliability. High-lead (Pb) solders such as Pb–5Sn and Pb–10Sn have been the most common high temperature solders due to their high operating temperature over 300 °C.

However, the usage of Pb has proven to be harmful to human health and environment. In order to meet the European restriction of hazardous substances directives, Pb was restricted to be used in electrical and electronic and development of high temperature lead-free solders is needed [5, 6]. Au-Sn, Au-Ge, Zn-Al and Bi based solder alloys have attracted considerable interest recently, but there are limitations for these solders (i.e. low conductivity of Bi based solders and high cost of Au based solders). Meanwhile, high melting temperature solders require a higher processing temperature, which is detrimental to the polymer that being used as dielectric materials in the substrate. This high processing temperature will also result in higher manufacturing cost and high thermal stress on the components after the soldering process [7]. Therefore, a specific soldering method that could use the current soldering temperature while withstand a high operating temperature needs to be established.

Transient liquid phase (TLP) bonding is an alternative process for joining of power electronics [8, 9]. During this bonding process, the liquid phase is transiently formed at the bonding interface between the interlayer metal and base material. Interdiffusion results in the liquid phase being converted to intermetallics. The subsequent isothermal solidification results in a bond that has a higher melting point than the bonding temperature [10]. This bonding technique involves complete consumption of low-melting interlayer and formation of high-melting IMC. TLP bonding materials can be widely classified into Sn and In based solders, such as Ni-Sn, Cu-Sn, Au-Sn, Au-In and Ag-In. Although some of these alloys have already been used in manufacturing, they suffer from various problems. For example, Au-Sn, Au-In and Ag-In have cost issues, Cu-Sn has a problem of oxidation and the formation of brittle IMCs (Cu_6Sn_5 and Cu_3Sn) which could reduce the joint reliability [11, 12], and Ni-Sn has poor conductivity [13]. Meanwhile, the different diffusion rates of interdiffusing metals could lead to Kirkendall void formation [14, 15], which is a common problem with this type of solder joint.

Sintering of nanoparticles such as Ag or Cu is an alternative process to achieve reliable interconnections with low processing temperature but high service temperature. Ag nanoparticles have excellent conductivity and good oxidation resistance; a strong Ag joint with high thermal reliability can be achieved in the ambient atmosphere [16]. However, Ag, as one of the more expensive metals, is less attractive for wide scale use. Cu nanoparticles seem to be more promising than Ag due to their comparable conductivity but high abundance and electrochemical migration resistance (EM). The main problem of Cu nanoparticles is the ease of oxidation, which causes difficulty in the Cu joining process and degrades the merit of Cu nanoparticles. Currently, high sintered Cu joint strength requires special processing conditions (i.e. high temperature and pressure, protective atmosphere and nanoparticle pre-treatment), and special storing conditions are also necessary to prevent the Cu oxidation prior to bonding. The correlation of joint strength with sintering conditions and initial particle size or shape has been well studied [17-19] and summarized by Chen and Siow [4]. However, these works are short of in-depth research linking the mechanism of sintering, the sintering conditions and the sintered structure characteristics (i.e. porosity, grain size and strength). Investigation of grain growth during Cu nanoparticle sintering will provide insight into the strengthening mechanism of the sintered structure. Although considerable sintered Cu joint strength has been achieved in many studies [20-25], the reliability of Cu joint under high temperature is less widely reported. Cu nanoparticles suffer from a severe oxidation issue under high temperature ambient conditions, which decreases the joint reliability and can even cause failure. Understanding of the oxidation process and the relevant effect on the microstructure and strength of sintered structure is paramount for the design and fabrication of sintered Cu joint.

The main themes of this thesis are:

- 1). Developing a specific Cu nanoparticle bonding technique with ease of processing (i.e. eliminating the use of sintering pressure or protective atmosphere).

- 2). Investigating the effect of sintering conditions on grain and pore size, porosity and strength of the sintered Cu structure.
- 3). Exploring the mechanism of grain growth in the sintered Cu structure during sintering.
- 4). Investigating the sintered Cu joint reliability during high temperature aging and unravelling the mechanism of oxidation and the relevant effect on the microstructure and strength of the sintered Cu structure.

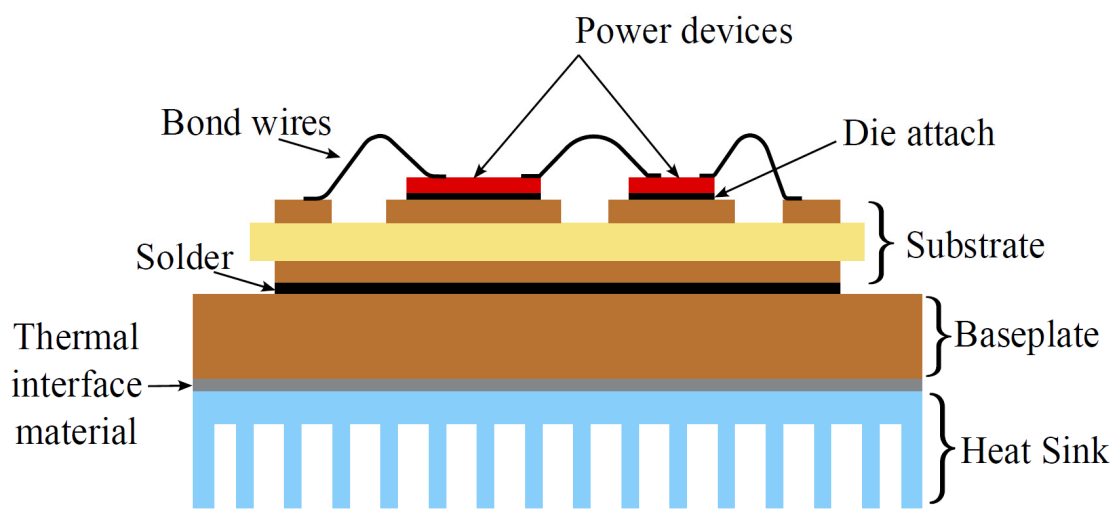


Figure 1. 1 Typical power module packaging architecture [26]

This thesis has nine chapters in the sequence: Chapter 1 Introduction; Chapter 2 Literature Review; Chapter 3 Methodology; Chapter 4 In situ reduction-sintering of CuO nanoparticle; Chapter 5 In situ reduction-sintering of Cu nanoparticle; Chapter 6 Quasi-in-situ observation of the grain growth and grain boundary movement during sintering; Chapter 7 Unraveling the complex oxidation effect in sintered Cu nanoparticle interconnects during high temperature aging; and Chapter 8 Conclusions and Future Work.

Chapter 2 explains the sintering mechanism in detail, including the sintering stages, driving forces and different diffusion paths. This chapter also introduces the theories of Cu nanoparticle based joining. First it introduces the possible methods to improve sintered Cu joint properties

and discusses the current limitations of this technology. After that, it reviews the popular ways to solve the oxidation issue of Cu nanoparticles. Next this chapter describes the alternatives to sintering of Cu nanoparticles and the advantages and disadvantages of various bonding techniques. Finally, it summarizes the different bonding methods in Cu nanoparticle based joining and their limitation and also gives the possible solutions.

Chapter 3 describes the methodology, including the paste and joint sample fabrication, grain and pore size, oxygen content, oxidation area and joint strength measurement, and details of characterization analysis (i.e. XRD, DSC and SEM).

Chapter 4 introduces an in situ reduction-sintering process of CuO nanoparticles and investigates the microstructure and strength of joint by this method and discusses the merits of this process. The morphological evolution of Cu oxide during a longer sintering duration is presented.

Chapter 5 shows a similar in situ reduction-sintering process of Cu nanoparticles but a different sintered Cu microstructure compared to CuO. The morphological evolution of Cu oxide during storage in air is also presented.

Chapter 6 presents a quasi-in-situ observation of the grain growth in sintered Cu structure (refer to chapter 5) during sintering and explain the mechanism of grain growth and twin formation. This chapter also shows in-depth research linking the mechanism of sintering, the sintering conditions and the sintered structure characteristics (i.e. grain and pore size, porosity and strength). A specific strengthening mechanism of GB shifting is revealed.

Chapter 7 investigate the reliability of sintered Cu joint (refer to chapter 5) by in situ reduction-sintering method during high temperature aging and discusses the complex oxidation effect on the microstructure and strength of sintered Cu structure. Both oxidation enhancement

and deterioration on joint property are found. A novel mechanism of oxidation mediated nanoscale Kirkendall void is unravelled.

Chapter 8 is the summary and conclusion of this thesis. This chapter reviews the results of other chapters and discuss the main advances that this work makes to the field of Cu nanoparticle based joining. Possible directions for future work are presented.

Chapter 2: Literature review

2.1 Sintering

Sintering is a traditional heat treatment in which a powder or a porous material is converted into a useful article with required microstructure and property via mass transport. The sintering process typically starts with fine powder which is first compacted into a porous green body, and then heated at high temperature so that the sintering neck can form at the interface of contacted particles and then these particles would coalesce together. This process leads to the densification of materials that is accompanied by pore shrinkage and grain growth and results in a dense component having elevated mechanical, thermal and electrical properties [27].

2.1.1 Sintering stages

The whole sintering process can be divided into three stages - initial, intermediate and final stage as shown in **Fig. 2. 1**. The initial stage is characterized by the neck formation between contacted particles. During the intermediate stage, the grain starts to grow and reduction of pore volume and significant densification (up to 90% of the theoretical density) takes place. The final stage begins when the pores pinch off and become isolated and spherical at the grain corners. The pores shrink continuously in this stage and may disappear altogether when final densification is achieved [28].

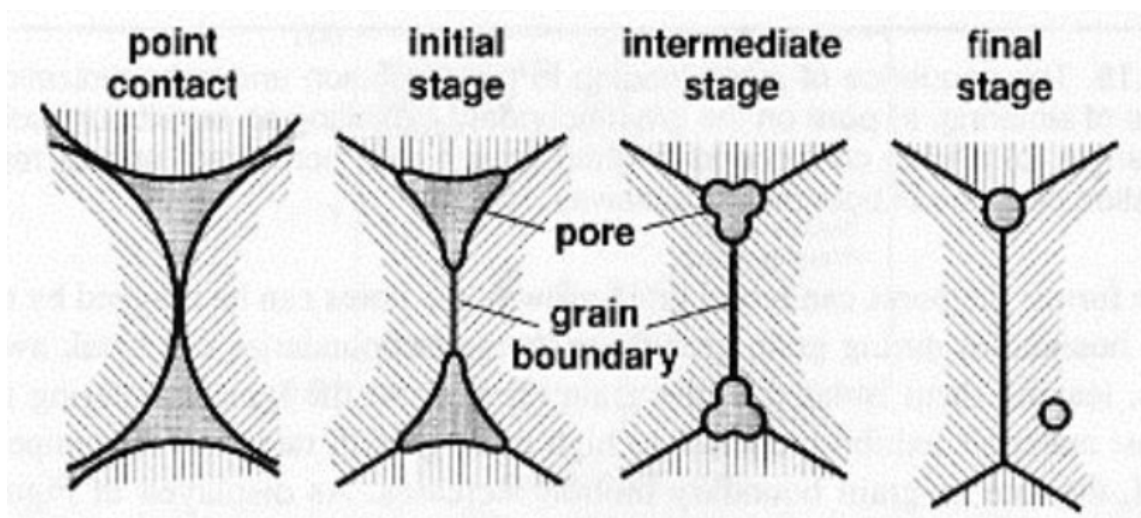


Figure 2. 1 Schematic illustration of sintering process [29]

Sintering can be classified as solid-state and liquid-phase sintering. In solid-state sintering, the joining of particles and densification of the powder compact are achieved by solid-state diffusion of atoms below the melting point of a material. Liquid-phase sintering occurs when a liquid phase is present in the powder compact during sintering [30, 31]. In sintering of Cu nanoparticles, organic solvent serves as the dispersing or reducing agent and needs to be removed prior to sintering as the organic residue would hinder the coalescence of Cu nanoparticles. Therefore, solid-state sintering dominates during Cu nanoparticle sintering.

2.1.2 Driving force of sintering

The driving force of sintering is the reduction in the total interfacial energy, which occurs via densification and grain growth. The sintering process can be accelerated by applying an external pressure or force. Generally, the total surface energy of a powder compact can be expressed as $\gamma \cdot A$, where γ is the specific surface energy and A is the total surface area of the compact. The driving force related to the interface energy is [28]:

$$\Delta G = \Delta\gamma \cdot A + \gamma \cdot \Delta A \quad (1)$$

where $\Delta\gamma$ and ΔA are the change in surface energy and surface area per unit area, respectively. Two processes of densification and coarsening will occur during sintering. For the coarsening process, a decreasing surface area will result in the reduction in energy, while for the densification, the energy reduction is caused by the replacement of surfaces by GBs as the energy of GBs is usually lower than the surface energy. Meanwhile, some local driving forces also apply during sintering, such as pressure from the curvature of particle surface and vapour pressure difference.

2.1.3 Sintering mechanism

Sintering occurs by diffusion of atoms along different paths through the microstructure, which is driven by the reduction of chemical potential. Matter is transported from regions of higher chemical potential to regions of lower chemical potential. The different paths that atoms

move during sintering is defined as the sintering mechanism and the six common mechanisms are described below and shown schematically in **Fig. 2. 2**.

1. Surface diffusion: diffusion of atoms along the particle surface.
2. Lattice diffusion from the surface: atoms from the surface diffuse through the lattice.
3. Vapor transport: evaporation of atoms from the surface which condense on a different surface.
4. GB diffusion: atoms diffuse along the GB.
5. Lattice diffusion from the GB: atoms from the GB diffuse through the lattice.
6. Plastic flow: dislocation motion causes flow of matter.

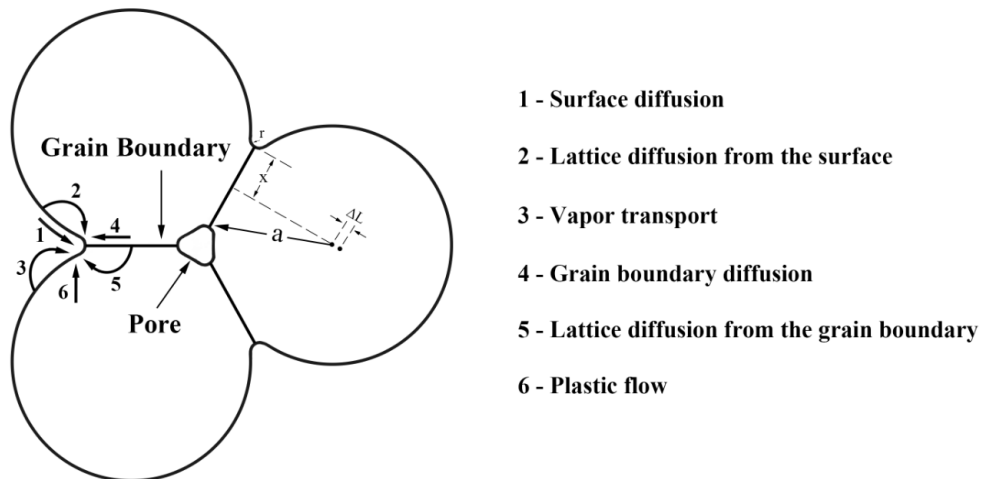


Figure 2. 2 Schematic illustration of different sintering mechanisms [29]

Those six different sintering mechanisms can also be classified as densifying and non-densifying mechanisms. Surface diffusion, lattice diffusion from the surface and vapour transport simply take atoms from the surface and re-arrange them onto another surface or part of the same surface. This matter re-arrangement will not cause pore to shrink and interparticle distance to reduce but the neck size will be increased. GB diffusion, lattice diffusion from the GB and plastic flow result in neck growth and densification and are referred to as densifying mechanisms. Atoms are moved from the bulk to the pore surface so that the pores can be eliminated and thereby increasing the density of sintered compact. GB diffusion and lattice

diffusion are important densification mechanisms in the sintering of metals and ceramics. Plastic flow, by dislocation motion in response to the sintering stress, is not critical to ceramic sintering due to the low dislocation density. The occurrence of plastic flow during the sintering of metals is controversial, but most likely dislocations participate in the initial stage of sintering [32]. The sintering neck formed between two equal-sized particles is assumed to be circular with a radius x . The equations for neck growth and shrinkage can be given by [28]:

$$\left(\frac{x}{a}\right)^m = \frac{H}{a^n} t \quad (2)$$

$$\left(\frac{\Delta L}{L_0}\right)^{m/2} = -\frac{H}{2^m a^n} t \quad (\text{only for the densifying mechanisms}) \quad (3)$$

where m and n are the integer exponent that depend on the sintering mechanism, H is a function that contains the geometrical and material parameters of the powder system. Plausible values for the numerical constants m , n , and H for each mechanism are given in the following **Table 2.1** [45]. For the non-densifying mechanisms, there is no shrinkage and $\Delta L/L_0 = 0$.

Table 2.1 Plausible values for the constants in equations

Sintering Mechanism	m	n	H
Surface diffusion	7	4	$\frac{56D_s\gamma\Omega\delta_s}{kT}$
Lattice diffusion from the surface	4	3	$\frac{20D_l\gamma\Omega}{kT}$
Vapor transport	3	2	$\frac{3\rho_v\gamma\Omega}{(2\pi mkT)^{1/2}kT}$
GB diffusion	6	4	$\frac{96D_{gb}\gamma\Omega\delta_{gb}}{kT}$
Lattice diffusion from the GB	5	3	$\frac{80\pi D_l\gamma\Omega}{kT}$
Plastic flow	2	1	$\frac{3\gamma}{2\eta}$

where D_{gb} , D_s and D_l are the diffusion coefficients for GB, surface and lattice diffusion, k is Boltzmann constant, Ω is volume of the diffusing vacancy, δ_{gb} and δ_s are the thickness for GB and surface diffusion, γ is surface tension energy, ρ_v is the vapor pressure over a flat surface, m is the mass of atom, η is the viscosity, T is the absolute temperature.

2.2 Cu nanoparticle based sintering

As the dimensions of a material decrease to the nanoscale, its melting temperature will decrease significantly due to the much larger surface to volume ratio than bulk material. The melting temperature of particles can be given by [33]:

$$T = T_0 \left(1 - \frac{2\sigma_{sl}v}{l_0 r} \right) \quad (4)$$

where T_0 is the bulk melting temperature, σ_{sl} is the surface area, v is the atomic volume, l_0 is the latent heat and r is the particle radius. From this equation, it is clear that the melting point of particle decreases with the decreasing particle size. When Cu nanoparticle size reaches to 26 nm, the melting temperature is only 225 °C, much lower than the value of bulk copper (1083 °C) [34]. Meanwhile, the sintering temperature is always below the melting point of a material to avoid melting. Therefore, based on changes to particle properties as dimensions shrink to the nanoscale, Cu nanoparticles can be sintered at a low temperature while the sintered structure possesses properties similar to those of bulk copper. For this reason, nanoparticle based sintering for high temperature joints is a topic of current interest.

2.2.1 Effect of joining conditions

Joining conditions such as sintering temperature or time, atmosphere and pressure are critical to the properties of Cu nanoparticle joint. Nishikawa et al. [21] compared the shear strength of joints made using Cu nanoparticle paste under vacuum and air sintering condition, and found that the formation of Cu oxide could inhibit the coalescence of Cu nanoparticles during sintering and lead to a much lower strength of joints bonded in air than joints bonded in vacuum.

The formation of Cu oxide seems to be inevitable as activated nanoparticle surfaces are readily oxidized by oxygen. Vacuum or inert gas atmosphere such as N₂ and Ar [20, 21, 23] is an effective way to prevent the oxidation of Cu and achieve high bonding strength joints.

High temperature or pressure and long duration can also greatly improve the strength of joint due to the enhanced driving force of sintering. Yamakawa et al. [20] reported the effect of joining temperature and applied pressure on the joint strength. Without the application of pressure, the joint strength was less than 10 MPa, even with a relatively high temperature of 400 °C. By contrast, the joint bonded at 400 °C with a 15 MPa pressure exceeded a high shear strength of 50 MPa. The dimple-like morphology which represents a ductile fracture and sufficient densification was only observed in the joints bonded at 350 °C and 400 °C. The fracture surface of sintered Cu nanoparticles in the joint below 300 °C shows a similar morphology to the original Cu nanoparticles and an insufficient densification of Cu sintering. Li et al. [23] and Yoon et al. [17] found a similar result regarding the effect of sintering temperature and pressure. Meanwhile, Yoon et al. [17] also proved that the joint strength increases with the increasing sintering times. Liu et al. [24] fabricated formic acid-treated Cu nanoparticles and found that the dimple-like morphology fracture appears at 260 °C which is much lower than the result from Yamakawa et al. [20]. This could be due to the removal of original Cu oxide by formic acid and the protection of sintering atmosphere of 5% H₂/95% N₂. They compared the shear strength of joints bonded from 160 to 320 °C with a constant pressure of 10 MPa and found an increasing trend of joint strength with increasing temperature.

However, these works are short of in-depth research linking the mechanism of sintering, the sintering conditions and the joint strength. The effect of sintering conditions on the porosity and grain size of sintered structure also requires more research. Zuruzi et al. [35] studied the densification of Ag nanoparticle during sintering and found both the porosity and electrical resistance decrease with increasing sintering times. Li et al. [36] measured the porosity and

thickness of the bonding layer between SiC die attachments made using Ag nanoparticles, and found that there are significant linear relationships between the joint strength and both the porosity and thickness. Chen et al. [37] introduced the Young's modulus and the growth ratio of particle necks besides porosity to characterise the properties of sintered Ag particle structure. The joint strength was found to be proportional to the necking growth while to be inversely proportional to the porosity. Cheng and Ngan [38] investigated the sintering behaviour of Cu nanoparticles at different sintering conditions by molecular dynamics simulation. Their result shows that higher temperature or pressure and smaller nanoparticle size can facilitate the densification and decrease the porosity.

The effect of sintering conditions on the grain size of sintered particle structure has been rarely studied as metallic particles coalesce together and the grain boundaries are not visible in the latter stage of sintering. By means of the back scattered electron (BSE) mode of SEM, the grains can be made visible due to the different contrast. Wang et al. [39] obtained the statistics of grain size distribution of sintered Ag nanoparticles at different temperatures and showed an obvious grain size growth with increasing temperature. However, they fail to correlate the grain size or porosity to the strength of sintered structure.

2.2.2 Copper oxide prevention and removal

2.2.2.1 Oxide removal and prevention

Cu nanoparticles readily oxidize due to the high surface activity. Special processing and storage conditions are necessary to prevent oxidation. Since native oxides on Cu nanoparticles would hinder the sintering process and decrease the joint strength. Acid pre-treatment followed by inert gas sintering is a popular way to remove the original oxide. Mou et al. [22] soaked Cu nanoparticles in a mixture of carboxylic acid and dehydrated ethanol to achieve the surface-modification. The surface-modified Cu nanoparticles were then sintered at 250 °C for 60 min with a pressure of 10 MPa under the protection of Ar-H₂ (5% H₂) gas mixture. Cu oxidation

was not found after sintering and the joints showed a high bonding strength over 30 MPa. Liu et al. [24] treated Cu nanoparticles with formic acid and found that the oxide is removed and copper formate forms on the surface of Cu nanoparticles. The copper formate will decompose into copper, carbon dioxide and hydrogen at the temperature range of 120-160 °C. The following sintering process under the atmosphere of 5% H₂/95% N₂ prevented the formation of Cu oxide and led to a highly conductive and strong Cu–Cu interconnection. Li et al. [40] and Liu et al. [41] also proved that Cu nanoparticles pretreated by formic acid are free of oxidation after sintering under inert atmosphere.

Besides carboxylic acid, some other reducing agents have also been used to remove the oxide of Cu nanoparticles. Yuan et al. [42] fabricated a complex reducing solution including copper formate, 2-amino-2-methyl-1-propanol and octylamine, and then mixed it with formic acid pretreated Cu nanoparticles. The carboxyl, carbonyl and amino groups in this reducing solution were proved to reduce Cu oxide into Cu during heating. Wang et al. [43] pre-treated Cu nanoparticles with lactic acid and then mixed them with the reducing agent of 3-dimethylamino-1,2-propanediol to form an anti-oxidative Cu paste. This reducing agent can prevent Cu nanoparticles from oxidation and also form complex with cupric compounds which would decompose into fresh Cu during sintering. Zhang et al. [44] mixed a surfactant of cetyltrimethyl ammonium bromide with colophony which contains abietic acid to fabricate the reducing agent. Gao et al. [45] employed ascorbic acid to reduce Cu oxide.

2.2.2.2 Reducing atmospheres

Reducing atmosphere is an alternative way to reduce Cu oxide into Cu. Formic acid is the most common reducing atmosphere [25, 46, 47]. Liu and Nishikawa [25] investigated a complex oxidation–reduction bonding process of Cu microparticles, which involves pre-heating samples at 130 °C for 5 min, heating at 300 °C for 20 min in air for microparticle oxidization, and holding at 300 °C for 40 min while introducing formic acid atmosphere into

the oven chamber. Cu nano-oxides formed on the surface of Cu microparticles were reduced by formic acid atmosphere into Cu nanoparticles which could significantly enhance the sinterability of Cu microparticles. Gao et al. [47] further shortened the bonding time of this approach from 65 min to 35 min by pre-oxidizing the Cu microparticle at 300 °C for 8 min. Ethyl alcohol [48], hydrogen [49, 50] and methanol [51] atmosphere have also been used as reducing atmosphere. However, these reducing gases have a relatively low reducing speed and require high reducing temperature (over 300 °C) compared to reducing agents, while most of them are toxic and flammable.

2.2.2.3 Laser sintering

Selective laser sintering possesses a faster processing speed with great oxidation suppression even in ambient environment, while traditional tube furnace heating suffers from an oxidation issue even with protective atmosphere [52]. Zenou et al [53] studied the conditions for laser sintering of Cu nanoparticle in ambient conditions while avoiding Cu oxidation. Kwon et al. [54] compared the selective laser air sintering with traditional tube furnace sintering in Ar atmosphere, they found that the sintered Cu nanoparticle thin film by laser shows better electrical property and less oxidation. Selective laser sintering has been well studied for flexible electronics applications, while it is not suitable for the sandwich structured chip packaging.

2.2.3 Reduction sintering of Copper oxide

Cu nanoparticles are a promising interconnection material due to low cost and superior conductivity although they readily oxidize and need special processing and storage conditions. To help address these issues, reduction sintering of Cu oxide particle has been proposed. Cu oxide nano/microparticles are much easier to synthesize than Cu nanoparticles and they are free from further oxidation. The reduction sintering process includes an additional reduction step of Cu oxide followed by sintering of the reduced Cu particle. The total bonding time of

Cu oxide particle is normally much greater than that of Cu nanoparticle, because sufficient reducing time is needed to completely transform Cu oxide into Cu.

Formic acid atmosphere was introduced by Liu and Nishikawa [25] to reduce Cu₂O nanoparticles formed on the Cu microparticle surface during preheating. The in situ formation of Cu nanoparticles during reduction could significantly increase the sinterability of Cu microparticles. Formic acid atmosphere has a relatively high reducing temperature of 300 °C and is also very harmful to human body [55]. The whole process of reduction sintering of Cu₂O nanoparticles requires up to 40 min and the total processing time (including preheating) of 65 min is non-ideal. The faster the reduction sintering, the less heat needs to be supplied. Another challenge of Cu oxide reduction sintering is to minimise the volume change of the material and the formation of gas reaction byproduct, which would increase the porosity in the sintering structure. Based on the above view, Cu₂O seems to be more preferable than CuO due to the lower oxygen content.

However, the reduction of CuO has been proven to be easier than the reduction of Cu₂O [56, 57]. The activation energy for the reduction of CuO by hydrogen is about 14.5 kcal/mol, while the value is 27.4 kcal/mol for Cu₂O. Cu₂O is more promising in terms of minimising the volume change of reaction while CuO is better for ease of reduction. Yasuda et al. [49] compared the bondability of CuO and Cu₂O as an interconnecting material and found that CuO has a much lower reducing temperature of 345°C by hydrogen and a higher bonding strength. The mechanism of CuO reduction by hydrogen is complex, involving an induction period and the embedding of H into the bulk of the oxide. CuO can be reduced directly to metallic Cu without formation of an intermediate or suboxide (Cu₄O₃ or Cu₂O) under a normal supply of hydrogen [58]. Meanwhile, CuO is free from further oxidation and there is no need for special storage conditions. Therefore, CuO is a promising candidate material for future interconnections.

Ogura et al. [59] replaced the complex reducing gas system by using the reducing solvent polyethylene glycol and found the reduction temperature 300 °C required for CuO nanoparticles is much higher than that for Ag₂O nanoparticles (150 °C) with the same reducing agent. The joint by Ag₂O/CuO mixed paste reached a high tensile strength of over 30 MPa at 300 °C for 5 min with an assisted pressure of 5 MPa. Yao et al. [60] only used CuO microparticles to fabricate the joint with the same conditions of Ogura et al. [59]. However, the joint strength was much lower, below 10 MPa without the addition of Ag. In conclusion, both the current reducing gas and reducing solvent processes require a relatively reducing temperature of over 300 °C. In the reducing gas system, organic solvent is not necessary and can be removed completely during preheating. The reducing speed of gas is much lower than solvent but the gas reaction byproduct will not produce bubble during reduction, which would cause porous sintering structure. The reducing solvent can reduce Cu oxide quickly while also producing many bubbles, and hence a considerable sintering pressure needs to be applied for good bonding strength.

Bhogaraju et al. [61] eliminated the use of Cu or CuO nanoparticles by directly decomposing copper formate into Cu nanoparticles; they achieved a high bonding strength interconnect at 275 °C with a 20 MPa pressure and N₂ atmosphere by this method. However, Copper formate, as a byproduct of the reaction of Cu oxide and formic acid, was also found to generate large bubbles during the decomposition process, which could create large voids during sintering. Huang et al. [62] proved that octylamine can greatly reduce bubble size and number due to its lower surface tension.

2.2.4 Particle size, shape and mixture

The particle joining process is driven by the reduction in particle surface area and is accompanied by the migration of atoms mainly along the particle surfaces. The driving force

at the interface of two contacted spherical particles during sintering can be given by the Laplace equation:

$$P = P_0 + \gamma \left(\frac{1}{R_1} + \frac{1}{R_2} \right) \quad (5)$$

where R_i is the curvature radius of particle, γ is the surface energy and P_0 is the external pressure of particle. Those results indicate that the sintering driving force would increase with decreasing particle size. Cu nanoparticles with diameter below 100 nm were mainly used in the sintered Cu interconnection [20, 22-24, 44, 63]. Zuo et al. [64] compared the shear strength of sintered Cu joints by different particle sizes of 20 nm, 100 nm and 1 μm and found the joint strength decreases with increasing particle size. It can be inferred that nanoscale particles possess high surface area resulting in high driving force for sintering and good sintered joint strength. However, the manufacture and storage cost would significantly increase when particle size decreases to nanoscale. Meanwhile, it has been reported that the packing density can be increased by using two different sizes of particles as smaller particles can fit into spaces left by the packing of mono-sized particles [65, 66]. Zuo et al. [67] found that smaller nanoparticles tend to surround the larger microparticles during sintering which leads to an increment of sintered density and joint strength. Therefore, the mixture of nanoparticles and microparticles could decrease the manufacture cost but increase the joint strength.

Besides spherical Cu nanoparticles, the microscale flake shaped Cu particles have also been studied for the sintered Cu interconnection [19, 68]. Liu and Nishikawa [19] preheated Cu flakes and spheres in air to form the Cu nano-oxides on the surface, then the oxides were reduced into Cu nanoparticles by formic acid atmosphere. The bonding of Cu flakes and spheres was achieved by sintering those reduced Cu nanoparticles with high surface activity. They found that the shear strength of joints with only Cu flakes by this oxidation–reduction bonding process is higher than the joints with Cu spheres, and the joint strength can be further strengthened by the mixture of Cu flakes and spheres (7.5:2.5, mass ratio) resulting in a higher

sintered density. Schwarzer et al. [68] also reported that the joint made from Cu flakes has a higher bonding strength than the joint by Cu spheres.

2.2.5 Particle Surface modification and composite

Cu microparticles have been proposed as a replacement of Cu nanoparticles by the virtue of lower cost and higher oxidation resistance. However, low surface activity of Cu microparticles makes them difficult to achieve acceptable sintering strength at low temperature. Zuo et al. [64] reported that the shear strength of joint with 1 μm Cu microparticles was only 4.5 MPa at sintering temperature of 250 °C and pressure of 2 MPa. Surface modification is one of effective approaches to increase surface activity of Cu microparticles and also prevent Cu oxidation, such as Sn coated [69, 70] or Ag coated Cu [71, 72]. Sn has a much lower melting point than Cu and thus enables Sn coated Cu microparticles to be sintered at a lower temperature. However, the brittle intermetallic compound (Cu_6Sn_5 and Cu_3Sn) and the voids formed between the interface of Cu/ Cu_3Sn and $\text{Cu}_3\text{Sn}/\text{Cu}_6\text{Sn}_5$ may reduce reliability of joint. Ag particles have a better sinterability than Cu particles and the introduction of Ag shell can improve the strength of sintered Cu microparticle, but the effect of Ag introduction on lowering sintering temperature is limited and considerable bonding strength requires up to 300 °C [71].

Surface treatment of Cu nanoparticles is another way to avoid Cu oxidation. Zuo et al. [73] coated a specific phosphating film on the surface of Cu nanoparticles and found that the Cu nanoparticles after treatment were free from oxidation at temperature below 300 °C. Some other researchers also mixed Cu nanoparticles with Ag nanoparticles [74-76] or Sn nanoparticles [77] to form the particle composite and achieve joint strength to be better than, or comparable with pure sintered Ag or Cu joints.

2.3 Alternatives to sintering nanoparticles

Although considerable sintered Cu joint strength has been achieved in many studies, special sintering conditions or processes and nanoparticle pre-treatment are necessary, which

compromise the Cu benefits of low cost, good conductivity and high electromigration resistance. Compared to Cu, Ag has a lower melting point and much better oxidation resistance. Ag nanoparticles can be sintered at a low temperature and achieve good sintering strength with low sintering pressure or even zero pressure. Although Ag₂O was also found to form in sintered Ag nanoparticles at 250 °C, it will subsequently decompose and produce Ag nanoparticles at the particle interface which results in the coarsening of sintered Ag particles. Meanwhile, it has been demonstrated that the formation of Ag oxide will not decrease the strength of sintered Ag structure [16]. Nanostructured Ag or multi Ag/Cu film was also applied as bonding material and this process eliminates the usage of harmful organic solvent to the electronics [78, 79]. However, Ag, as one of the more expensive metals, is less attractive for wide scale use.

Transient liquid phase (TLP) bonding is an alternative process for joining of power electronics. During this bonding process, the liquid phase is transiently formed at the bonding interface between the interlayer metal and base material. Interdiffusion results in the liquid phase being converted to intermetallics. The subsequent isothermal solidification leads to a bond with a higher melting point than the bonding temperature [7, 10]. TLP bonding materials can be widely classified into Sn and In based solders, such as Ni-Sn, Cu-Sn, Au-Sn, Au-In and Ag-In. Although some of these alloys have already been used in manufacturing, they suffer from different kinds of problems. For example, Au-Sn, Au-In and Ag-In have cost issue, Cu-Sn has a problem of oxidation and the formation of brittle IMCs (Cu₆Sn₅ and Cu₃Sn) could reduce the joint reliability, Ni-Sn has poor conductivity [13]. Meanwhile, the different diffusion rate of interdiffusing metals could lead to the formation of Kirkendall voids [14, 15], which is a common problem with solder joints. Cu₆Sn₅ nanoparticles have also been studied for die attachment of power electronics and the bonding mechanism is similar to the sintering of Cu/Ag nanoparticles [80, 81], but the formation of Cu₃Sn during high temperature service will cause Kirkendall Voids.

Direct Cu-Cu bonding (DCB) has the potential to replace the solder or nanoparticle paste joint in 3D packaging technology. Cu-Cu bonding is formed by the interdiffusion of atoms and grain growth between two flat wafer surfaces with Cu coating. However, the bonding process needs to be carried out under high temperature/pressure (over 350 °C) and vacuum condition to achieve good bonding strength [82, 83]. Surface activation can facilitate the surface diffusion by employing an Ar ion beam to clean the wafer surface prior to bonding [84, 85]. By means of ion beam cleaning, strong bonding can be achieved at room temperature though this process requires ultrahigh vacuum condition and is high in cost. Pd [86] or Ti [87] passivation layer on Cu film surface is another way to achieve Cu-Cu bonding at low temperature of under 200 °C but the whole process including pre-bonding (passivation) and annealing is very time-consuming. Nanotwinned Cu film with (111)-orientation seems to be more promising due to the high surface diffusivity on the (111) plane, which enables a low temperature direct bonding at 150 - 200 °C under an ordinary vacuum condition of 10^{-3} to 10^{-4} torr [88, 89].

2.4 Summary

Various materials have been used for the bonding materials, such as Ag, Cu and Sn-based alloys. Based on a comprehensive consideration of all aspects of material properties and bonding processes as shown in **Table 2. 2** and **2. 3**, sintering of Cu nanoparticles seems to be one of the optimal bonding techniques. High surface activity enables Cu nanoparticles to be sintered at a low temperature, while special processing conditions and nanoparticle pre-treatment are necessary to remove the original Cu oxide and suppress the formation of oxide during sintering. Cu microparticle is another promising bonding material and a shell layer such as Ag or Sn or in situ formed Cu nanoparticles are necessary to improve the low sinterability of Cu microparticles. Reduction followed sintering of CuO particles has also been proposed for joining as they are much easier to synthesize and store. However, the current reduction processes of CuO are non-ideal. For example, the reduction temperature of either gas

atmosphere or solvent is very high (over 300 °C). The use of reducing atmosphere during sintering can be dangerous due to the toxicity of some gases such as formic acid and could even cause an explosion. Therefore, Development of specific Cu or CuO nanoparticle bonding technique with ease of processing and investigation of the sintered Cu joint reliability during high temperature aging and in-depth research on the relevant sintering or oxidation mechanism occurring can enable the use of Cu or CuO nanoparticle in power electronics packaging.

Table 2. 2 Comparison of different interconnection material properties [90]

Material	Ag	Cu	Sn	Cu ₆ Sn ₅	Cu ₃ Sn	Ni ₃ Sn ₄
T _m (°C)	962	1083	221	415	676	796
ρ (μΩ•cm)	1.6	1.7	10.9	17.5	8.8	28.5
λ (Wcm ⁻¹ K ⁻¹)	429	401	66.8	47.7	70.4	19.6
CTE (10 ⁻⁶ /°C)	18.9	16.5	22.2	16.3	19.0	13.7
Cost (USD/kg)	603.1	6.5	20.5	12.5	10.0	18.3

Table 2. 3 Comparison of different interconnection processes

Joining Process	Cost	Conductivity	Difficulty of processing	Reliability
Sintering of Ag NPs	High	High	Low	Low EM
Sintering of Cu NPs	Medium	High	Medium	Oxidation
TLP of Cu-Sn	Low	Medium	Low	IMC/K-void
TLP of Ni-Sn	Low	Low	Low	IMC/ K-void
DCB of surface activation	High	High	High	Oxidation
DCB of (111) twin	Medium	High	Medium	Oxidation

Chapter 3: Methodology

3.1 Treatment of Cu substrate

A dummy Cu die with 4 mm diameter and 2 mm thickness was bonded using the paste on a dummy Cu substrate with 8 mm diameter and 3 mm thickness. Prior to bonding, the dummies were polished with emery paper (P1200-grit), soaked briefly in diluted hydrochloric acid, rinsed in ethanol and dried. The roughness of the polished Cu dummies is $R_a = 184.2 \pm 13.5$ nm (measured by AFM, Bruker Icon Dimension).

3.2 Fabrication of CuO paste and interconnect

CuO nanoparticles with mean diameter of 100 nm purchased from Sigma-Aldrich were used in this study. The initial morphology is as shown in **Fig. 3. 1**. Ascorbic acid and ethylene glycol were mixed as reducing agent I, glycerol and polyethylene glycol (PEG) were chosen as reducing agent II and III. CuO paste was composed by mixing CuO nanoparticle with reducing agent. The mass ratio of CuO to reducing agent was 2:8 except reducing agent I (15 wt% of CuO, 15 wt% of ascorbic acid and 70 wt% of ethylene glycol). The reduction temperatures of CuO nanoparticle for each reducing solvent were evaluated by Differential Scanning Calorimetry (STARe DSC822e) at a heating rate of 20 K/min in air.

The CuO paste was firstly printed on the surface of the dummy Cu die (the height of the paste drop is 2 mm) and then heated to the reducing temperature of the organic solvent for several minutes as shown schematically in **Fig. 3. 1**. Following reduction, the smaller Cu die with reduced Cu particles was forced face down on the top of dummy Cu substrate with placement pressure of 3 MPa for 1 minute to ensure good contact between the paste and the Cu discs. Next the assemblies were heated to 220 °C for 10 min, 15 min, 20 min, 40 min, 80 min and 240 min without pressure in air in order to determine the effects of sintering time. The whole heating process was conducted on a hot plate (Stuart SD160). This method is relevant to Chapter 4.

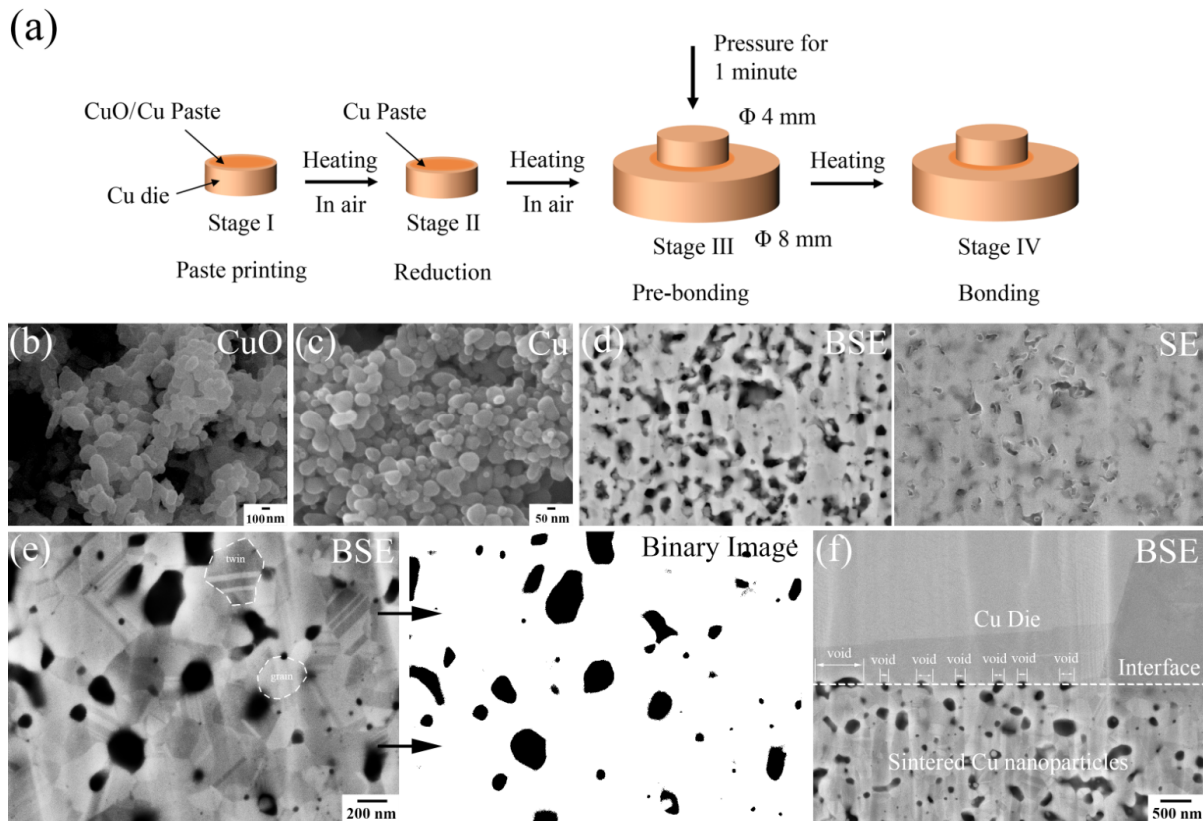


Figure 3. 1 Schematic illustration (a) of the bonding process. SEM images of CuO (b) and Cu (c) nanoparticles. Comparison of cross section image (d) of sintered Cu under SE and BSE mode. Representative BSE cross section image (e) of sintered Cu structure for grain size measurement and corresponding converted binary image for porosity measurement. BSE cross section image (f) of interface for porosity measurement

3.3 Fabrication of Cu paste and interconnect

Cu nanoparticles with mean diameter of 50 nm as shown in Fig. 1 (a) were purchased from Sigma-Aldrich. Reducing paste (gly) was composed by mixing Cu nanoparticle and the reducing agent/solvent, glycerol at a mass ratio of 3.5:6.5 (Cu/solvent). In contrast, a non-reducing paste (eth) was fabricated by mixing Cu nanoparticle with ethylene glycol (6.5:3.5, Cu/solvent). Ethylene glycol was mixed with CuO nanoparticles to evaluate its reduction effectiveness by Differential Scanning Calorimetry (STARe DSC822e) at a heating rate of 20 K/min in air.



The gly paste was firstly printed on the surface of the dummy Cu die (the height of the paste drop is 1 mm) and the following reduction and pre-bonding processes are same to the CuO joint in Section 4.2. Next the assemblies were held at 220 °C for 5 min under zero pressure on a hot plate (Stuart SD160) in air. Eth paste was printed into the overlap area between the Cu dummies, then the assemblies were heated in an oven (Lenton WF 60) with the same condition but under 3 MPa sintering pressure. This method is relevant to Chapter 5.

3.4 Fabrication of interconnect for different sintering conditions and aging test

After the reduction and pre-bonding processes (reducing paste), the assemblies were heated to different sintering conditions as shown in **Table 3. 1** under zero pressure and N₂ atmosphere in a tube furnace (Lenton LTF 12). (relevant to Chapter 6). The joints bonded at 220 °C for 20 min were chosen for the high temperature aging test. The joints were aged at 200 °C in air for 24 h, 100 h and 500 h in an oven (Lenton WF 60). (relevant to Chapter 7).

It should be noted that the different heating equipment has different heating speed to the desired temperature from room temperature (i.e. 1 min for hot plate, 3 min for oven and 7 min for tube furnace). The heating times mentioned in this chapter all represent the holding time at the set temperature.

Table 3. 1 Experimental design and distribution of factors

Set	Factor	Sintering conditions			
1	A (°C)	220 °C/5 min	250 °C/5 min	280 °C/5 min	310 °C/5 min
2	B (min)	220 °C/5 min	220 °C/10 min	220 °C/20 min	
3	B (min)	310 °C/5 min	310 °C/10 min	310 °C/20 min	

A - Sintering temperature, B - Sintering time.

3.5 Characterization analysis

The phase composition of Cu nanoparticles before and after reduction was measured by

XRD (Stoe StadiP, Mo radiation). The shear strengths of joints were assessed by means of a shear tester (Nordson Dage 4000) with the shearing speed of 50 $\mu\text{m/s}$ at room temperature. The mean values of ultimate shear strengths of five specimens for each bonding condition were calculated and reported for comparison. It should be noted that the joints in Chapter 5, 6 and 7 were fabricated by using the same Cu nanoparticles at different time periods (up to 2 years interval). The Cu nanoparticles were stored in a sealed bottle at ambient atmosphere and continually slow oxidation of Cu will cause a slight difference in the sintered Cu nanoparticle structure even with the same sintering condition. Therefore, the joint strength results in Chapter 5, 6 and 7 are slightly different even under the same sintering conditions.

The joints were cross sectioned and then polished by emery paper (2000-grit). After that, the cross sections were polished by ion beam miller (JEOL SM-09010) at 5 KV for 6-8 hours. The morphology of Cu nanoparticles, joint fracture surfaces and cross sections were observed by SEM equipped with energy dispersive X-ray Spectroscopy (EDS) (Hitachi S4000, Tescan-Delmic SEM-CL and Zeiss Zeiss EVO LS15, 10 KV for back scattered electron (BSE) mode and 30 KV for secondary electron (SE) mode). The curves of DSC, XRD and sintered Cu characteristics (i.e. porosity, grain or pore size and strength) with sintering temperature or time were plot by Origin and the length of error bars refers to the doubled standard deviation.

3.6 Grain size and pore size/number/shape and porosity measurement

By means of BSE mode of SEM, the grains can be made visible due to their different contrast values [78]. Most grain cross sections are approximately elliptic while some show irregular shapes as shown in **Fig. 3. 1 (e)**. A parameter for grain size, d , was extracted from the data by calculating equivalent sphere diameter as follows:

$$d = 2 \sqrt{\frac{S}{\pi}} \quad (6)$$

where S is the grain area. Up to 500 grains from SEM cross section images of three polished

samples for each condition were measured for the mean value and distribution of grain size. The measurement was conducted by Photoshop and ImageJ.

The voids in the sintered Cu nanoparticle structure are more visible in BSE mode of SEM compared to the SE mode as shown in **Fig. 3. 1 (d)**, and hence the BSE images were used for porosity measurement. Twenty SEM cross section images of the sintered layer of three polished samples for each bonding condition with an area of 8 μm x 8 μm were selected to measure the porosity. The SEM images were converted into binary image before measurement and the porosity of sintered layer was calculated according to the following formula:

$$\rho = \frac{p_v}{p_t} \quad (7)$$

where p_v is the sum of black pixels and p_t is the sum of all the pixels. The measurement was conducted by MATLAB[®]. The porosity at the bonding interface between sintered Cu nanoparticles and Cu die/substrate was also calculated. The porosity at the interface was calculated by taking the ratio of the diameter of voids at the interface to the interface length as shown in **Fig. 3. 1 (f)**. Twenty SEM cross section images of the interface (including both Cu die and substrate) of three polished samples for each bonding condition with an area of 20 μm x 20 μm were selected to measure the porosity at interface. The measurement was conducted by ImageJ.

The pore size was measured using the same method as the grain size (equation (1)). Meanwhile, the distribution of pore eccentricity was also measured to show the change of pore shape. The closer to 0 the eccentricity value, the closer the pore to spherical shape. Up to 1000 pores from SEM cross section images of three polished samples for each condition with an area of 8 μm x 8 μm were measured for the mean value and distribution of pore size and shape. The measurement was conducted by MATLAB[®]. The mean pore number (PN) in the unit area of 1 μm^2 was also calculated. The sum of pore number in SEM image was measured by MATLAB[®]

and the image area was measured by ImageJ based on the scale bar. This section is relevant to Chapters 6 and 7.

3.7 Observation of microstructure during heating and aging

A quasi-in-situ method was adopted in this study by intermittently observing the grain growth in the microstructure of one joint cross section during the heating process of **Table 3.1** [91]. The same joint was slightly etched by ion beam milling at 4 KV for only 2 minutes (see more detail regarding the etching time in Appendix) for microstructure observation after every heating step so that the GB could be clearly seen. After etching, the sample was immediately moved and inserted into the SEM chamber within 5 minutes. It should be noted that this term “quasi-in-situ” has been widely used in the interrupted (S)TEM or SEM observation [91-93], where the sample needs to be treated (i.e. heat, corrosion and catalysis) out of the chamber and the same place of sample will be observed after the treatment. (relevant to Chapter 5 and 6).

The joint cross section structure was sequentially aged at 200 °C in air for 1 h, 3 h, 10 h and 24 h to accelerate the oxidation of sintered Cu structure and study the effect of oxidation. The same joint was slightly etched by ion beam miller at 5 KV to adequately remove the oxide formed on the Cu surface after every aging step so that the original sintered Cu structure could be clearly seen. A light microscope (Zeiss Axio) was used to determine if the oxide is removed adequately as the oxide show a different color to Cu under the light microscope. The mean oxygen content of the sintered Cu structure was calculated from the EDS mapping of twenty SEM cross section and fracture surface images of three samples for each bonding condition. The mean oxidation area of the joints was measured from the fracture surface images of five samples. The oxidized structure shows a different color of black and grey to the original structure (orange). The oxidation area was calculated by dividing the sum of black and grey area pixels to the sum of all the pixels. The measurement was conducted by Photoshop (relevant to Chapter 7).

Chapter 4: In situ reduction-sintering of CuO nanoparticle

4.1 Background

High temperature or pressure assisted sintering with protective atmosphere is necessary to achieve acceptable sintering strength of Cu nanoparticles due to ease of oxidation, and this could increase the process complexity and damage some temperature sensitive devices [20]. Kwon et al. [54] suppressed the oxidation of Cu nanoparticle during sintering by selective laser sintering, which possesses a faster sintering speed than a conventional furnace, while oxidation from environmental exposure during use is still inevitable and nanoparticle storage requires special conditions to prevent oxidation. Zuo et al. [73] coated a specific phosphating film on the surface of Cu nanoparticles and found that the Cu nanoparticles after treatment were free from oxidation at temperatures below 300 °C, However the consumption of the Cu nanoparticle during treatment was high and the dense phosphating film may hinder the coalescence between Cu nanoparticles.

To help address these issues, reduction sintering of CuO particle has been proposed. Cu oxide nano/microparticles are much easier to synthesize than Cu nanoparticles and they are free from further oxidation. The reduction sintering process includes an additional reduction step of CuO particles followed by sintering of the reduced Cu particle. The total bonding time of CuO particle paste is normally much greater than that of Cu particle paste, because sufficient reducing time is needed to completely transform CuO into Cu. Liu and Nishikawa [25] investigated a complex oxidation–reduction bonding process of Cu microparticles, which involves pre-heating samples at 130 °C for 5 min, heating at 300 °C for 20 min in air for microparticle oxidization, and holding at 300 °C for 40 min while introducing reducing formic acid atmosphere into the oven chamber. Gao et al. [47] further shortened the bonding time of this approach from 65 min to 35 min by pre-oxidizing the Cu microparticle at 300 °C for 8 min, but the total processing time is still non-ideal. Ogura et al. [59] replaced the complex reducing

gas system by using the reducing solvent polyethylene glycol and found the reduction temperature 300 °C required for CuO nanoparticles is much higher than that for Ag₂O nanoparticles (150 °C) with the same reducing agent. In order to bring the bonding temperature of CuO particles down to an acceptable value for manufacturing (below 300°C), the reduction temperature should be as low as possible. A reducing organic solvent appears to be more promising than reducing gas due to its ease of manufacturing, but most typically used solvents will completely decompose or evaporate before reaching the reduction temperature. Therefore, the choice of reducing solvent for CuO reduction bonding is limited and the oxidation mechanism of the Cu particles during sintering and its impact on sintering strength requires more research.

4.2 Objectives

This chapter aims to develop a specific Cu nano/microparticle bonding technique with ease of processing (i.e. eliminating the use of sintering pressure or protective atmosphere). Here, an in situ reduction-sintering of CuO nanoparticles was proposed to fabricate strong Cu-Cu bonding without special processing conditions. The growth behavior and morphological evolution of oxide during sintering were detailed and the effect of oxide on the sintering strength of Cu particles was investigated. The micro-fracture mechanism of sintered Cu particles was also studied.

4.3 Methods

Glycerol, PEG and the mixture of ascorbic acid and ethylene glycol, were chosen as reducing agent. CuO nanoparticles were mixed with the reducing agent to fabricate the paste. The reduction temperature and reduced particle size were analyzed by DSC and SEM, respectively. The paste was printed on the dummy Cu die surface and then heated to the reducing temperature for several minutes. Following reduction, the Cu die with reduced Cu particles was forced face down on the top of dummy Cu substrate with placement pressure of 3 MPa for 1 minute to

ensure good contact between the paste and the Cu discs. Next the assemblies were heated to 220 °C for 10 min, 15 min, 20 min, 40 min, 80 min and 240 min without pressure in air in order to determine the effects of sintering time.

4.4 Results and Discussion

4.4.1 Comparison of different reducing agents

Ascorbic acid, glycerol and PEG were chosen as the reducing agents. It should be noted that ascorbic acid is powder and since an organic solvent is necessary to disperse the CuO nanoparticles and fabricate the paste, ethylene glycol was mixed with the ascorbic acid to make the reducing solutions. The paste mixed by ethylene glycol and CuO nanoparticles was tested by DSC as shown in **Fig. 4. 1 (a)**. The result shows that there is no exothermic peak in the red curve, indicating that CuO nanoparticles cannot be reduced by ethylene glycol liquid alone. Next, ascorbic acid was mixed with ethylene glycol and CuO nanoparticles. It can be concluded that the exothermic peak at 135 °C in the black curve shown in **Fig. 4. 1 (a)** was caused by the reduction reaction between ascorbic acid and CuO nanoparticles [45]. The mean diameter of reduced Cu particle by ascorbic acid at 135 °C was 500 nm and the shape was spherical as shown in **Fig. 4. 2 (a)**. However, the EDS results show the existence of carbon indicating the presence of organic residues after reduction, which would significantly hinder the coalescence between Cu particles during sintering. The organic residues may decompose at higher temperature while high sintering pressure is necessary to compress the particles for achieving dense sintering structure.

By comparing the difference between the curves of reducing agent II, glycerol and reducing agent III, PEG with and without CuO nanoparticles, the reducing temperature of the organic solvent is found by the position of the additional exothermic peak in the black curve. PEG had the highest reducing temperature of 320 °C and produced in the smallest reduced particle size of 300 nm. There was still some organic compound covering the reduced particles as shown in

Fig. 4. 2 (b) and the corresponding EDS results also show the existence of carbon. Meanwhile, an unacceptably high sintering temperature of over 320 °C is necessary to decompose these organic compounds. The reduction temperature of glycerol was 220 °C and reduction reactions began at just 200 °C. The reduced Cu particles have a larger mean size of 1 μm and a cleaner surface as shown in **Fig. 4. 2 (c)**. Carbon was not detected on the reduced Cu particles which indicates that most of the organic compounds decomposed. The existence of oxygen (6.54 %) also indicates that the reduced Cu particles were slightly oxidized by air after reduction.

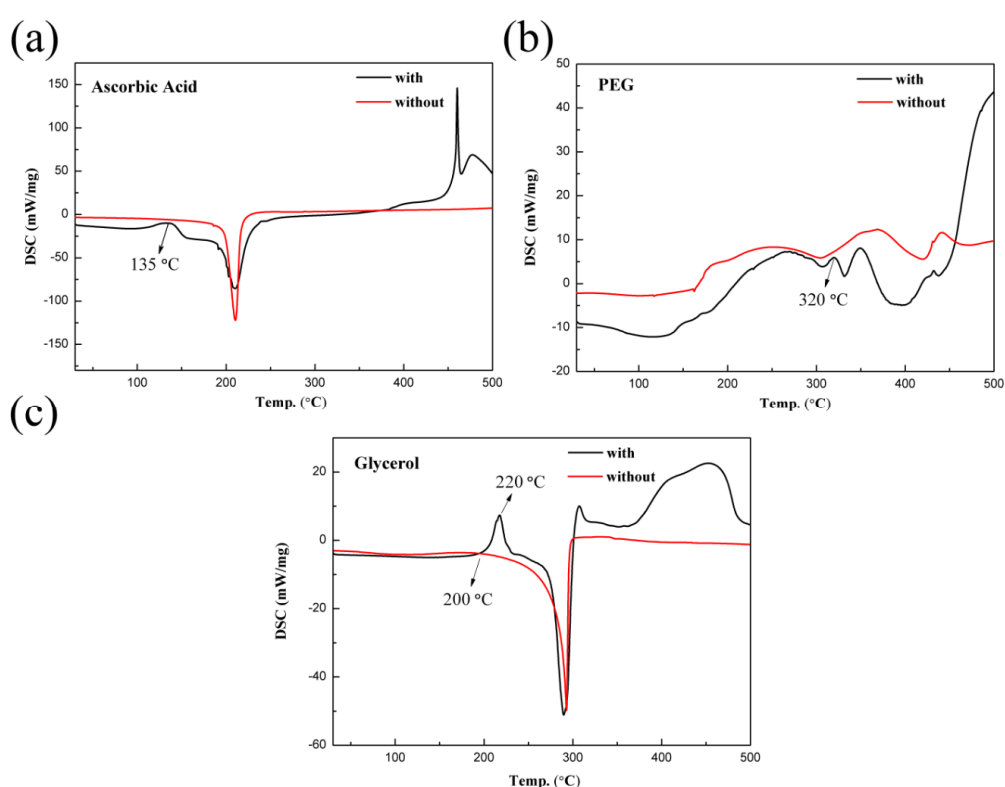


Figure 4. 1 Thermal analysis of (a) ethylene glycol and CuO nanoparticle with and without ascorbic acid, PEG (b) and glycerol (c) respectively with and without CuO

Metal nanoparticles have been reported to grow through merging primary particles and organic ligands serve as stabilizers to prevent nanoparticle merging [94]. Love et al. [95] also reported that the organic shell can act as a physical or electrostatic barrier against aggregation of nanoparticle. These results suggest that organic residues on particle surfaces can depress Cu particles growth by preventing them merging and result in a smaller particle size. Therefore, it

can be concluded that glycerol is the optimal reducing agent for CuO nanoparticle with the mean size of reduced particle being 1 μm . The main reduction reaction of CuO by glycerol is given in eq. (7) while the oxidation products will vary with the degree of oxidation [96]:

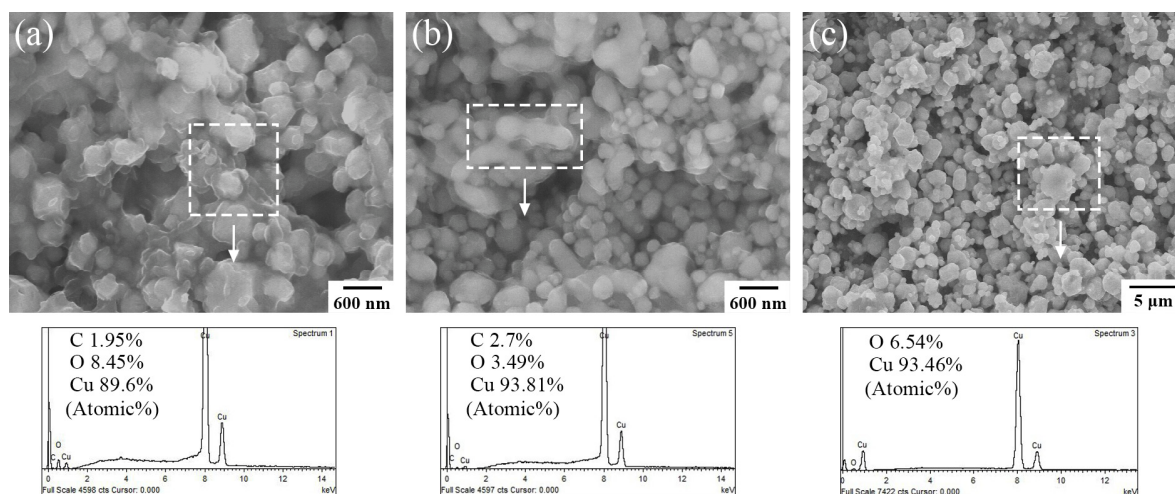
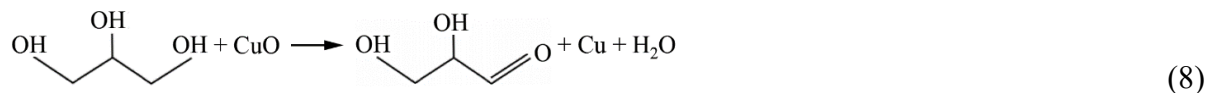


Figure 4.2 Morphology and EDS results of reduced Cu particle by ascorbic acid at 135 °C (a), PEG at 320 °C (b) and glycerol at 220 °C (c)

Fig. 4.3 shows the morphology and size distribution of the reduced Cu particles by glycerol at 200 °C, 210 °C, 220 °C and 230 °C. The minimum required durations of the reduction step with different temperature were also measured (the counting begins after putting the small disc with printed paste on hot plate and ends when no reaction bubble forms). With increasing reduction temperature, the shape of the reduced particles remained spherical while the reduction time was greatly shortened from 6 min and 20 sec at 200 °C to 2 min and 12 sec at 230 °C. The reduced Cu particles at different temperatures shear similar mean diameter and size distribution. However, the water reaction byproduct will boil and create bubbles in the paste during reduction. Higher reduction temperature will cause more violent reaction and severe paste splash which is negative to manufacturing. Meanwhile the Cu particle oxidizes easily at higher temperature negating the benefit of reduced reduction time. Higher temperature

may also damage some sensitive electronics components and raise cost. Therefore, the 220 °C temperature has been determined as the most suitable reduction temperature of CuO nanoparticles by glycerol.

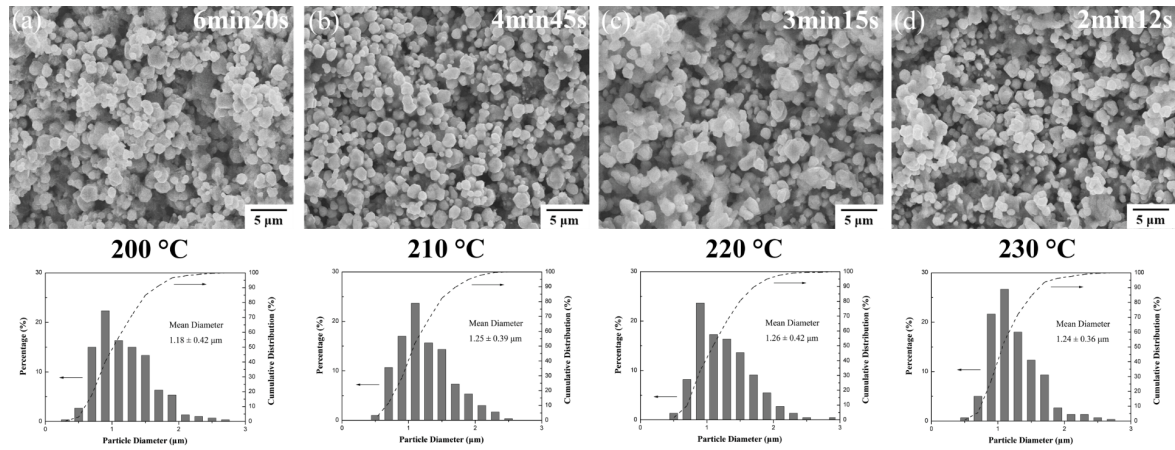


Figure 4. 3 Morphology and size distribution of reduced Cu particle by glycerol at 200 °C (a), 210 °C (b), 220 °C (c) and 230 °C (d). Required reduction times are shown in figure

4.4.2 Effect of sintering time on the microstructure

In order to confirm the most suitable mass ratio between CuO nanoparticles and glycerol, the phase composition of fracture surfaces of joints with differing concentrations of CuO in the paste was analyzed by X-ray diffraction (Mo radiation) as shown in **Fig. 4. 4 (a)**. With low CuO content, only Cu peaks can be detected. However, when the mass ratio rises to 40%, obvious Cu₂O peaks began to appear. Since a higher concentration of CuO nanoparticles leads to more reduced Cu particles in the paste and a denser sintering structure, the mass ratio of 3.5:6.5 is most suitable. **Fig. 4. 4 (b)** shows the XRD patterns (Mo radiation) of fracture surfaces of (3.5:6.5) joints with different bonding times. When the bonding times were 10 min and 15 min, XRD patterns show obvious peaks of metallic Cu and the intensity of the Cu₂O peak was negligible. The corresponding EDS results of the 15 min joint (see Fig. A1 in Appendix) show an increasing oxygen content of 11.59 % compared to the oxygen content

(6.54 %) of the original reduced Cu particles, which indicates that more oxygen atoms were adsorbed on the surface of Cu particles with increasing bonding time. As time rose to 20 min, a Cu₂O peak corresponding to the crystal plane of (111) began to appear, and the color of Cu sintered particles also changed from their natural orange into dark red due to the formation of Cu₂O as shown in **Fig. 4. 4 (c)**. As time further rose to 40 min, another two Cu₂O peaks related to crystal planes of (200) and (220) were detected, while the strength of peaks was weak. The oxygen content also increased to 25.99 % (see Fig. A2 Appendix) and the color of Cu sintered particles further changed to dark grey. The strength of these three Cu₂O peaks became stronger with further increasing time. However, even with 240 min bonding time, no obvious CuO peak was found. These results indicate that Cu₂O is the only oxidation product of Cu particles within 240 min of sintering at 220 °C. Yang et al. [97] reported similar results that only the Cu₂O formed on the surface of Cu powder at 200 °C and formation of CuO occurred at 300 °C.

From the point of view of manufacturing, Cu-Cu bonding should be performed at a reasonably low temperature and pressure with a time that is as short as possible. The joints for shear test were fabricated with bonding times between 10 min and 80 min. The shear strengths of joints using 3.5:6.5 paste are plotted in **Fig. 4. 4 (d)** as a function of bonding time (error bars calculated by mean value \pm one standard deviation of shear strengths). From this plot it is apparent that the shear strength of the joint increased firstly with increasing time and reached a peak of 22 MPa at 15 min. Then it decreased as bonding time rose to 20 min where obvious Cu₂O structure began to appear according to the XRD results. These results indicate that there is no significantly negative effect of surface oxygen chemisorption on the sintering strength of Cu particles and the formation of Cu oxide structure is responsible for the degradation of joint shear strength. Zuo et al. [64] employed Cu microparticles with a size of 1 μ m and non-reducing organic solvent to fabricate Cu-Cu joints, with the higher temperature of 250 °C and sintering pressure of 2 MPa. Under these conditions the reported joint strength is nearly five times lower

than the best shear strengths of the current (3.5:6.5) joints as shown in **Fig. 4. 4 (d)**.

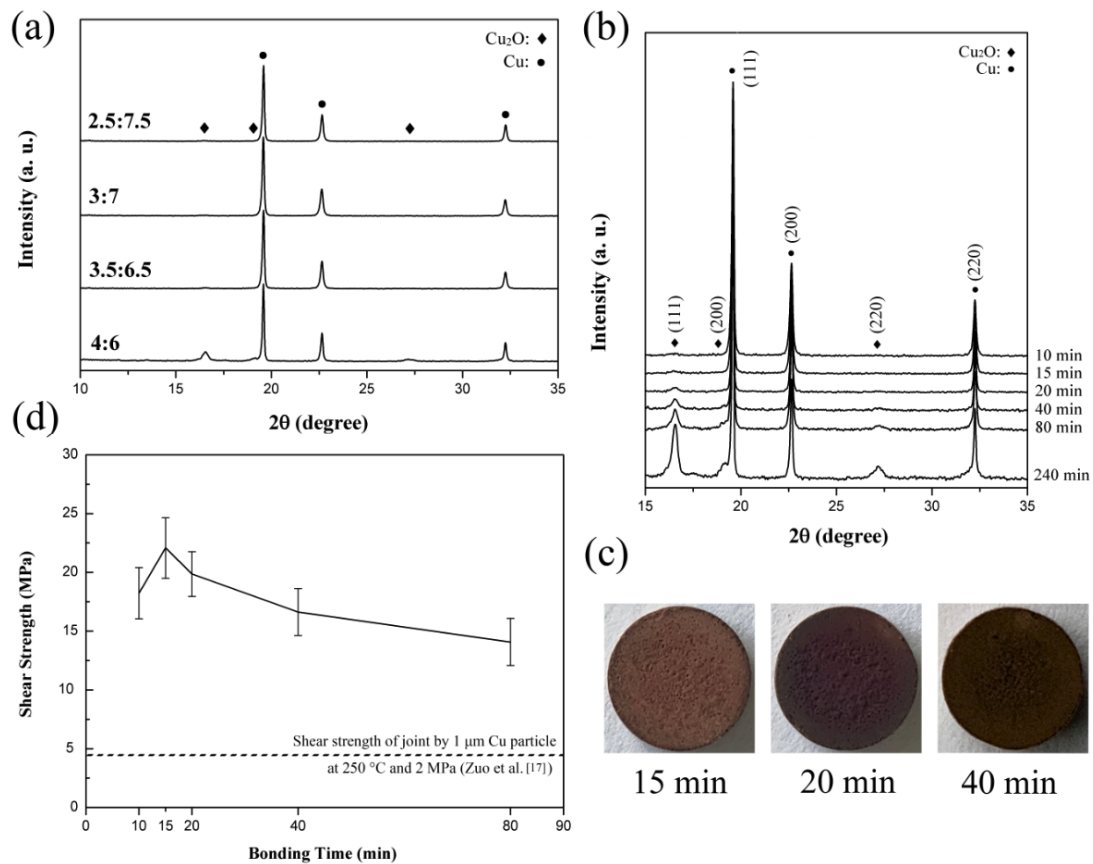


Figure 4. 4 XRD patterns (a) of fracture surfaces of joints with different mass ratios of CuO nanoparticle to glycerol, XRD patterns (b) and images (c) of fracture surfaces and shear strengths (d) of (3.5:6.5) joints for different bonding time. (Shear tests were performed in five replicates)

Compared with traditional Cu nanoparticle sintering, the specific reduction-sintering omits the heating step from room temperature where Cu oxidation usually appears. Meanwhile, the reduced Cu submicron particles have higher oxidation resistance than Cu nanoparticles can be quickly and directly sintered at the reduction temperature. These properties lead to the high shear strength of joint formed by this method. During the reduction and pre-bonding process, the oxide is reduced to Cu particle which would immediately coalesce with other Cu particles at the high processing temperature of 220 °C. The sintered reduced Cu would be oxidized at the ambient condition and the remaining organics are able to reduce the oxidized Cu again.

Therefore, the reduction and sintering of Cu occur simultaneously and this process is termed in situ reduction-sintering process.

Fig. 4. 5 shows SEM images of fracture surface of the (3.5:6.5) joint for different bonding times. The morphology of the fracture surface shows little change with increasing time while the surface of the Cu particle changed from smooth to rough due to the formed oxidation film. Meanwhile, Cu particles have deformed little and significant coalescence between particles was not found. It is also clear that the fracture is mainly located at the interface between Cu particles.

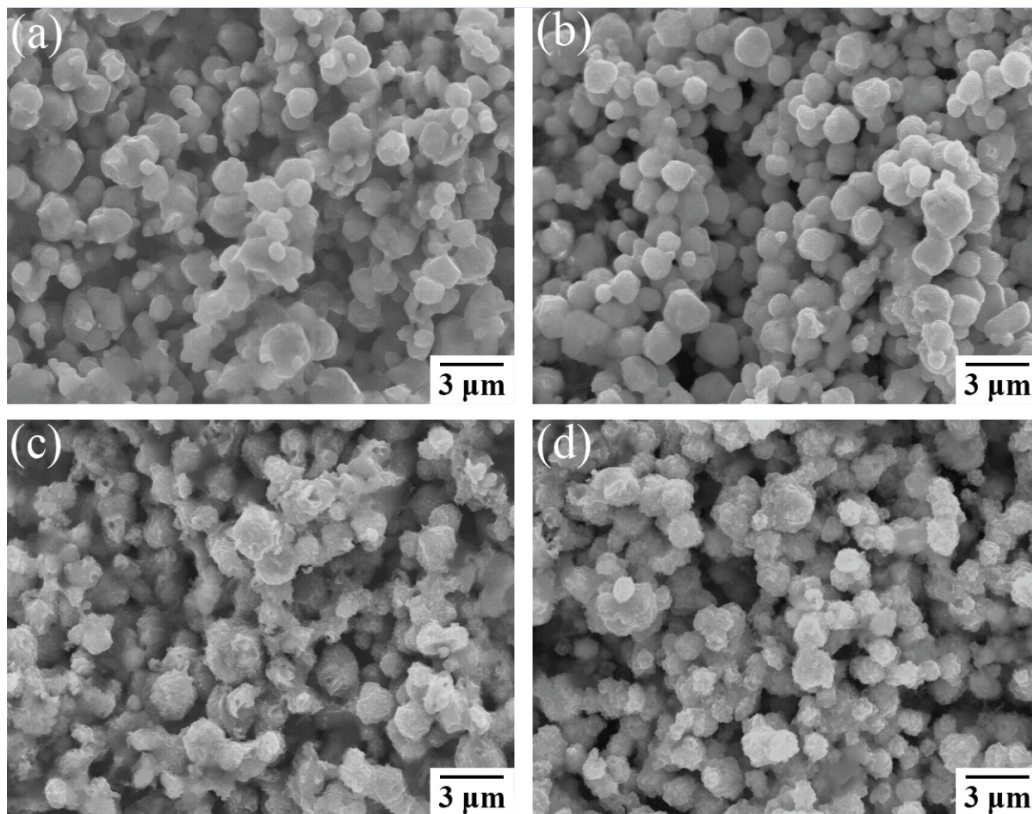


Figure 4. 5 SEM fracture surface images of joints for 15 min (a), 20 min (b), 40 min (c) and 80 min (d)

To investigate the effect of oxidation on the sintered structure, the 15 min joints with best strength and no obvious oxide were compared with the 40 min joints with clear oxide structure. SEM cross section images of representative joints after cutting and polishing are shown in **Fig. 4. 5**. Both cross sections of 15 min and 40 min show a dense and porous structure and

significant sintering coalescence between particles was found as shown in **Fig. 4. 6 (b) and (d)**. The interfaces between Cu particles and disc also show good bonding as shown in **Fig. 4. 6 (c) and (f)** and the Cu particles have deformed due to interdiffusion with the substrate. However, by comparing the images of cross section of 15 min and 40 min, it is clear that an oxidation film has formed on surface of particles at 40 min as shown in **Fig. 4. 6 (d) and (e)**, depressing further diffusion of Cu atoms and causing poor sintering strength, which is in good agreement with shear test results.

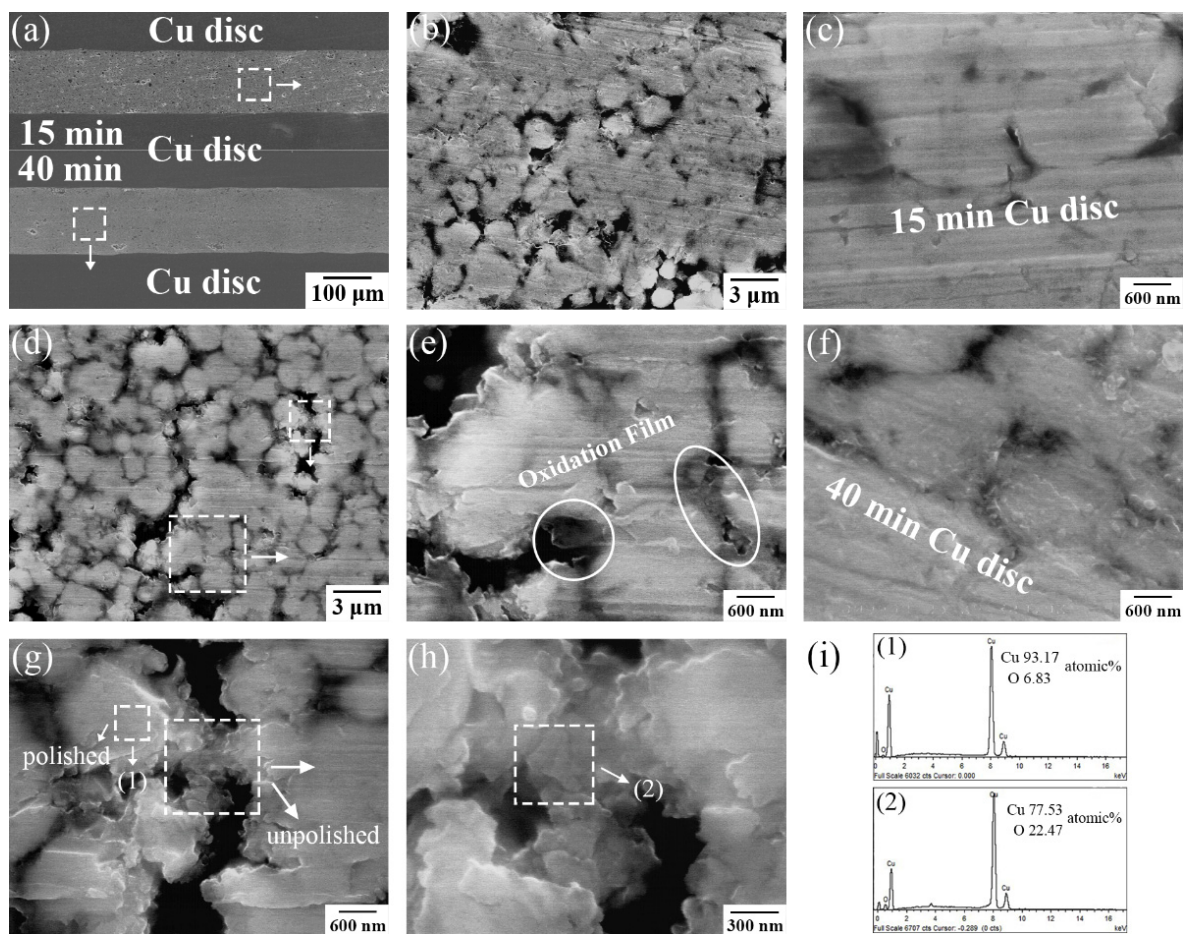


Figure 4. 6 SEM cross section images of joints bonded for 15 min (a, b, c) and 40 min (d, e, f, g, h), as well as corresponding EDS results (i)

In order to prove the existence of the oxidation film, the sintered Cu particles with uneven surface in the 40 min joints cross section was polished and the oxide in only outer Cu particle was removed while the oxide in inner Cu particle remained as shown in **Fig. 4. 6 (g)**. The

relevant EDS results show that the oxygen content of the polished particle is much lower than that of unpolished one. Meanwhile, the oxygen content of cross sections of 15 min joint and 40 min joint (8.01% and 19.17%, respectively, see Fig. A3-4 Appendix) were both lower than the values (11.59% and 25.99%, respectively) of the corresponding fracture surfaces, which indicates that fracture tends to appear in sintering areas with high oxidation.

4.4.3 Growth behavior of cuprous oxide

The primary oxide formed on the surface of Cu micro/nano particle during low temperature sintering has been reported to be cuprous oxide (Cu_2O) and its formation plays a critical role in determining the shear strength of Cu-Cu joint [25, 73]. However, growth behavior and morphological evolution of Cu_2O during sintering still remain unclear and require further study. Cu_2O with cubic crystalline structure has been reported to grow epitaxially on the Cu surface. The sequence of oxidation reactions on a clean metal surface is generally accepted to be oxygen chemisorption, nucleation and growth of surface oxide, and bulk oxide growth. Before the onset of oxidation, a restructured Cu surface due to oxygen saturation has been proven to be important for formation of Cu_2O . Lee et al. [98] reported that the subsurface oxide-like structure was more easily produced on a Cu surface with pre-adsorbed oxygen atoms. The mechanism of nucleation and initial growth of oxide islands on a clean Cu surface has been proposed in terms of ‘capture zone’ theory [99], which claims that oxygen atoms diffuse on Cu surface and become incorporated into an oxide island when entering the surrounding capture zone. After oxide islands reach the saturation point of nucleation, they start to grow and coalesce to generate a thin layer of Cu_2O . Oxygen diffusion dominates initial growth of the oxide, and direct impingement of oxygen atoms onto islands is also likely to occur when island size becomes larger [100]. The formed Cu_2O layer prevents exposure of Cu to oxygen. Further oxidation of Cu occurs on both internal and external surfaces of the oxide layer and is a result of Cu atoms from the underlying Cu metal core diffusing outward through the oxide layer and

oxygen atoms diffusing into the Cu core. Meanwhile, Hung et al. [101] reported that oxygen atoms are absorbed into oxide layer surface and electrons penetrate into the layer by tunneling to establish equilibrium between Cu ions and oxygen ions, this process produces an electric field which provides an additional driving force for Cu ions move outward.

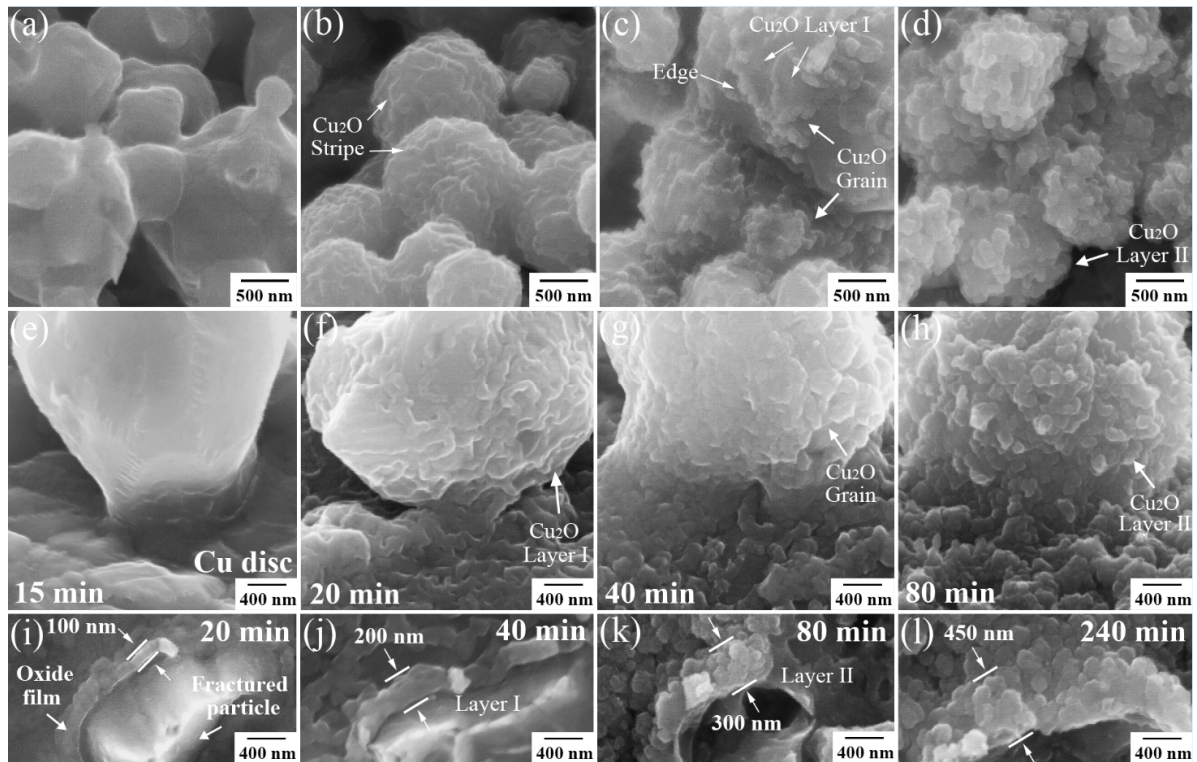


Figure 4. 7 SEM images of interfaces between Cu particles and between Cu particle and disc for 15 min (a, e), 20 min (b, f), 40 min (c, g) and 80 min (d, h). Comparison of oxide thickness between 20 min (i), 40 min (j), 80 min (k) and 240 min (l)

The surfaces of Cu particles for 15 min were very clean and show no obvious oxide structure as shown in **Fig. 4. 7 (a)** and **(e)**, which matches the corresponding XRD results very well (presented in Section 5.3.2). The existence of oxygen detected by EDS can be attributed to oxygen chemisorption and nucleation of oxide islands, which are inevitable for air sintering at 220 °C. When bonding time is 20 min, oxide islands reached the saturation point of nucleation and started to grow and show an irregularly striped structure as shown in **Fig. 4. 7 (b)**. They later coalesced together and produced a thin Cu₂O laminar layer termed Cu₂O layer I as shown

in **Fig. 4. 7 (c) and (j)**. Additionally new oxide islands formed and grew on the surface of some existing Cu_2O layers I to produce a multilayer structure. As time further rose to 40 min, oxide islands with a second morphology of Cu_2O grain began to appear and showed a spherical structure with a mean diameter of 100 nm. Their nucleation was more likely to occur at the edge area of Cu_2O layer I as shown in **Fig. 4. 7 (c)**, which acted as defect site rather than the surface. It has also been reported that defect locations such as grain boundaries [102] and edge of a pit [103] are preferential nucleating sites for oxide island formation. Cu_2O grains later grew and coalesced together, which led to thickening of the oxide layer, replacement of Cu_2O layer I by many crossed and overlapping Cu_2O grains and formation of a new multiple Cu_2O layer termed Cu_2O layer II as shown in **Fig. 4. 7 (d), (h), (k) and (l)**. The interface structure between Cu particle and disc shows a similar oxidation trend with time as shown in **Fig. 4. 7 (e-h)** and the Cu disc surface was also oxidized after sintering. The thickness of oxide film increased from 100 nm at 20 min (bonding time) to 450 nm at 240 min as shown in **Fig. 4. 7 (i-l)**, which indicates that more Cu will be oxidized into Cu_2O with increasing time.

4.4.4 Variation in shear strength and fracture mechanism of joint

The bonding strength of Cu-Cu joints produced by sintering Cu is strongly related to contact area between sintering layer and substrate, and also the density of the sintered structure which is directly proportional to contact area between particles [67]. Made et al. [104] also proved that contact area was directly proportional to shear strength of the Cu-Cu thermal compression bond based on simulated and experimental results. After the pressure-assisted placement step, the joint was held at 220 °C with no pressure. Further increase of contact areas and joint strength results from relatively slow thermal diffusion.

However, the shear strength of joints stops increasing with bonding time and eventually decreases when the oxide forms as discussed Section 5.3.2. In order to investigate the reason, the micro-fracture mode of sintered Cu particles bonded for 80 min was observed by SEM as

shown in **Fig. 4. 8**. The submillimeter scale fracture surface of the joint (presented in Section 5.3.2) indicates that the Cu particles have deformed little after shearing and the fracture is mainly located at the interface between sintered Cu particles. However, the submicron scale fracture shows the evidence of plastic deformation of some Cu particles and fracture occurred inside Cu particles. These results indicate that there are three different fracture modes of the joint: 1) Brittle fracture at the interface between Cu particle and disc as shown in **Fig. 4. 8 (a)**. 2) Brittle fracture at the interface between Cu particles as shown in **Fig. 4. 8 (c)**. 3) Ductile fracture inside Cu particles with different deformation degrees as shown in **Fig. 4. 8 (b) and (d)**. However, the Cu₂O film shows little plastic deformation in either case which indicates it is a brittle structure with poor strength, and there was poor bonding between Cu core and Cu₂O film. Yuan et al. [105] has also reported that there was an obvious crack between the Cu₂O layer and Cu disc surface. It can be inferred that Cu₂O film was not able to provide effective strength for the whole bonding structure. In summary, formation of brittle Cu₂O structure with bad bonding to Cu core and disc and decrease of Cu-Cu contact area result in decreasing shear strength.

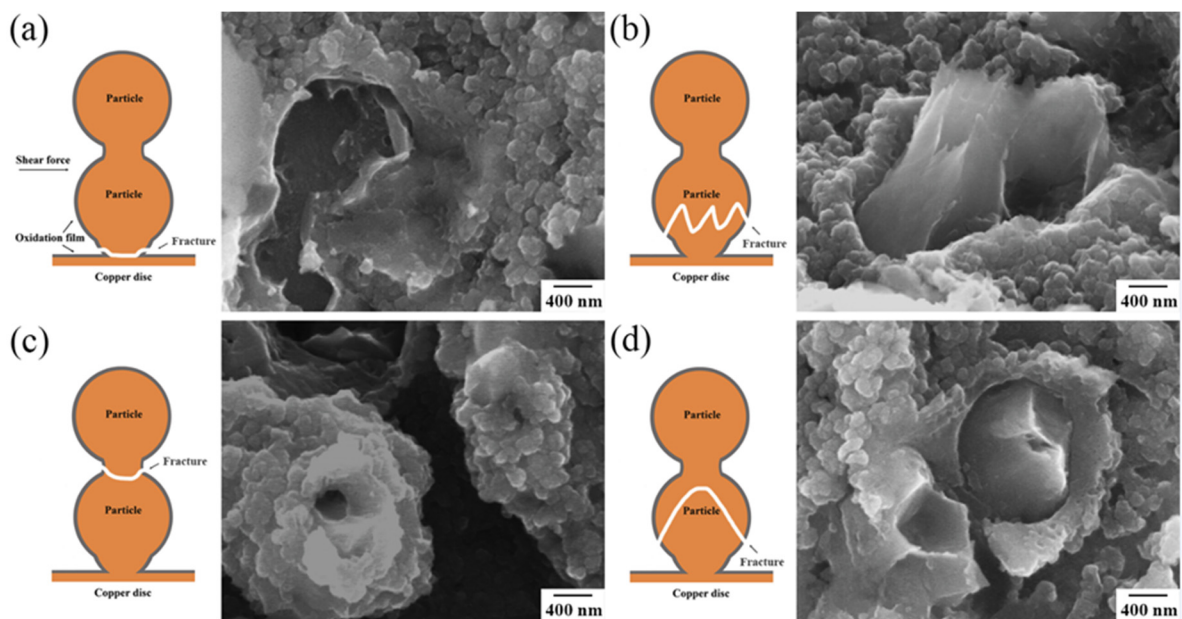


Figure 4. 8 SEM images of fractures between Cu particle and disc (a, b), and between Cu particles (c, d), and corresponding schematic illustration of fracture mode

4.5 Conclusions

In summary, in situ reduction-sintering of CuO nanoparticles by glycerol was proposed to fabricate strong Cu-Cu bonding for power electronics and the formation of oxide was depressed by the rapid sintering speed. The proposed method produces similar shear strengths to Cu nanoparticle sintered joints but without the need for pressurized sintering or protective gas atmospheres. The best shear strength of 22 MPa for the joint was achieved by 15 min pressureless bonding at 220 °C in air which resulted in no Cu oxide structure. The only oxide that formed during bonding was Cu₂O, which shows morphological evolution from a laminar layer structure formed by growth and coalescence of Cu₂O nano-strips to a multiple layer structure formed by crossed and overlapping Cu₂O nano-grains. Brittle fracture at the interface between Cu particles and between Cu particles and disc dominated while ductile fracture inside Cu particles was also found. The Cu₂O layer was a brittle structure with poor bonding to Cu core and disc, and its formation led to decreasing Cu-Cu contact area and joint shear strength.

Chapter 5: In situ reduction-sintering of Cu nanoparticle

5.1 Background

Cu nanoparticles readily oxidize and this significantly depresses their conductivity and sintering ability. Use of an inert atmosphere is the most popular way to prevent Cu nanoparticles from oxidation during sintering [106, 107]. Selective laser sintering with a faster sintering speed than a conventional furnace is another approach to depress Cu nanoparticle oxidation [52, 54]. However, the native oxides on the Cu nanoparticle surface will reduce the reliability of the bonded joint. Reducing gas-assisted sintering (such as formic acid [25, 108], hydrogen [109] and ethanol vapor [110]) or surface acid-pretreating followed by inert gas sintering [22, 24] can achieve high bonding strength joint without Cu oxide, but toxicity or complexity of the gas system may hinder its application in manufacturing.

Surface modification has been proposed to increase the oxidation resistance of Cu nanoparticles. Zuo et al. [73] pushed the oxidation onset temperature of Cu nanoparticles up to 300 °C by phosphating treatment but found that the dense phosphating film may hinder the coalescence of Cu nanoparticles during sintering. A metal core-shell structure has also been proposed to improve the oxidation resistance and sintering ability of Cu micro/nanoparticles, such as Ag [111], Sn [69], and Ni [112] covered. However, the cost of this method is much higher than pure Cu and complex synthesizing process or brittleness of intermetallic compound is also potential problem. Therefore, the problems of sintering Cu nanoparticles arising from oxidation have not been completely solved and require more research.

5.2 Objectives

Although strong Cu-Cu bonding of 22 MPa was achieved by in situ reduction-sintering of CuO nanoparticles in chapter 5, the sintered structure of reduced micron-sized Cu particles shows an insufficient sintering of Cu and little deformation after fracture. This chapter aims to achieve a stronger bonded joint by in situ reduction-sintering of Cu nanoparticles with higher

surface activity. The effect of oxidation on morphology and sinterability of Cu nanoparticles was also investigated.

5.3 Methods

Cu nanoparticles were mixed with glycerol and ethylene glycol to fabricate the reducing paste (gly) and non-reducing paste (eth), respectively. The gly paste was printed on the dummy Cu die surface and then heated for reduction. Following reduction, the dummy Cu die and substrate were bonded with placement pressure of 3 MPa for 1 minute. Next the assemblies were heated to 220 °C for 5 min without pressure in air. Eth paste was printed into the overlap area between the Cu dummies, then the assemblies were heated with the same condition but under 3 MPa sintering pressure. The properties of joint by the reduction-sintering process and traditional sintering process were compared.

5.4 Results and discussion

5.4.1 Growth of Cu oxide during storage in air

The Cu nanoparticles were exposed to air atmosphere for a varying number of weeks (wk) to investigate their oxidation resistance and the nature and extent of oxides formed during exposure. The initial Cu nanoparticles were sealed in a glass bottle without vacuum or inert gas condition, the XRD pattern of the initial Cu nanoparticles (0wk) shows obvious Cu_2O peaks as shown in **Fig. 5. 1 (a)**, which indicates that the Cu nanoparticles were already oxidized to a certain degree. The surface of Cu nanoparticles was also covered by many Cu_2O nanoparticles with a size of about 5nm as shown in **Fig. 5. 1 (b)**. In contrast, the Cu nanoparticles treated by diluted hydrochloric acid show very clean surface. After 1 week air exposure the peaks of Cu_2O almost disappear and clear CuO peaks begin to occur. The shape of the oxide is still spherical and the oxidation film becomes thicker as shown in **Fig. 5. 1 (c)**. At 2 weeks, the peaks of CuO become stronger and the shape of the oxide grains changes from spherical to rod shaped as shown in **Fig. 5. 1 (d)**. Yang et al. [97] also reported a similar morphological change of oxide

on Cu powder surfaces.

The XRD pattern of Cu nanoparticles exposed for 4 weeks shows similar CuO peak intensity to that of 2 weeks, which indicates that there is no apparent increase in the oxidation degree of Cu nanoparticles over this period. This is because the formed oxide layer prevents exposure of Cu surface to oxygen and further oxidation of Cu results from slow diffusion of Cu and oxygen atoms through the oxide layer [100]. As exposure time further rises to 6 weeks, the intensity of CuO peak increases significantly and the oxide nanorods become longer as shown in **Fig. 5. 1 (e)**. The CuO peak intensity does not increase significantly as exposure time rises to 9 weeks.

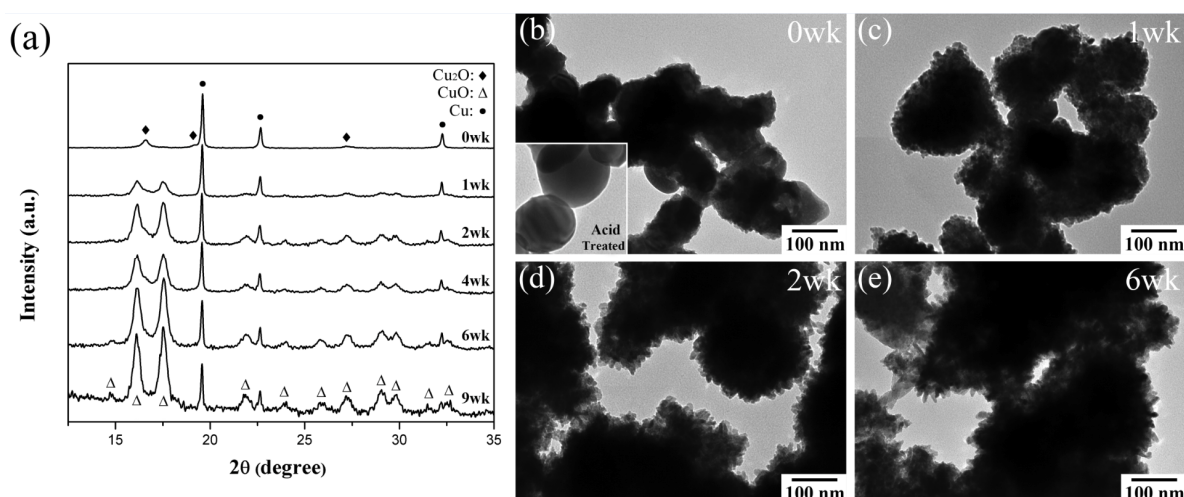


Figure 5. 1 XRD patterns (a) of Cu nanoparticles before and after exposure for different weeks. TEM image of Cu nanoparticles exposed for: (b) 0wk, (c) 1wk, (d) 2wk, (e) 6wk. (Inset image is Cu nanoparticles treated by acid)

5.4.2 Characterization of reduction- sintering structure of Cu nanoparticles

Fig. 5. 2 (a) shows the DSC curves of glycerol mixed with and without CuO nanoparticles, and the curve of ethylene glycol with CuO nanoparticles in air. There is no exothermic peak in the curve of ethylene glycol mixed with CuO nanoparticle and in the curve of glycerol but only an endothermic peak related to the evaporation of solvent. It can be inferred that CuO nanoparticles cannot be reduced by ethylene glycol. In contrast, the exothermic peak at 220 °C in the curve containing CuO nanoparticles in addition to glycerol was caused by the reduction

reaction between glycerol and CuO nanoparticles. The reduction reaction of CuO and Cu₂O by glycerol is presented as follows and the oxidation product of the glycerol molecule may vary according to the degree of oxidation [96]:

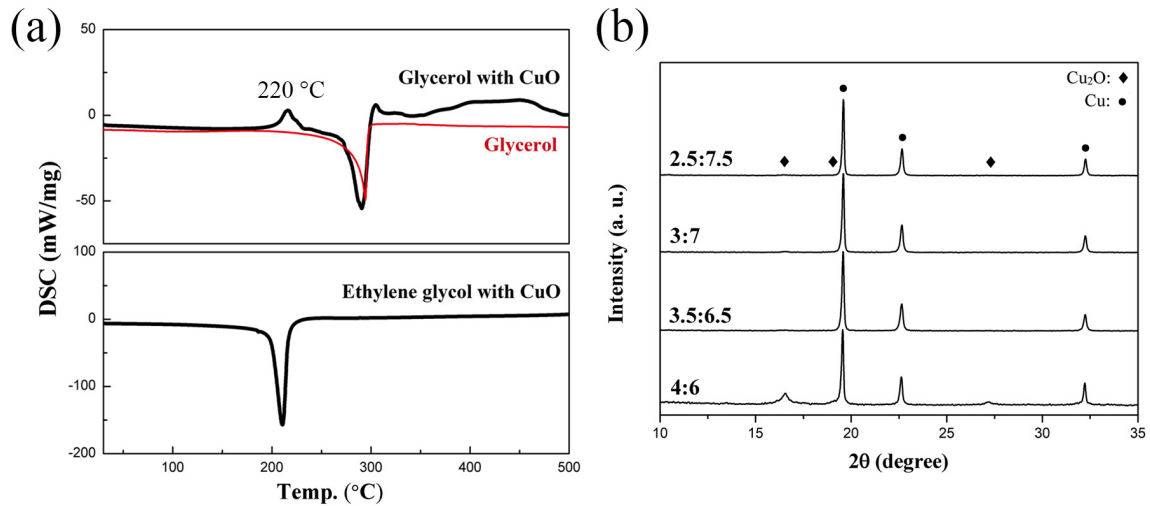


Figure 5. 2 Thermal analysis (a) of glycerol and ethylene glycol with/without CuO nanoparticle. XRD patterns (b) of fracture surfaces of joints with different mass ratios of Cu nanoparticle to glycerol

Cu nanoparticles exposed for 0wk, 1wk, 2wk and 6wk presented were chosen to investigate the effect of oxidation on the reduction-sintering structure of Cu nanoparticles by glycerol. Prior to that, the Cu nanoparticles with most oxide (6wk) were chosen to investigate the suitable mass ratio between Cu nanoparticles and glycerol, as well as the phase composition of reduction-sintering structure. The XRD results of fracture surfaces of joints with differing concentrations of 6wk Cu nanoparticles in the paste is shown in **Fig. 5. 2 (b)**. With low Cu nanoparticles content, only Cu peaks can be detected, which indicates that the oxide on Cu nanoparticle surfaces can be completely reduced to Cu by glycerol. It is also clear that the oxide of Cu nanoparticles for 0wk, 1wk and 2wk can be completely reduced as they contain less oxide content. However, when the mass ratio rises to 40%, obvious Cu₂O peaks began to appear.

Since a higher concentration of Cu nanoparticles leads to more reduced Cu nanoparticles in the paste and a denser sintering structure, the mass ratio of 3.5:6.5 is optimal.

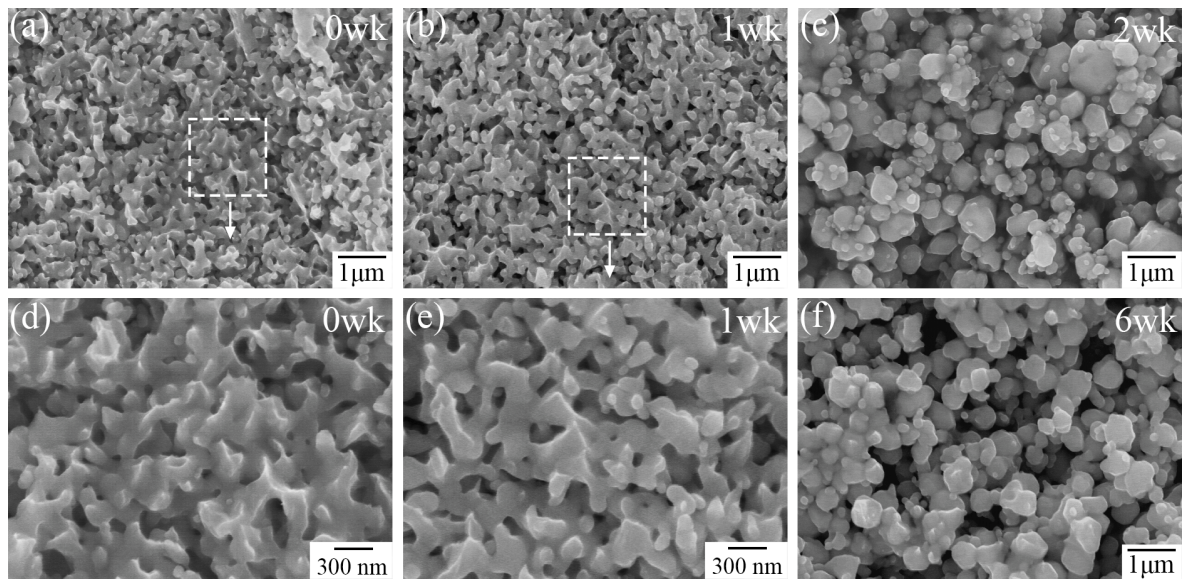


Figure 5. 3 SEM fracture surface of joints by glycerol and Cu nanoparticles exposed for (a, d) 0wk, (b, e) 1wk, (c) 2wk, (f) 6wk

Fig. 5. 3 shows SEM images of fracture surfaces of joints by glycerol and Cu nanoparticles exposed for different weeks. The oxidation film on the surface of Cu nanoparticles of 0w and 1w was reduced by glycerol after reduction and the initial Cu nanoparticles cores exposed and then coalesced together during sintering. The reduced Cu nanoparticles also sintered with the initial Cu nanoparticles cores and make them difficult to be distinguished. However, the size of the reduced Cu nanoparticles is believed to be similar to or lower than that of the initial Cu nanoparticles as there is no larger Cu nanoparticle found in the sintering structure as shown in **Fig. 5. 3 (a)** and **(b)**. The deformation with dimple-like morphology shown in **Fig. 5. 3 (d)** and **(e)** also indicates that the sintering structure of Cu nanoparticles has good strength. In the case of Cu nanoparticles exposed for 2wk and 6wk, the oxidation film was much thicker and more CuO was reduced, allowing the reduced Cu grains to grow to a larger size of about 400 nm as shown in **Fig. 5. 3 (c)** and **(f)**. Some initial Cu nanoparticles cores after reduction were also found in the sintering structure while obvious deformation of sintered Cu was not found.

Since Cu nanoparticles of 2wk and 6wk share a similar reduced sintering structure, Cu nanoparticles of 0wk, 1wk and 2wk were chosen to mix with glycerol and ethylene glycol respectively to fabricate the reducing paste (gly) and non-reducing paste (eth). The shear strengths of joints fabricated with each paste are plotted in **Fig. 5. 4 (a)**. From this plot, it is clear that the joints by gly had a much higher shear strength than the joints by eth and that the joint shear strength decreased with increasing exposure time for both pastes. The Cu nanoparticles with ethylene glycol failed to bond the joint while the joint by glycerol had good strength of about 25 MPa. In the case of glycerol, the increasing size of reduced Cu nanoparticles for longer exposure times decreased the driving force of sintering, which lead to a less dense sintering structure and decreased joint shear strength [29, 113]. Zuo et al. [67] also reported similar result that the joint bonded by 20 nm Cu nanoparticles had a higher shear strength than the joint of 100 nm nanoparticles due to the more densely sintered structure.

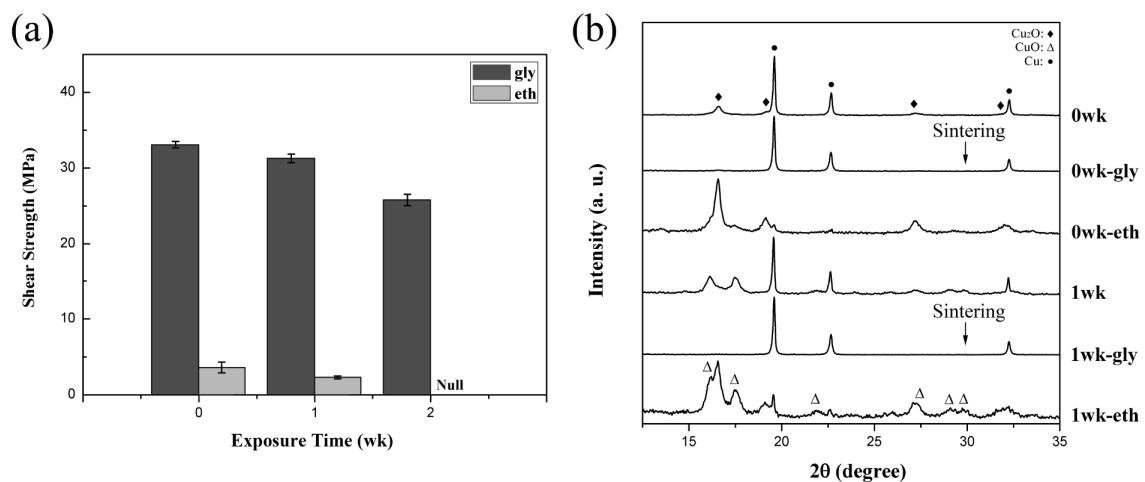


Figure 5. 4 Shear strengths (a) of joints by gly and eth and XRD patterns (b) of joints fracture surface. (Shear tests were performed in five replicates)

The phase composition of fracture surfaces of successfully bonded joints by 0wk and 1wk Cu nanoparticles were analyzed by X-ray diffraction as shown in **Fig. 5. 4 (b)**. The XRD pattern of the gly joint shows no obvious oxide peak, which indicates that the native oxide of Cu nanoparticles was reduced to Cu by glycerol. The oxide didn't re-appear after sintering due to

the merit of in situ reduction-sintering, whereby the Cu nanoparticles can be immediately sintered after reduction at the same temperature. The rapid sintering significantly depresses oxide formation. In contrast, oxide peaks found in sintered Cu nanoparticles with ethylene glycol become much stronger compared with the original Cu nanoparticles. The oxidation film on the Cu nanoparticle surface depress the diffusion of Cu atoms and cause porous sintering structure. The cross section of joints by gly show a highly dense sintering structure, while joints by eth show a porous structure with poor coalescence as shown in **Fig. 5. 5 (g)**.

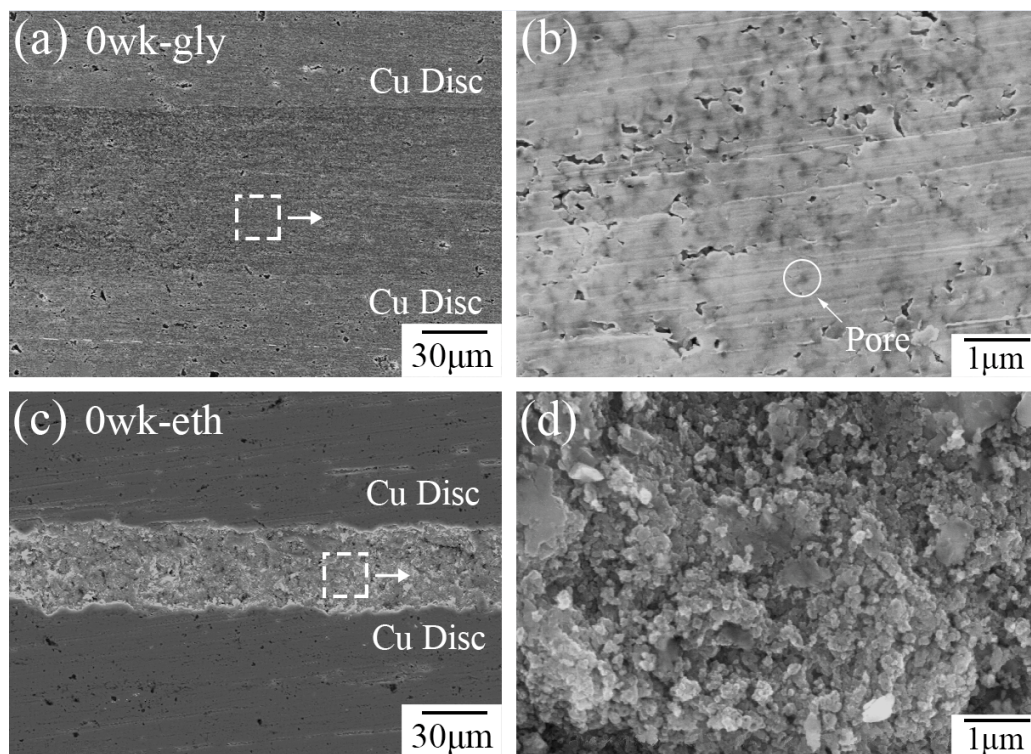


Figure 5. 5 SEM cross section images of joints by glycerol (a, b) and ethylene glycol (c, d) mixed with 0wk exposure Cu nanoparticles, respectively

5.4.3 Consolidation behavior of Cu nanoparticles during sintering

The Cu nanoparticles of 0wk and 2wk were ultrasonically dispersed in ethanol and then printed on Transmission Electron Microscope (TEM) grid. Next the coalescence of Cu nanoparticles was intermittently observed by TEM during the heating process (quasi-in-situ observation). It should be noted that the TEM grid was heated on a hot plate in air rather than

tube furnace to achieve fast heating speed. The air-sintering evolution of Cu nanoparticles at 220 °C is shown in **Fig. 5. 6**. From this plot, it is clear that the 2wk Cu nanoparticles show little deformation after heating, which indicates they cannot be sintered due to the rod shaped oxide. In contrast, significant coalescence between 0wk Cu nanoparticles was found after heating for only 5 min. The “closed loop” pores almost disappeared while there were still tiny pores even after 20 min heating. Meanwhile, the dislocations were found in sintered nanoparticle after 10 min heating while they later disappeared due to relocation of mislocated Cu atoms [80] and other new dislocations formed as shown in the inset image of **Fig. 5. 6 (g) and (h)**. These results indicate that Cu nanoparticles can be quickly sintered with high sintering density at 220 °C. Prolonging the heating time leads to the formation of dislocations in sintered Cu but no further densification, and it will also result in more Cu oxidation. Cheng et al. [38] found similar results that the shrinkage of Cu nanoparticles rises at first and remains stable with increasing time during sintering for low temperature ($T \leq 900\text{K}$) and further densification of sintering structure can be facilitated by higher temperature..

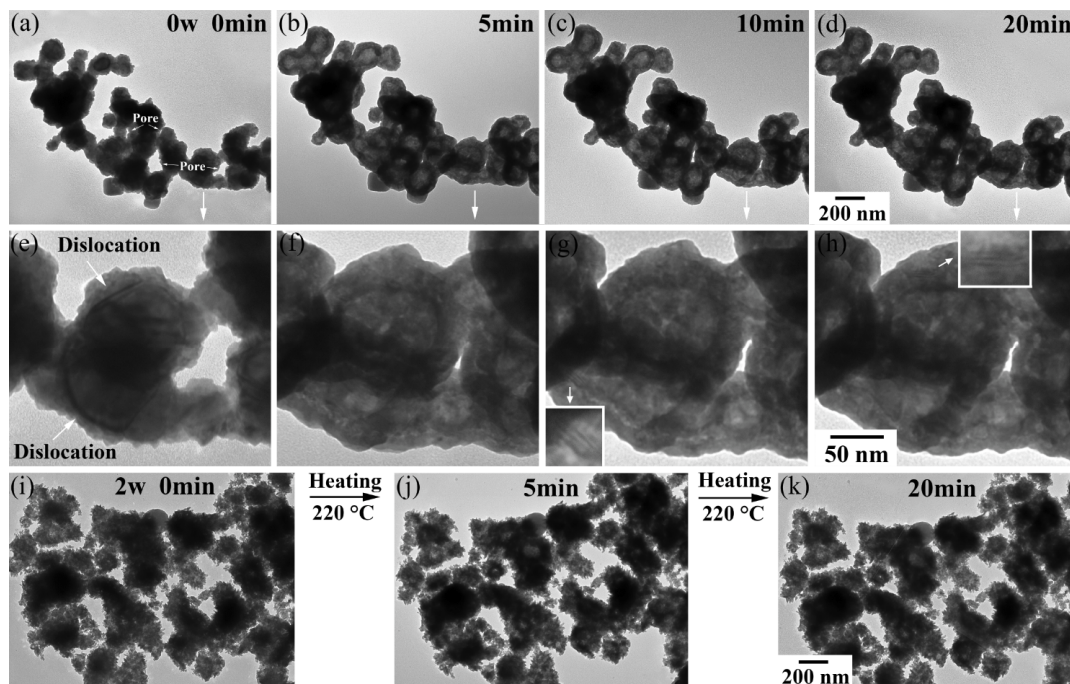


Figure 5. 6 TEM images of consolidation behavior of Cu nanoparticles of 0wk (a-h) and 2wk (i-k) during air-sintering

5.5 Conclusions

In summary, rapid and pressureless in situ reduction-sintering reduced the oxide on Cu nanoparticle surface and depressed its re-appearing and fabricated high bonding strength joint of over 30 MPa at 220 °C in air. The Cu nanoparticles were sufficiently sintered and show dimple-like deformation after fracture. The Cu nanoparticles with the rod shaped oxide cannot be sintered by traditional pressure-assisted sintering while the oxidized nanoparticles treated by in situ reduction-sintering had good sintering strength. This bonding process omits special sintering and storing conditions of Cu nanoparticles and presents a promising bonding technology for power electronics.

Chapter 6: Quasi-in-situ observation of the grain growth and grain boundary movement during sintering

6.1 Background

Sintered Cu interconnection for power electronics has attracted considerable interest recently. Investigation of grain growth during Cu nanoparticle sintering provides insight into the strengthening mechanism of the sintered structure. Currently, the literature on Cu nanoparticle sintering mechanism is limited and mainly focuses on the transmission electron microscopy (TEM) observation of a limited number of nanoparticles with an ultrathin region. It was found that particles undergo an alignment process through rigid body rotation to match their orientation prior to or during attachment, this alignment process is kinetically driven by the reduction of interfacial energy [114-117]. In some cases, perfectly aligned and coherent particles would occur. Aabdin et al. [116] found that there is a critical misalignment angle ($\sim 15^\circ$) for gold nanoparticle coalescence. Beyond this critical angle, the nanoparticles fail to correct misalignment during oriented attachment and this results in the bonding interface consisted of GB defects. Lange et al. [117] reported a found a defect mediated co-alignment process by Molecular Dynamics simulation. The dislocations were found to form at the interface of coalesced gold nanoparticles after imperfect oriented attachment and they later dissociate and glide through the adjacent particles, which removes the associated strain at the interface and leads to additional co-alignment. However, these studies are mainly focused on the early stage sintering behavior of a limited number of nanoparticles within a very thin region below 200 nm thickness (or even 10 nm for high resolution) due to the limitation of TEM observation. The sintering mechanism involving numerous particles could be more complex and requires more research. Meanwhile, the coalescence process of Cu nanoparticles and substrate is rarely reported.

6.2 Objectives

This chapter aims to investigate the mechanism of grain growth and twin formation in the bulk sintered Cu nanoparticles (refer to chapter 6) by using a quasi-in-situ method combining SEM observation and ion beam etching. The effect of sintering conditions on grain and pore size, porosity and strength of the sintered structure and the micro-fracture mechanism of the joint were investigated. A model of the sintering diffusion mechanism is proposed. The mechanism of GB movement across sintered Cu grains and Cu substrate grains and the relevant strengthening mechanism on joint strength were also studied.

6.3 Methods

Cu nanoparticles and glycerol were mixed to fabricate the reducing paste. After the reduction and pre-bonding process in Chapter 5, the assemblies were heated to different sintering conditions as shown in **Table 4. 1** without pressure in N₂. The BSE cross section images of joint were used to measure the grain size and pore size/number/shape of sintered Cu structure. The joint cross section was intermittently observed by combining SEM and ion beam miller during the heating process (quasi-in-situ observation) to study the mechanism of grain growth and twin formation. The same joint was slightly etched by ion beam milling after every heating step so that the GB could be clearly seen.

6.4 Results and discussion

6.4.1 Effect of sintering temperature on microstructure

Fig. 6. 1 (a) shows the XRD results (Mo radiation) of Cu nanoparticles before and after reduction. The Cu₂O peaks of the initial Cu nanoparticles disappear and only Cu peaks remain after reduction, which indicates that Cu oxides were completely reduced to Cu by glycerol. The oxygen content of sintered Cu structure was also measured by the EDS and the relevant results show that the contents of organic residue and oxide are limited (see Fig. A5-6 in Appendix). The sintering process was then carried out under N₂ atmosphere to avoid Cu oxidation. The

joints were bonded at different temperatures for 5 min to investigate the effect of temperature on grain and pore size, porosity and strength of the sintered Cu nanoparticle structure. With increasing temperature, the grain size increases from 150 nm of 220 °C to 279 nm of 310 °C as shown in **Fig. 6. 1**. Wang et al. [39] found a similar result on the variation of sintered nanoparticle grain size distribution with increasing temperature. Both the porosity of the sintered structure and the bonding interface decrease significantly at first and then the rate of decrease levels off after the temperature increases to 280 °C. Kozawa and Yanagisawa [118] reported a similar result on trends of both grain size and porosity with temperature. The pore size changes little with the sintering temperature as shown in **Fig. 6. 1 (c)**. However, the pore number in an area of 1 μm^2 decreases significantly from 9.08 at 220 °C to 4.52 at 310 °C, which is responsible for the decreasing porosity. Meanwhile, the pore shape shows an obvious trend of being isolated and spherical as shown in **Fig. 6. 1 (d-g)**, which is a sign of the final sintering stage. The pore shape distribution in Figure A7 of Appendix also shows that the number of irregular pores decreases significantly. The increment of grain size and density can be attributed to the higher sintering driving force arising from increasing temperature. The shear strength of joints increases with increasing temperature as shown in **Fig. 6. 1 (c)** which is in good agreement with the porosity result. Decreasing porosity leads to more contact area between Cu nanoparticles and Cu die/substrate and higher sintering strength. **Fig. 6. 1 (d-g)** show SEM images of fracture surface of joints for different temperatures. The fracture surfaces of joints for all bonding temperatures show deformation with dimple-like morphology which represents a ductile fracture of sintered Cu structure and this indicates that strong bonding was achieved [20]. The deformation degree (elongation) of sintered Cu increases with increasing the sintering temperature and results in higher joint bond strength. The relevant force-displacement curves (see Fig. A11 Appendix) also show an increasing elongation as the moving distance of shear tool increases obviously with the sintering temperature.

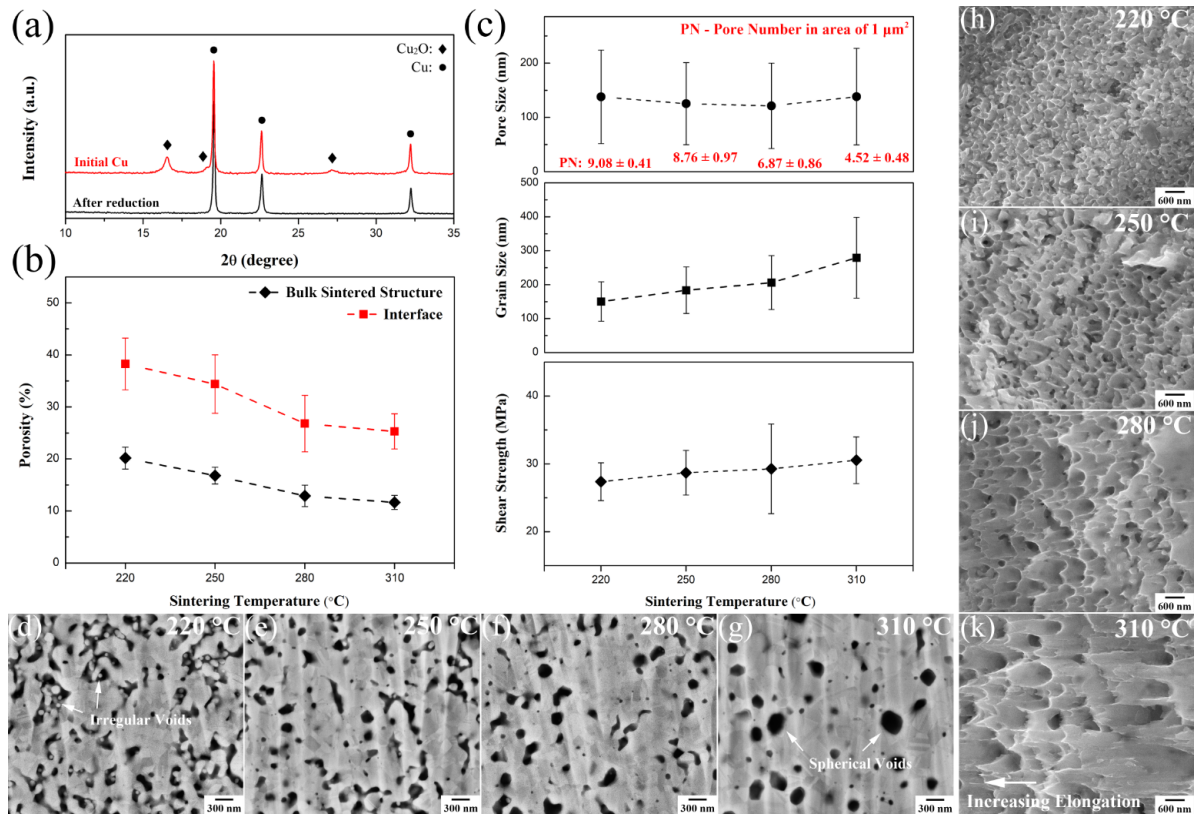


Figure 6.1 XRD patterns (a) of Cu nanoparticles before and after reduction. Variation in porosity of bulk sintered Cu structure and interface (b), pore size/number and grain size of the bulk sintered structure and shear strength of joints (c) due to different temperatures (each for 5 min). Corresponding SEM cross section (d-g) and fracture surface images (h-k) of joints. (SEM cross section images of three replicates were used for measurement and shear tests were performed in five replicates)

6.4.2 Effect of sintering duration on microstructure

The joints were also bonded at the lowest and highest temperatures of 220 °C and 310 °C for different times to investigate the effect of duration on grain and pore size, porosity and strength of the sintered Cu nanoparticle structure. The grain size remains almost unchanged with increasing times at 220 °C as shown in **Fig. 6.2**, which indicates that the activation of grain growth requires a higher temperature. However, holding at 220 °C can still activate the atomic diffusion between Cu nanoparticles and increase density of both bulk and interfacial sintered structure and the joint shear strength. The pore number increases slightly while the

pore size decreases significantly from 137.90 nm at 5 min to 99.70 nm at 20 min, and this results in the decreasing porosity. Most of the large and irregular pores disappear at 20 min and some of them become isolated and spherical as shown in **Fig. 6. 2 (i)**, and the pore size and shape distribution in Figure A8 of Appendix also confirm that. The deformation degree of sintered Cu nanoparticles increases with increasing time as shown in **Fig. 6. 2 (c-e)**, which is in good agreement with the strength result. When holding at 310 °C, the grain size similarly shows little change as shown in **Fig. 6. 2**. The sintering stress σ arises from interfacial energies, also referred to sintering driving force, can be defined by [119]:

$$\sigma = \frac{6\gamma}{G} (1 - \rho)^2 \quad (11)$$

where γ is surface tension energy, G is mean grain size and ρ is porosity. Although 310 °C is much higher than 220 °C, the grains at 310 °C are also much larger (almost a factor of 2) and further grain growth requires a higher temperature.

Unlike the progressively decreasing porosity at 220 °C, the interface porosity at 310 °C only decreases when sintering time increases from 5 min to 10 min, the sintered structure porosities for different time show little difference as shown in **Fig. 6. 2 (a)**. This porosity result also shows a good agreement with the insignificant change of pore size and number also pore size and shape distribution (see detail in Figure A9 of Appendix). Hu et al. [120] also found that the sintering porosity decreases first with holding time and then becomes stable. The deformation degree of sintered Cu nanoparticles with different time at 310 °C also remains almost unchanged as shown in **Fig. 6. 2 (f-h)**. The grain size and porosity at 310 °C change little with increasing time, but the joint shear strength keeps increasing and the possible reason will be discussed in Section 7.3.7. The statistical significance of these parameters is also analyzed by T-test and can be seen in Appendix.

The joints sintered at 220 °C for 20 min and 310 °C for 10 min share similar porosity in the bulk sintered structure (12.7% and 11.1%) and interface (22.1% and 22.6%). The grains of

310 °C are almost twice as large as the grains of 220 °C and the pore size is also larger as shown in **Fig. 6. 2 (i-j)**. However, the shear strength of joints at 220 °C/20 min is 30.88 MPa which is similar to the joint strength of 30.69 MPa at 310 °C/10 min. It can be inferred that porosity is the most important factor of joint strength and grain or pore size does not play a significant role. The porosity and strength of sintered Cu structure can be effectively improved by increasing sintering time at low temperature which is better for manufacturing, as high processing temperature could increase the cost and damage some temperature sensitive devices.

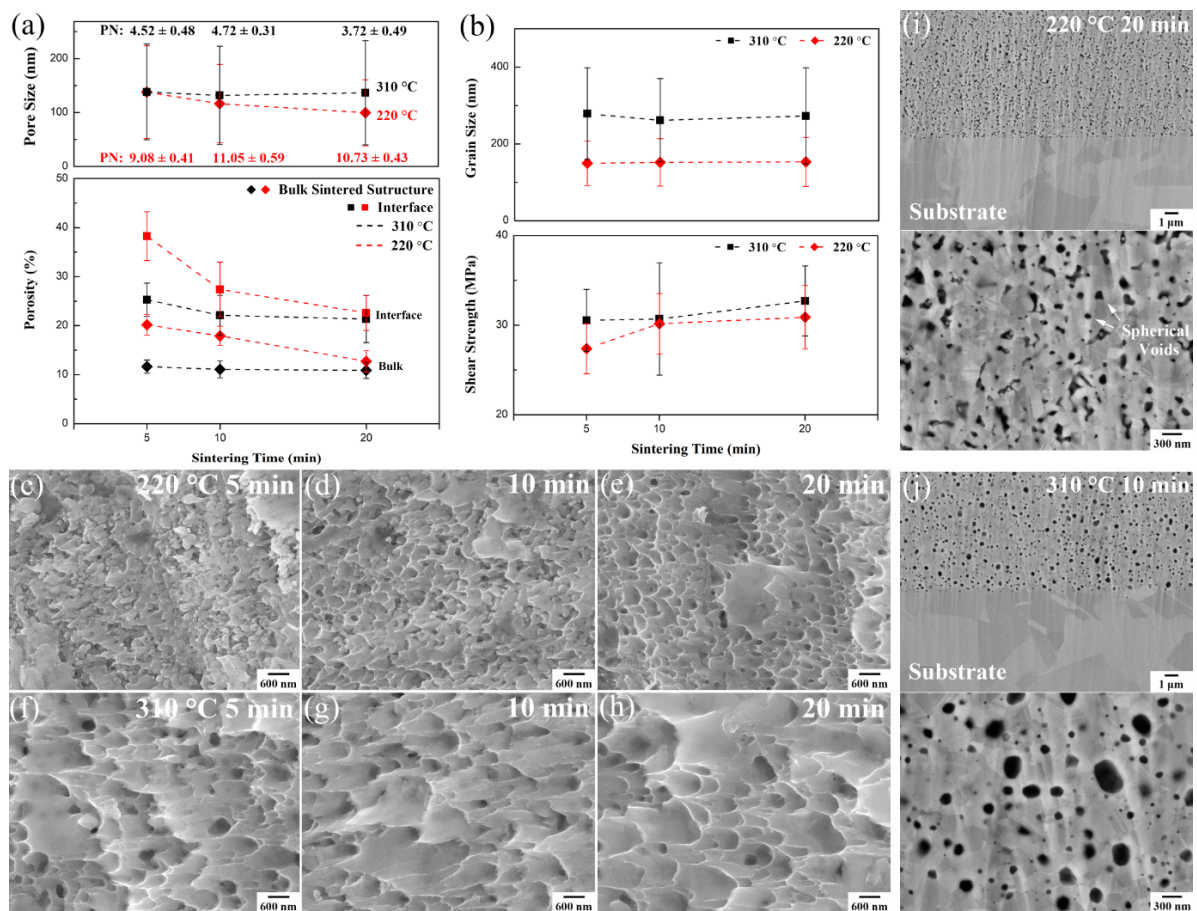


Figure 6. 2 Variation in pore size/number and porosity of the bulk sintered Cu structure and interface (a), and grain size of the bulk sintered structure and shear strength of joints (b) due to different time at 220 °C and 310 °C. Corresponding SEM fracture surface images (c-h) of joints. Comparison of sintered structure at 220 °C/20 min (i) and 310 °C/10 min (j). (SEM cross section images of three replicates were used for measurement and shear tests were performed in five replicates)

6.4.3 Sintering mechanism and modeling

The sintering process can be divided into three stages: the initial stage with neck growth and minor densification, the intermediate stage with grain growth and significant densification, and the final stage with isolated and spherical pores and low densification rate. In high temperature (over 800 °C) and pressure sintering over several hours duration [118, 121], the sintered particle density can reach near bulk material values. The sintering process in this study was carried out under zero pressure and low temperature (below 310 °C). The porosity in the sintered Cu only increases 0.2% from 310 °C/10 min (11.1%) to 310 °C/20 min (10.9%), which indicates that the lowest achievable porosity ρ_l is near to 11% at sintering temperature (310 °C).

A two particle sintering model was used in this study and the particles were assumed to be slightly attached in the necking area at the beginning of sintering as shown in **Fig. 6.3 (a)**. To simplify the simulation, the area outside the necking area was assumed to be triangle as indicated by red line in **Fig. 6.3 (a)** and the movement ΔL of particle centers was neglected. For the case of mass transport to the neck by GB diffusion, the growth rate of sintering neck can be given by [122]:

$$\frac{x}{a} = \left(\frac{96D_{gb}\gamma\Omega\delta_{gb}}{kT a^4} \right)^{1/6} t^{1/6} \quad (12)$$

For the case of surface diffusion:

$$\frac{x}{a} = \left(\frac{56D_s\gamma\Omega\delta_s}{kT a^4} \right)^{1/7} t^{1/7} \quad (13)$$

For the case of lattice diffusion through GB:

$$\frac{x}{a} = \left(\frac{80\pi D_l\gamma\Omega}{kT a^3} \right)^{1/5} t^{1/5} \quad (14)$$

Where a is particle radius, D_{gb} , D_s and D_l are the diffusion coefficients for GB, surface and lattice diffusion, k is Boltzmann constant, Ω is volume of the diffusing vacancy, δ_{gb} and δ_s are

the thickness for GB and surface diffusion, T is the temperature. The pore area P_x outside sintering neck and porosity ρ can be given by:

$$P_x = 2a^2 - 2ax \quad (15)$$

$$\rho = \frac{P_l + P_x}{8a^2}, P_l = 8a^2\rho_l \quad (16)$$

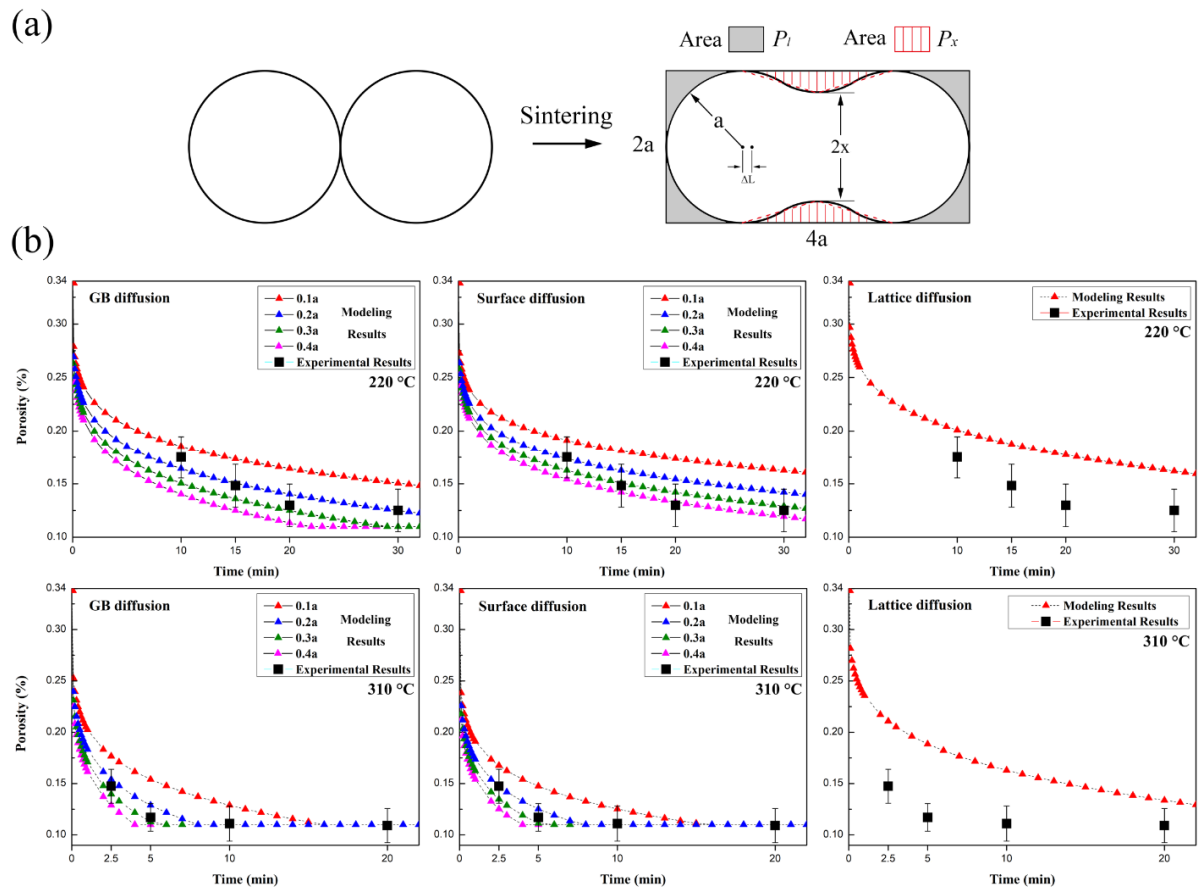


Figure 6. 3 Schematic illustration (a) of two particle sintering model and comparison (b) of bulk sintered structure porosity of experimental results and modeling prediction due to different diffusion method (0.1a-0.4a represent the diffusion thickness δ)

The porosity ρ was assumed to remain unchanged when it attains the lowest porosity ρ_l which is assumed to be 11%. The porosity 34% of the sintered structure at 0 min (just after reduction) was measured and the porosity 20.2% at 220 °C/5 min was used to calculate the relevant parameters (i.e. D , γ , Ω). The experimental porosity results of other sintering conditions were compared with the modeling prediction based on equation (8) as shown in **Fig.**

6.3 (b). It is clear that the modeling curves of GB and surface diffusion whether at 220 °C or 310 °C fit better with the experimental results than the curve of lattice diffusion, which indicates that GB and surface diffusion are the main diffusion method during Cu nanoparticle sintering. The activation energy of lattice diffusion is higher than that of GB or surface diffusion and requires higher temperature. Meanwhile, the modeling curves with $0.2a$ thickness at 220 °C and $0.3a$ thickness at 310 °C in the GB diffusion mode show the best fit with the experimental results. It can be inferred that GB diffusion dominates during Cu nanoparticle sintering under 310 °C.

6.4.4 Fracture mechanism of joint

A joint with representative fracture surface (bonded at 220 °C for 20 min) was selected to investigate the micro-fracture mechanism of joint. Different areas of Cu substrate and their corresponding areas on Cu die were both observed as shown in **Fig. 6.4** (see more fracture surface images of joint with different sintering conditions in Appendix Figure A12-13). It is clear that sintered Cu was attached to both the surface of Cu die and substrate after fracture. The fracture surfaces are seen to lie adjacent to either the die or substrate interfaces, such that there are few areas where the fracture occurs in the bulk sintered structure. The sintered Cu adhering to the Cu substrate shows plastic deformation with dimple-like morphology as shown in **Fig. 6.4 (b)**. However, a very thin sintered layer with similar plastic deformation was also found on the corresponding detached area of Cu die as shown in **Fig. 6.4 (e)**. It can be inferred that the fracture indeed occurs within the sintered structure near to the interface and the sintered Cu at the interfaces is plastically deformed. Meanwhile, some sintered Cu nanoparticles adhering to the Cu die/substrate also show little deformation as shown in **Fig. 6.4 (c)**. These indicate areas of poor bonding between the sintered Cu structure and the bonding surfaces. The representative fracture crack path at the interface in **Fig. 6.4 (f)** also indicates that the joint fracture mainly occurs within the bulk sintered Cu and the sintered Cu nanoparticles are

plastically deformed.

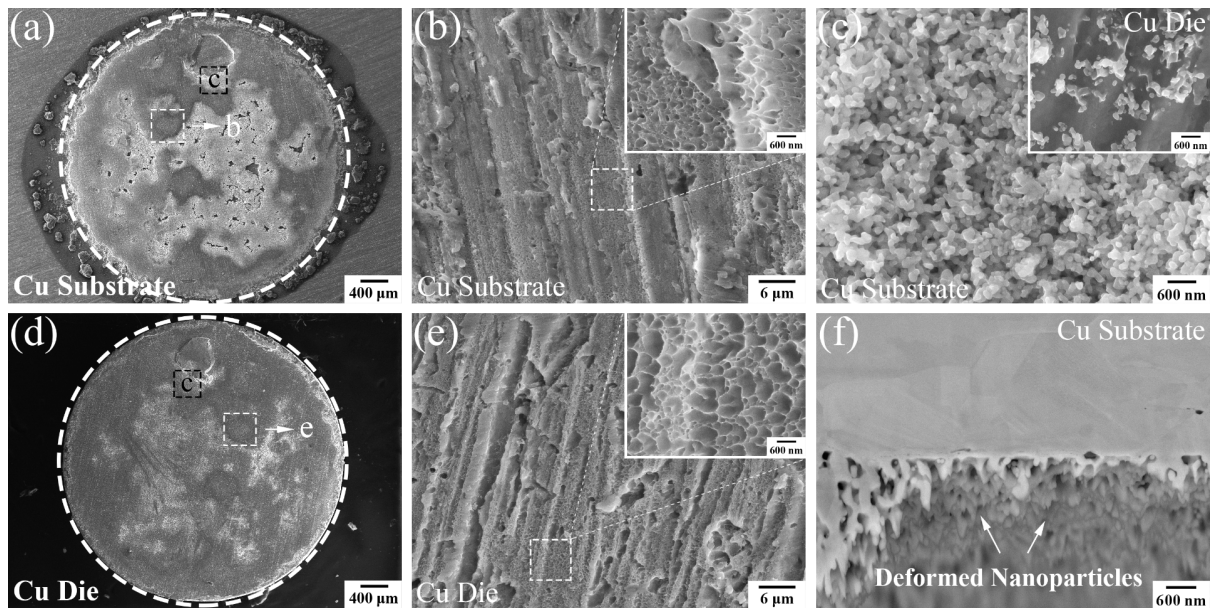


Figure 6. 4 Representative SEM fracture surface image of joint bonded at 220 °C for 20 min. Areas on Cu substrate: (a), (b) and (c), corresponding areas on Cu die: (d), (e) and the inset of (c). Representative SEM fracture image of joint cross section (f)

6.4.5 Grain growth during sintering

The grain growth behavior during sintering was studied by combining SEM observation and ion beam etching. According to the statistics of grain size presented in Section 7.3.2, grains finish growing very fast (within 5 min) during sintering and then stop growing when the holding time is further increased, whether at 220 °C or 310 °C. The SEM observation shows similar result as shown in **Fig. 6. 5**. However, twin I with a diameter about 100 nm and grain II with a diameter about 50 nm in **Fig. 6. 5 (a1)** grow slightly by absorbing part of surrounding grains. Although the mean grain size will not increase significantly during constant temperature heating, some small grains can still grow due to high grain surface activity. In contrast, those larger twins or grains shows little change when holding at 220 °C or 310 °C.

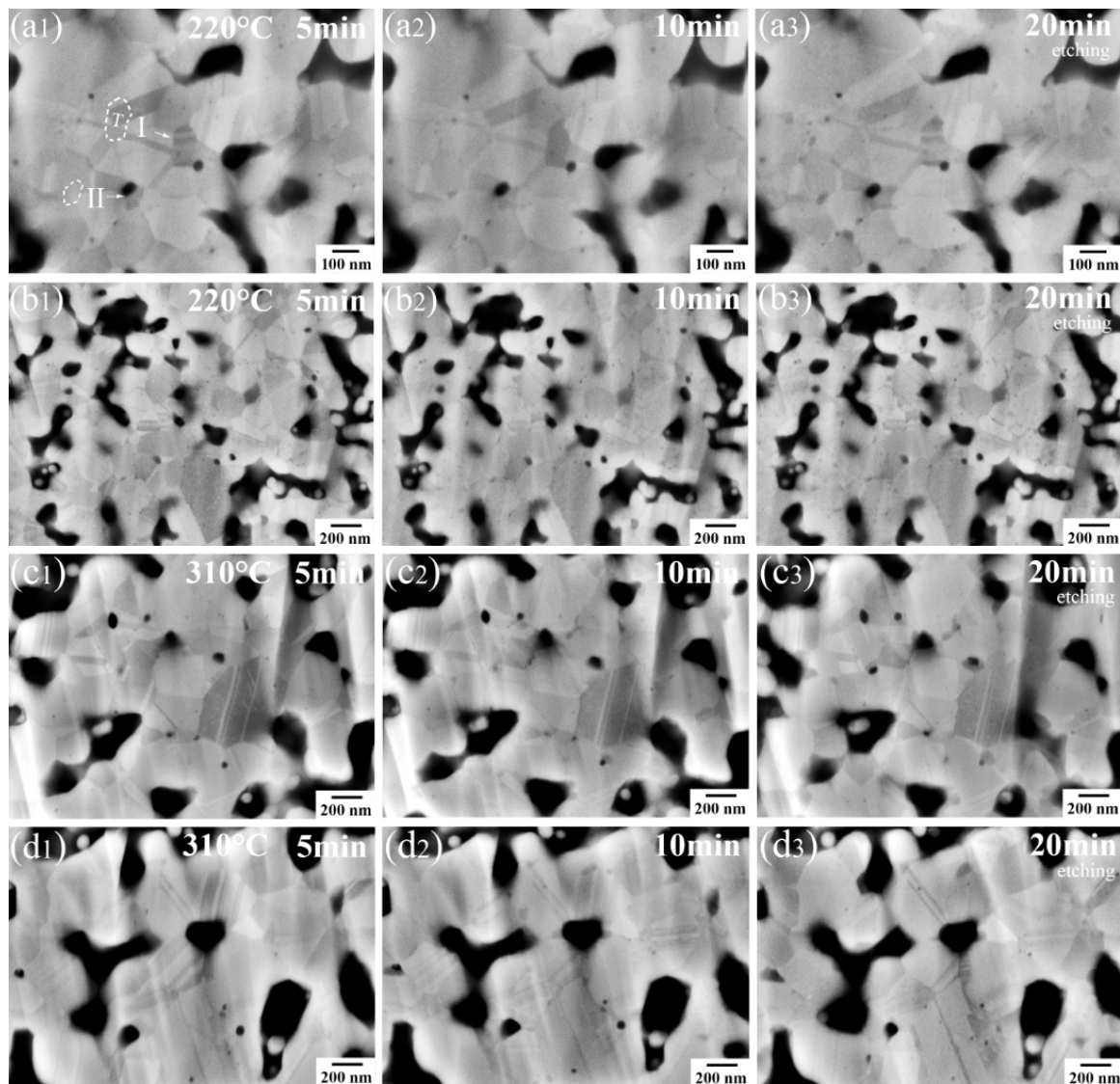


Figure 6. 5 Time sequences of SEM observation showing sintering of Cu nanoparticles at 220 °C (a-b) and 310 °C (c-d). Grain size and boundary remain unchanged after heating and only twin (T) I and grain (II) in (a1) grows a little

Fig. 6. 6 shows the process of grain growth during elevated temperature heating. The grains show different brightness in the BSE images due to different grain orientation. It can be clearly seen in **Fig. 6. 6 (a)** that two black grains I and II grow by transforming the grey grains on their right into black grains first, which represents similar orientation to their own. These grains then merge together into two bigger black grey grains. The color of the left grey grains also becomes black grey while the GB remains. It can be deduced that the crystal structure of these

misorientation grains undergoes different degrees of re-arrangement during sintering and the final orientation tends to be consistent. This further co-alignment of grain orientation could be caused by GB migration or dislocation motion at the interface [116, 117].

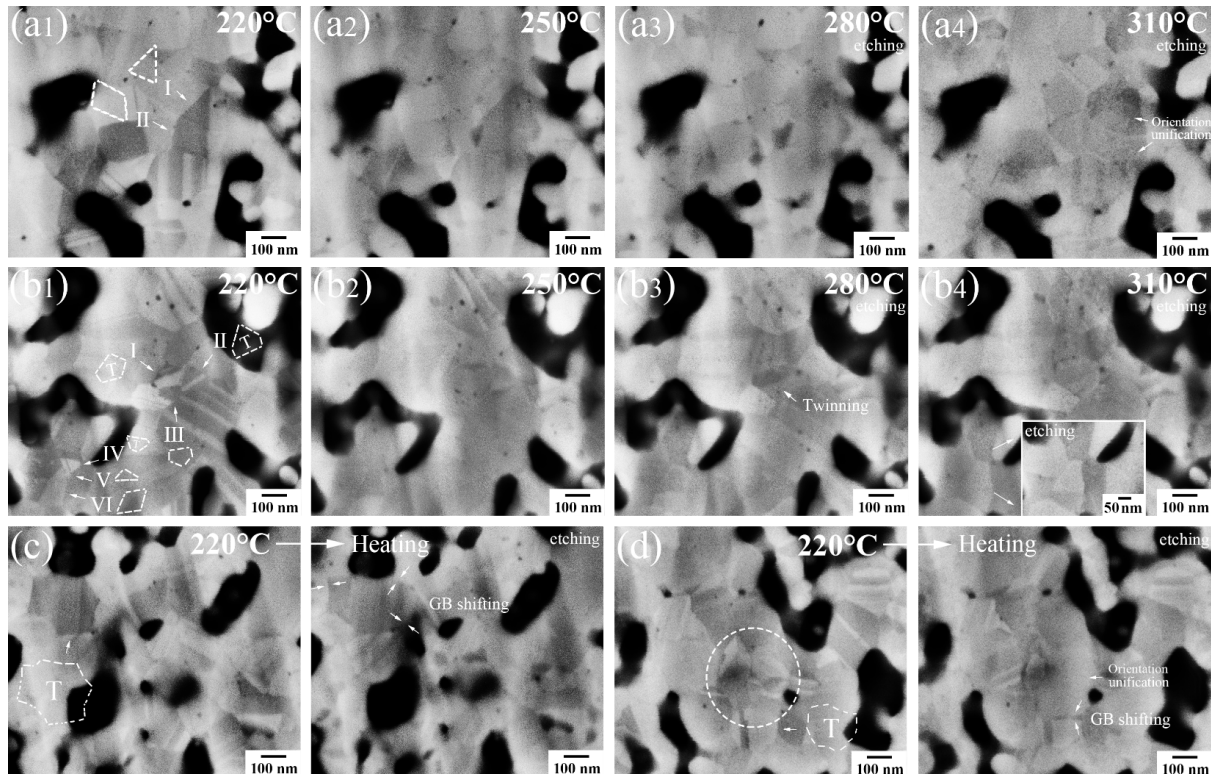


Figure 6. 6 Sequence of SEM observation showing sintering of Cu nanoparticles at elevated temperature (each for 5min). Grains with different orientation (a) as indicated by different brightness undergo orientation unification during coalescences, incomplete orientation unification causes twinning (b), larger grains (c-d) assimilate smaller grains

At the beginning of sintering, particles tend to reorient themselves through another way of rigid body rotation to match their orientation according to both simulation and experimental reports [123, 124]. Zhang et al. [125] observed the sintering behavior of two small nanoparticles and a larger one with special twin structure by in situ TEM exposure. These three nanoparticles were initially misaligned after attachment and they later deformed and rotated for co-alignment of particle orientation. The twin particle finally assimilated one small particle when they shared same orientation, while another small particle retained due to slight

misorientation. Their result is very similar to the growth behavior of twin particle as shown in **Fig. 6. 6 (c)**, where the twin assimilates the small grains on the right and the left grain remains.

Fig. 6. 6 (b) show another sintering process of twin I and II and grain III with different orientation. The color of these particles all turn to black grey after heating to 250 °C and these particles later coalesced together into a larger twin particle as shown in **Fig. 6. 6 (b4)**. Lange et al. [117] reported a deformation of twinning occurred after neck formation in two coalesced nanoparticles with different orientation. According to their result, the particle grows by creating a deformed region within other attached particles. The atomic columns in this region becomes disordered first and then develops the same orientation of this growing particle, which results in different orientations of deformed and un-deformed regions. This incomplete orientation unification results in the formation of twins at the region interface. The formation of twin structure is driven by decreasing total interfacial energy and can also be seen in other research [114, 126, 127]. The misaligned and disordered degree of original particle orientation is critical in twin formation. In contrast, the coalescence of twin IV and grain V and VI in **Fig. 6. 6 (b1)** or several grains as indicated by white dash lines in **Fig. 6. 6 (d)** only produces a larger grain.

Most of current research on metal nanoparticle coalescence were conducted using in situ TEM heating or electron beam exposure [114, 116, 117, 125, 128]. These studies are mainly focused on the early stage sintering behavior of a limited number of nanoparticles and these nanoparticles on a TEM sample grid are usually mobile. There is also a limitation on TEM sample thickness (below 200nm). This study bridges the gap between those small-scale studies and macroscale studies, concentrating on the intermediate and latter stage sintering mechanisms involving numerous particles. In summary, grains tend to grow by merging with other similar-sized grains and the crystal structure of final grain depends on the orientation unification degree as shown in **Fig. 6. 6 (a-b)**. The larger grain will retain its original crystal structure and further grow by assimilating the whole or parts of other smaller grains as shown

in **Fig. 6. 6 (c-d)**. The thermodynamic driving force for particle coalescence is the reduction in surface energy. At the early sintering stage, particles are mobile and may deform or rotate to achieve orientation unification. Particle rotation during or following attachment may not appear in high temperature (over 800 °C) sintering as the enhanced diffusion could relieve the strain at the interface before rotation occurs. At the intermediate and latter sintering stage, GB migration or dislocation motion at the interface could lead to further co-alignment to correct the misorientation. Lange et al. [117] found the presence of dislocation nodes after imperfect orientation attachment at the interface of coalesced particles with misorientation. They reported that these dislocations would be either sessile or dissociated and glide through the adjacent particles which is driven by the surface stress in the neck groove.

6.4.6 Twin growth during sintering

It has been demonstrated that the introduction of high density twins can significantly enhance the strength of polycrystalline copper due to the effective blockage of dislocation motion by numerous coherent twin boundaries [127, 129]. However, from the statistics of twin numbers in sintered Cu nanoparticles as shown in **Fig. 6. 7 (a-b)**, it is clear that there is a small difference (below 7%) between the twin percentages (twin number/twin and grain number) of different sintering conditions. The twin percentage remains relatively constant in the sintered Cu structure when holding at 220 °C or 310 °C as the grains do not grow significantly in these situations. During a rising temperature heating, the grains and twins will coalesce together and grow into one larger grain or twin, which results in more variable twin percentage curve. It can be also seen in **Fig. 6. 5** and **Fig. 6. 6** that the twin structure of grain won't change after heating without coalescence. This is different to the single particle observation reported by Zhong et al. [80] that the twin structure disappeared after heating due to the re-arrangement of atoms. Misorientation between grains formed during coalescence can produce twinning as shown in **Fig. 6. 6 (b)** and **Fig. 6. 7 (d-e)**. The twin grain can also assimilate nearby grains and

transform their crystal structure into twins as shown in **Fig. 6. 6 (c)** and **Fig. 6. 7 (c)**.

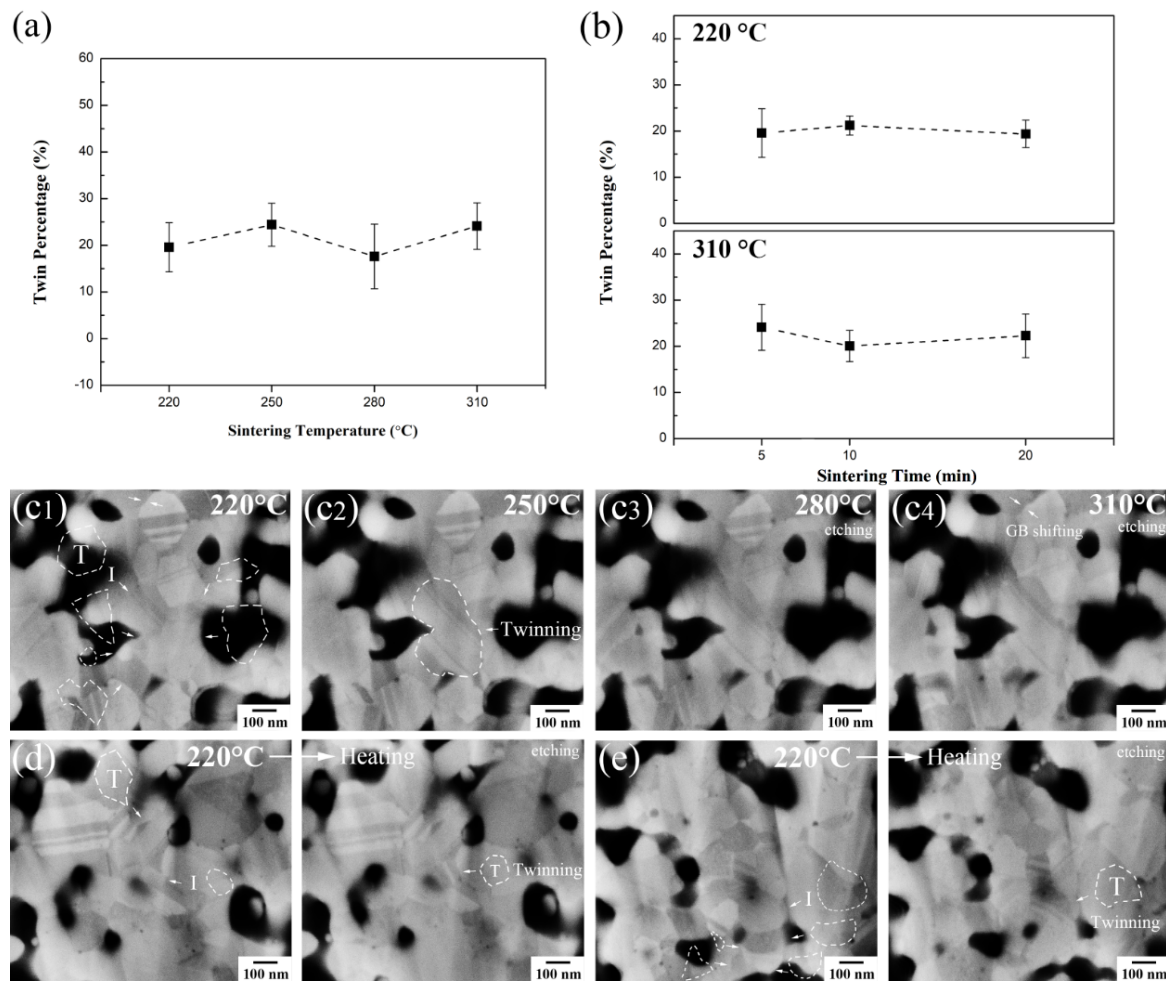


Figure 6. 7 Twin percentage (a-b) in sintered Cu for different conditions. Sequence of SEM observation showing sintering of Cu nanoparticles (c-e) at elevated temperature (each for 5min). Twinning occurs in the assimilation of grains by twin particle (c). Twin forms (d-e) during coalescence due to incomplete orientation unification

6.4.7 Grain boundary shifting during sintering

The coalescence behavior of Cu nanoparticles and Cu die/substrate surface was investigated as shown in **Fig. 6. 8**. One can easily distinguish the initial bonding interface by the coherent large voids at the interface and it was found that some tiny voids in **Fig. 6. 8 (a1)** are distributed in a line along the initial interface. The GB between the sintered Cu and Cu die grains barely move either at elevated temperature or during increasing time at 220 °C, and only one GB in

Fig. 6. 8 (b1) shows a little shifting after heating at 310 °C. However, it was found that some GBs as indicated by white arrows in **Fig. 6. 8 (a1), (c1)** and **(d1)** move away from the initial interface towards the sintered Cu side, which indicates that these larger Cu die grains have assimilated smaller sintered Cu grains during the early sintering stage. Zhong et al. [80] and Fang et al. [130] also found the growth of larger particles is accompanied by the shrinkage of smaller particles during sintering. This can be explained by the Ostwald ripening phenomenon, which leads to the dissolution of smaller solid grains and re-precipitation at regions of larger energetically favored solid grains [131]. Meanwhile, a small number of GBs were also found to move towards Cu die side as shown in **Fig. 6. 9 (a)**.

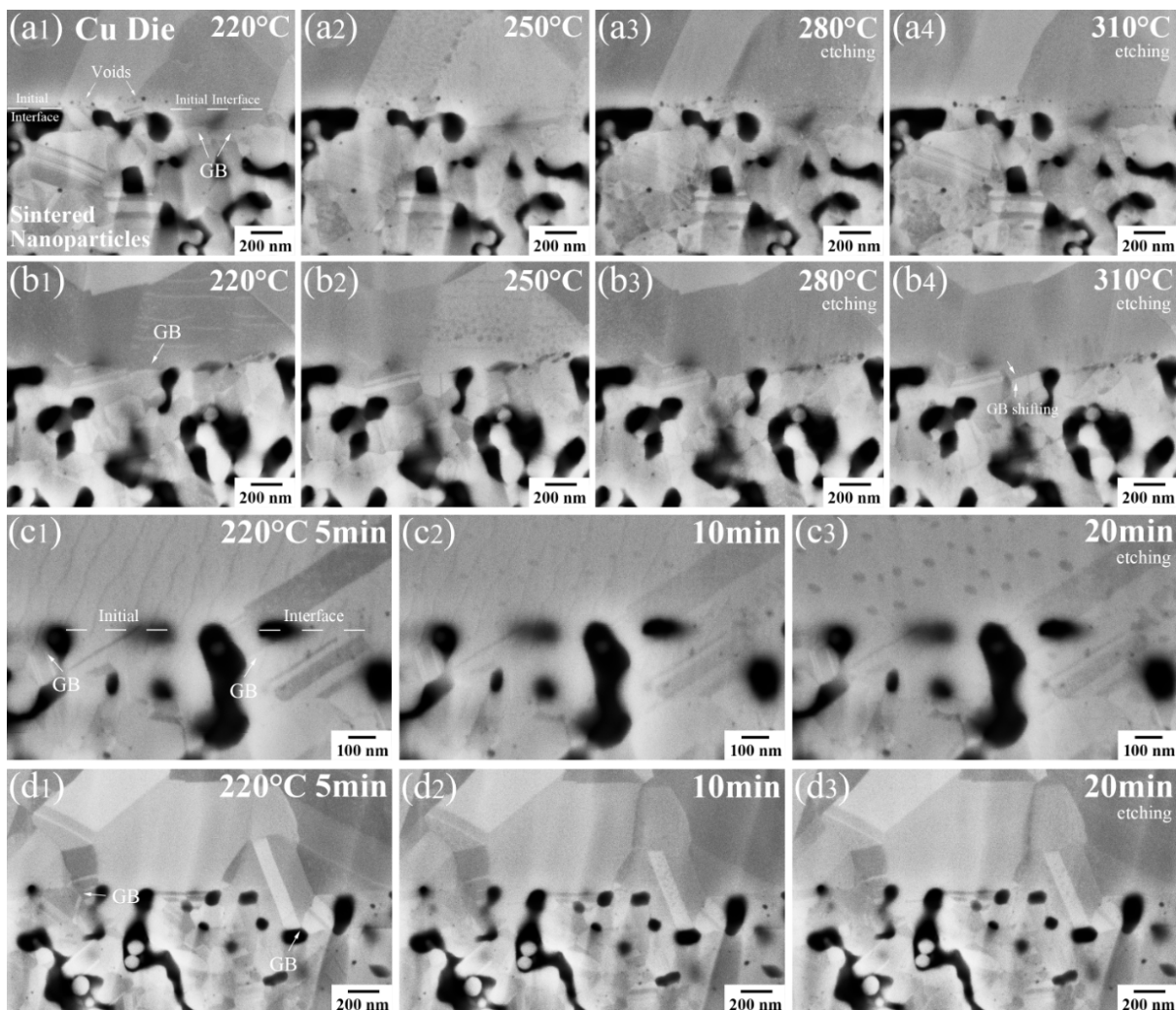


Figure 6. 8 Sequence of SEM observation showing the bonding interface at different temperature for 5min (a-b) and at 220 °C for different time (c-d). GB barely moves

after heating and only GB in (b1) moves a little. GBs in (a1, c1 and d1) move away from the initial interface towards the sintered Cu side during early sintering stage

Fig. 6. 9 (b) shows an obvious GB shifting process during temperature hold at 310 °C. It is clear that a Cu die twin grows by assimilating part of a neighboring sintered Cu twin and their GB moves towards sintered Cu side. Although the mean grain size shows little change during holding at 310 °C as discussed in Section 7.3.2, it can activate the GB shifting between larger Cu die grain and smaller sintered Cu grain. This kind of GB shifting can be also found during Cu nanoparticle sintering as shown in **Fig. 6. 5 (a)**, **Fig. 6. 6 (c-d)** and **Fig. 6. 7 (c)**. There are also some tiny voids along the initial interface due to incomplete sintering as shown in **Fig. 6. 9 (b1)**, the residual organics could also induce voids [78, 132]. Some new voids in **Fig. 6. 9 (b3)** exposed after the sample was slightly etched to make the grain structure visible. The cracks may originate from these defects (voids) during fracture and decrease the bonding strength.

However, after a drop test (from 1.5 meters height), the joint fracture exactly appears at the GB rather than the initial interface and the sintered Cu adhering to the Cu die also shows plastic deformation as shown in **Fig. 6. 9 (c)**. Kimura et al. [133] also reported that the fracture crack propagates along the GBs of sintered nanoparticle structure. Therefore, the joint strength can be further strengthened by the GB shifting away from the initial interface contains harmful voids. The GB shifting at the interface requires a high driving force due to the low surface activity of large Cu die grains and can be found in either the early sintering stage with the presence of high curvature nanoparticles or in the latter sintering stage with high temperature. This is responsible for the unchanged grain and pore size and porosity of sintered Cu structure but increasing joint strength at 310 °C with increasing time as mentioned in Section 7.3.2.

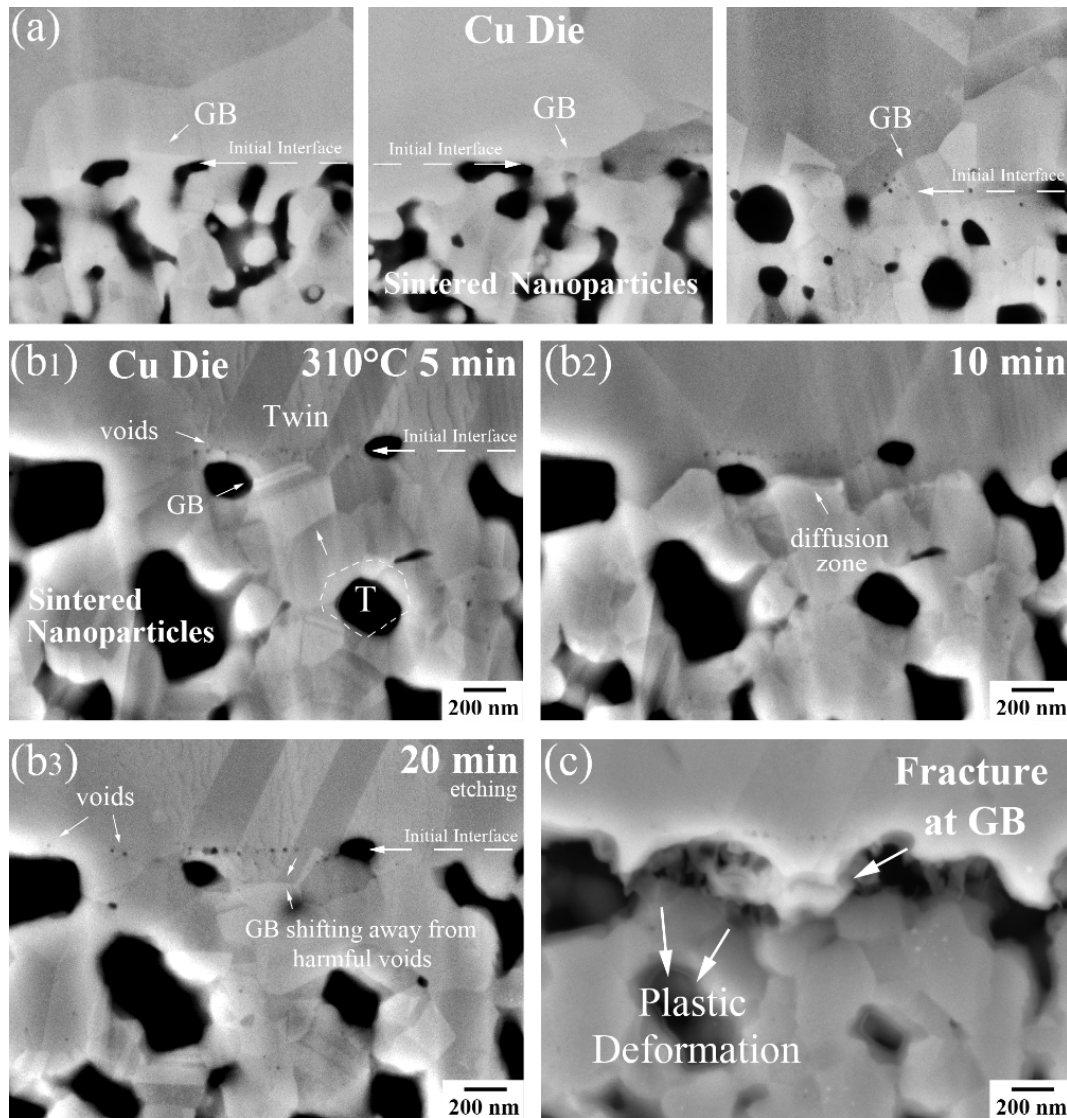


Figure 6.9 Representative SEM images (a) of the bonding interface showing GB moves towards Cu die side. Time sequences of SEM observation (b) showing the bonding interface at 310 °C, SEM fracture surface image (c) of corresponding joint after drop test. GB in (b1) moves away from voids after heating and fracture in (c) exactly appears at the GB not the initial bonding interface.

6.5 Conclusions

The grain growth behavior in the bulk sintered Cu structure was identified by quasi-in-situ SEM observation. Grains continue to grow at elevated temperature by merging with other similar-sized grains or assimilating the whole or parts of other smaller grains. Incomplete

orientation unification during coalescence may produce twinning and the twin grains can also assimilate nearby grains and transform their crystal structure into twins. Both the porosity of the sintered structure and the bonding interface decrease with either increasing temperature or time. The rate of decrease levels off when the porosity approaches the ultimate value of 11%. Decreasing porosity is accompanied by the decreasing pore size in case of insignificantly changed grain size or the decreasing pore number in case of increasing grain size. GB diffusion dominates during Cu nanoparticle sintering under 310 °C and the most important factor determining joint strength is porosity rather than grain or pore size. Joint fracture tends to occur in the bulk sintered Cu structure and also at the GB between the sintered Cu and the Cu die/substrate grains. The sintered Cu structure shows plastic deformation with dimple-like morphology after fracture. The assimilation of sintered grains by die/substrate grains results in the interfacial GB shifting away from the initial bonding interface, and away from the high concentration of voids at this interface, resulting in strengthening of the sintered Cu joint.

Chapter 7: Unraveling the complex oxidation effect in sintered Cu nanoparticle interconnects during high temperature aging

7.1 Background

Although considerable sintered Cu joint strength has been achieved in many studies, the reliability of Cu joint under high temperature is less widely reported. The main problem with Cu nanoparticle based materials is the ease of oxidation, which causes difficulty in Cu joining process and deterioration of joint reliability. In our previous research [134], the Cu oxide has been found to be a different brittle structure to the sintered Cu structure. The oxides formed during high temperature aging could weaken the strong Cu bonding and result in a degradation of joint strength, which is also reported by other papers [135, 136]. Meanwhile, some researchers believe that the oxidation can increase the density of sintered Cu structure and thus strengthen the joint [4, 137]. Gao et al. [137] found that during aging at 200 °C in air, the shear strength of sintered Cu joints increases significantly at first and then decreases with the aging time. Oxidation enhancement of strength is not able to explain subsequent strength degradation after prolonged the aging time. The complex effect of oxidation on the microstructure and strength of sintered Cu structure requires more in-depth research.

7.2 Objectives

This chapter aims to unravel the multiple oxidation effects on the microstructure and strength of sintered Cu structure. The microstructure evolution of sintered Cu structure during high temperature aging was investigated using a quasi-in-situ method combining SEM observation and ion beam etching. The effect of aging time on the grain size, porosity and strength of the sintered structure and the micro-fracture mechanism of the joint were also studied.

7.3 Methods

Cu nanoparticles and glycerol were mixed to fabricate the reducing paste. After the reduction and pre-bonding process in Chapter 5, the assemblies were heated to 220 °C for 20 min without

pressure in N₂. Next the joints were aged at 200 °C in air for 24 h, 100 h and 500 h to study the effect of oxidation on sintered Cu structure. The joint cross section structure was also sequentially aged for 1 h, 3 h, 10 h and 24 h to accelerate the oxidation while it was intermittently observed by combining SEM and ion beam miller during the aging process. The same joint was slightly etched by ion beam milling to adequately remove the oxide formed on Cu surface after every aging step so that the original sintered Cu structure could be clearly seen.

7.4 Results and discussion

7.4.1 Effect of aging time on microstructure

The joints bonded at 220 °C/20 min were aged at 200 °C in air for different times to investigate the effect of oxidation on the microstructure and strength of sintered Cu structure. The sintered Cu structure was found to be oxidized after aging at 200 °C in air and the color of the joint fracture surface also changed from the original orange to black and grey as shown in **Fig. 7. 1 (a)**. The main oxidation product of sintered Cu during high temperature aging has been reported to be Cu₂O in our previous research (220 °C) [134] and also by other papers (200 °C) [137, 138]. Meanwhile, it is found that around 55% of the fracture surface area in the aged joints, show a similar color to the original sintered Cu and a limited oxygen content (a slight increase from 0.4 % at 0 h to 0.6 % at 500 h) as shown in **Fig. 7. 1 (b)**.

With increasing the aging times, the oxidized area percentage including both black and grey area increases slightly which indicates that the oxidation did not propagate significantly with the aging time. The oxygen content of grey area changes little while the oxygen content of black areas increases from 10.5% at 24 h to 14.5% at 500 h. The shear strength of joints increases firstly with increasing aging time and reaches a peak of 32.0 MPa at 100 h, then decreases as aging time rises to 500 h. For the un-oxidized sintered Cu areas (orange color), the aging is indeed a re-sintering process. However, the grain size of the bulk sintered Cu in this area changes little with the aging times. The porosity also decreases slightly from 12.7%

at 0 h to 9.8 % at 100 h and then remains steady. The pore size decreases from 99.70 nm at 0 h to 79.68 nm at 500 h while the pore number in the unit area of $1 \mu\text{m}^2$ increases from 10.73 to 15.19. The pore size and eccentricity distributions show a slightly decreasing number of large and irregular pores with increasing aging time (see Figure A10 in Appendix). The statistical significance of these parameters is also analyzed by T-test and can be seen in Appendix. The insignificant decrease in porosity indicates that the microstructure change of the black and grey area during aging could be responsible for the changed joint strength and this will be discussed in Section 7.4.2.

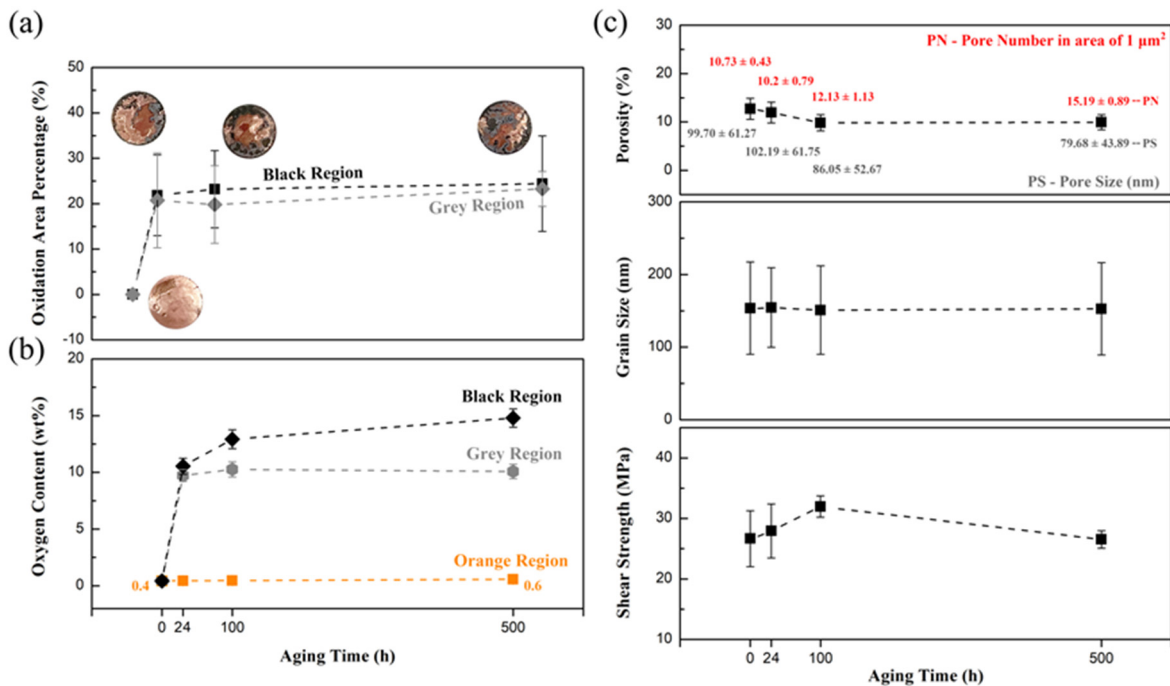


Figure 7. 1 Variation in oxidation area (a) of joint and corresponding oxygen content (b), porosity and grain size and pore size/number of bulk sintered Cu (c) and shear strength of joints (d) due to different aging times. (SEM cross section images of three replicates were used for measurement and shear tests were performed in five replicates)

7.4.2 Fracture mechanism of joint

The effect of oxidation on the microstructure and the micro-fracture mechanism of joint was investigated by comparing the fracture surfaces of the original joint and the aged joint for 100

h. Different areas of Cu substrate and their corresponding areas on Cu die were both observed as shown in **Fig. 7. 2**. It is clear that the Cu nanoparticles were not uniformly distributed in the sintered Cu structure and this results in areas with different densities termed the loose, intermediate (IM) and dense area. Aggregation of Cu nanoparticles could be one reason for the non-uniform distribution. Meanwhile, the reaction byproduct of gas will cause the formation of bubbles in the paste during the reduction process, which would worsen the distribution. The following sintering process was carried out without the assistance of pressure, so that those loose areas cannot be eliminated.

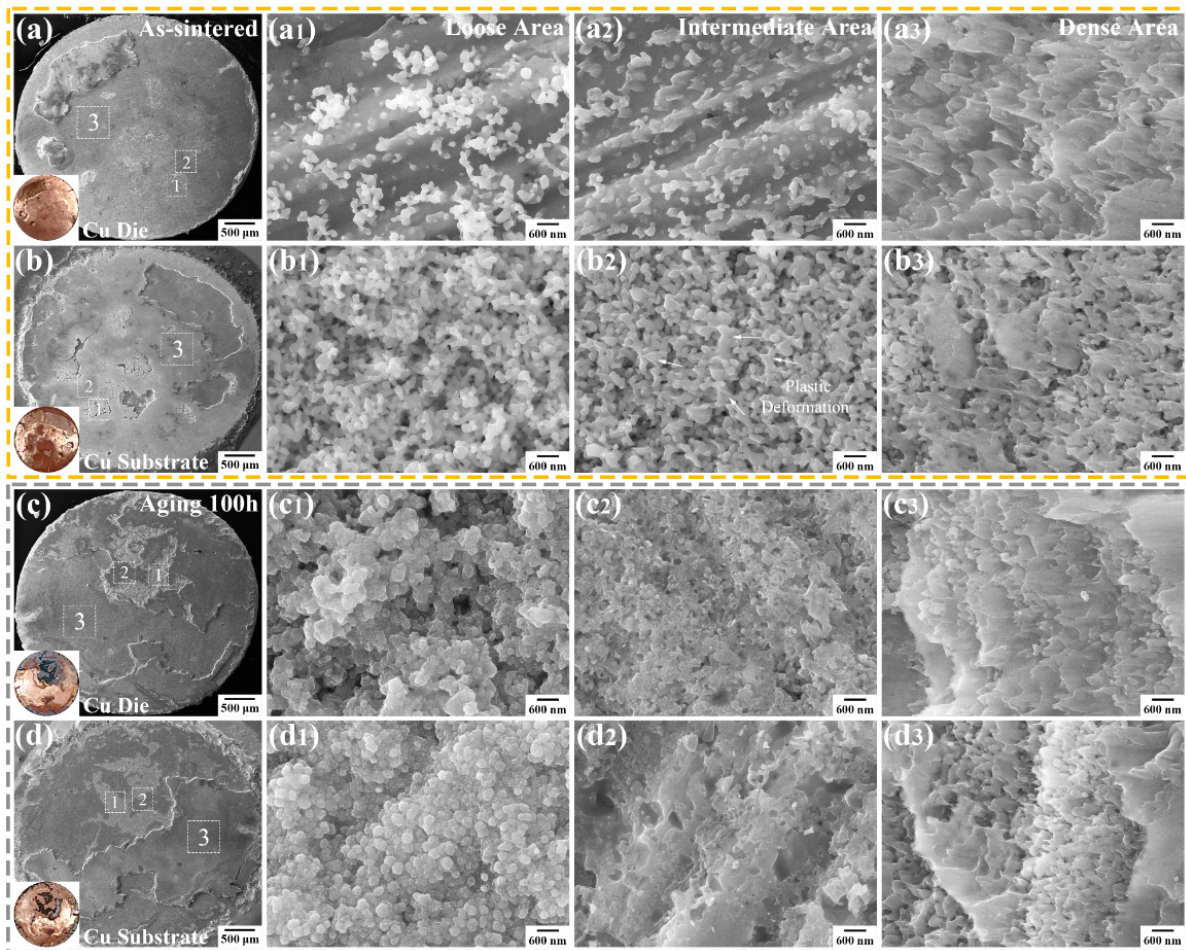


Figure 7. 2 SEM fracture surface images of joint before (a, b) and after (c, d) aging at 200 °C for 100 h

In the loose area, Cu nanoparticles were not contacted closely, which causes insufficient sintering of Cu as shown in **Fig. 7. 2 (b1)**. The sintered Cu nanoparticles in these areas show

little deformation after fracture and the joint fracture occurs mainly at the bonding interface between sintered Cu and Cu substrate as shown in **Fig. 7. 2 (a1)**. This highly porous structure facilitates the introduction of air during aging and this leads to significant oxidation (black color) of the sintered Cu structure. The oxidized structure also shows little deformation, while it becomes much denser and the joint fracture occurs within the bulk sintered Cu structure as shown in **Fig. 7. 2 (c1)** and **(d1)**. The sintered Cu structure in the IM area shows trace of plastic deformation as shown in **Fig. 7. 2 (b2)**, but the bonding between sintered Cu and Cu substrate is still bad and the Cu substrate surface is exposed after joint fracture. The sintered Cu structure in this area becomes a bit denser after aging, while the oxidized structure tends to be more brittle and shows a different color of grey to the structure of loose area as shown in **Fig. 7. 2 (c2)** and **(d2)**. In contrast, the fracture surfaces of dense area (orange color) in both the original and aged joints show significantly plastic deformation, which indicates that strong bonding was achieved. These dense areas contribute to the high joint strength of over 25 MPa for all aging conditions.

Fig. 7. 3 shows the SEM cross section images of the original and aged joints. It should be noted that the cracks in **Fig. 7. 3** were caused by the joint cross section process and one can easily distinguish Cu and its oxide due to their different contrasts in the BSE images as shown in **Fig. 7. 3 (d)**. The corresponding EDS mapping result in **Fig. 7. 3 (d1)** also confirms this. The porosity of loose sintered area is 26.3 % and Cu nanoparticles were poorly bonded and the sintered Cu fell apart after fracture as shown in **Fig. 7. 3 (a)**. However, the oxides formed during aging tend to fill into the voids and decrease the porosity to 10.9 % (100 h), which results in a much more compact structure as shown in **Fig. 7. 3 (e)**. Although the oxidized Cu structure shows a different brittle fracture to the dense and un-oxidized Cu structure as shown in **Fig. 7. 3 (b)** and **(d)**, the loose sintered Cu structure can still be strengthened by the decreasing porosity. Meanwhile, the bonding interface becomes almost voidless due to the oxidation as shown in

Fig. 7. 3 (f) and the fracture path changes from the interface into the bulk sintered Cu, which is consistent with the joint fracture results in **Fig. 7. 2 (a1-d1)** and **Fig. 7. 3 (c)**.

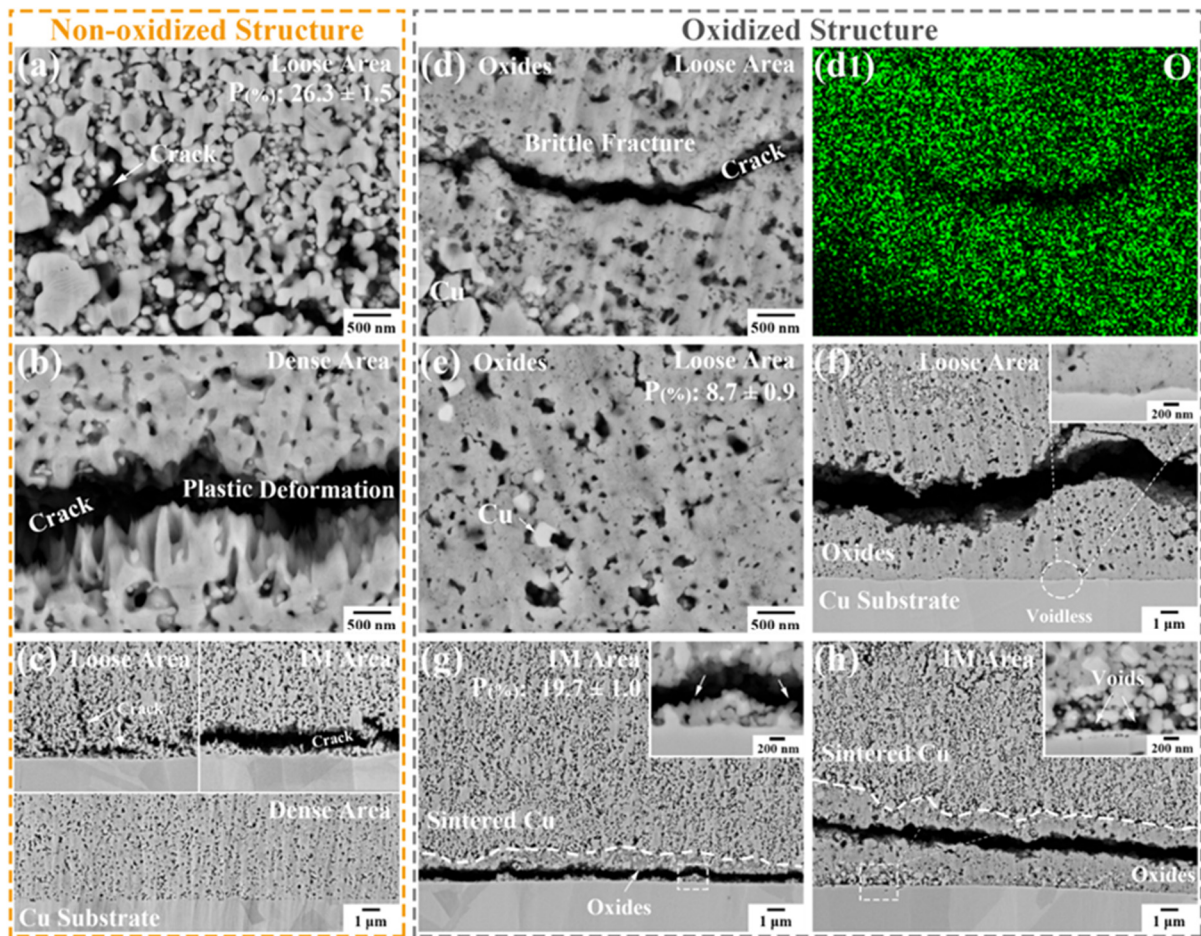


Figure 7. 3 Representative SEM cross section images of joint before (a-c) and after (d-h) aging. Corresponding EDS mapping result (d1) of image (d) and P in (a), (e) and (g) represents porosity

It is found that the oxides start to form in the interface area at first and then spread into the bulk sintered Cu structure as shown in **Fig. 7. 3 (g)** and **(h)**. The fracture path also moves from the interface into the bulk sintered Cu with the increasing oxidation area. Meanwhile, the mixed sintered Cu and oxide structure in the inset image of **Fig. 7. 3 (g)** also shows trace of plastic deformation after fracture. Unlike the full oxidation of sintered Cu in the loose area, the spread of oxide was suppressed by the lower porosity of 19.7 in the intermediate area as shown in **Fig. 7. 3 (g)** and limited to areas near the bonding interface. In conclusion, the joint was further

strengthened by the oxidation as it can significantly increase the density of both the bulk sintered Cu and the interface in the loose area and lead to a shift of fracture path from the interface to the bulk structure.

7.4.3 Particle coarsening mechanism

Fig. 7. 4 (a-c) show the morphology of aged Cu nanoparticles in the loose areas for different times. It is clear that the sintered Cu nanoparticles are covered by many smaller oxide nanoparticles and undergo an obvious coarsening process when the aging time increases from 100 h to 500 h, and a typical nanowire structure of CuO [97, 139] in the inset image of **Fig. 7. 4 (c)** also forms. However, the sintered Cu structure for all aging conditions show little deformation after fracture and the porosity decreases significantly at first and then remains consistent when the aging time rises to 100 h as shown in **Fig. 7. 4 (d)**. It can be deduced that the microstructure change of the IM and dense areas could be the possible reason of decreasing joint strength from 100 h to 500 h. From **Fig. 7. 2 (a2-d2)** and **Fig. 7. 3 (c, g, h)**, it seems that the oxidation tends to increase the sintering density of IM areas while it also turns the partly deformable Cu matrix into a brittle structure. Different IM sintered areas of Cu die and their corresponding areas on Cu substrate were both observed as shown in **Fig. 7. 4 (e-h)**. The magnified views of single micro-sized compact aged for 100 h in **Fig. 7. 4 (e1)** and **(f2)** show signs of plastic deformation after fracture. However, the sintered Cu becomes a completely brittle structure and shows little deformation after aging for 500 h as shown in **Fig. 7. 4 (g1-2)** and **(h1-2)**. Meanwhile, it is found that the sintered structure surface is covered by many more oxide nanoparticles compared to the structure aged for 100 h.

Based on the SEM observation, a possible coarsening mechanism of sintered Cu structure during high temperature aging is proposed. First, the Cu nanoparticles coalesce together during sintering and form a porous structure with separated clumps (termed compacts) with necks and voids as shown in **Fig. 7. 5 (a)**. During high temperature aging, the oxide nanoparticles grow

on the surface and also in the interspace of sintered Cu structure by consuming Cu in the core and neck areas. These oxide nanoparticles are poorly bonded and are intrinsically a brittle structure. Meanwhile, the sintering neck areas are thinner than the inner bulk Cu areas and tend to be the weak point of the whole sintered Cu structure. After short time aging, the remaining un-oxidized Cu bonding areas are still plastically deformable as shown in Fig. 7. 5 (b1). However, when the oxides grow further and consume the whole Cu structure in the neck area, the oxidized Cu becomes a completely brittle structure as shown in Fig. 7. 5 (c1). The fracture would then occur within the oxide and result in a coarsening behavior of sintered Cu nanoparticles.

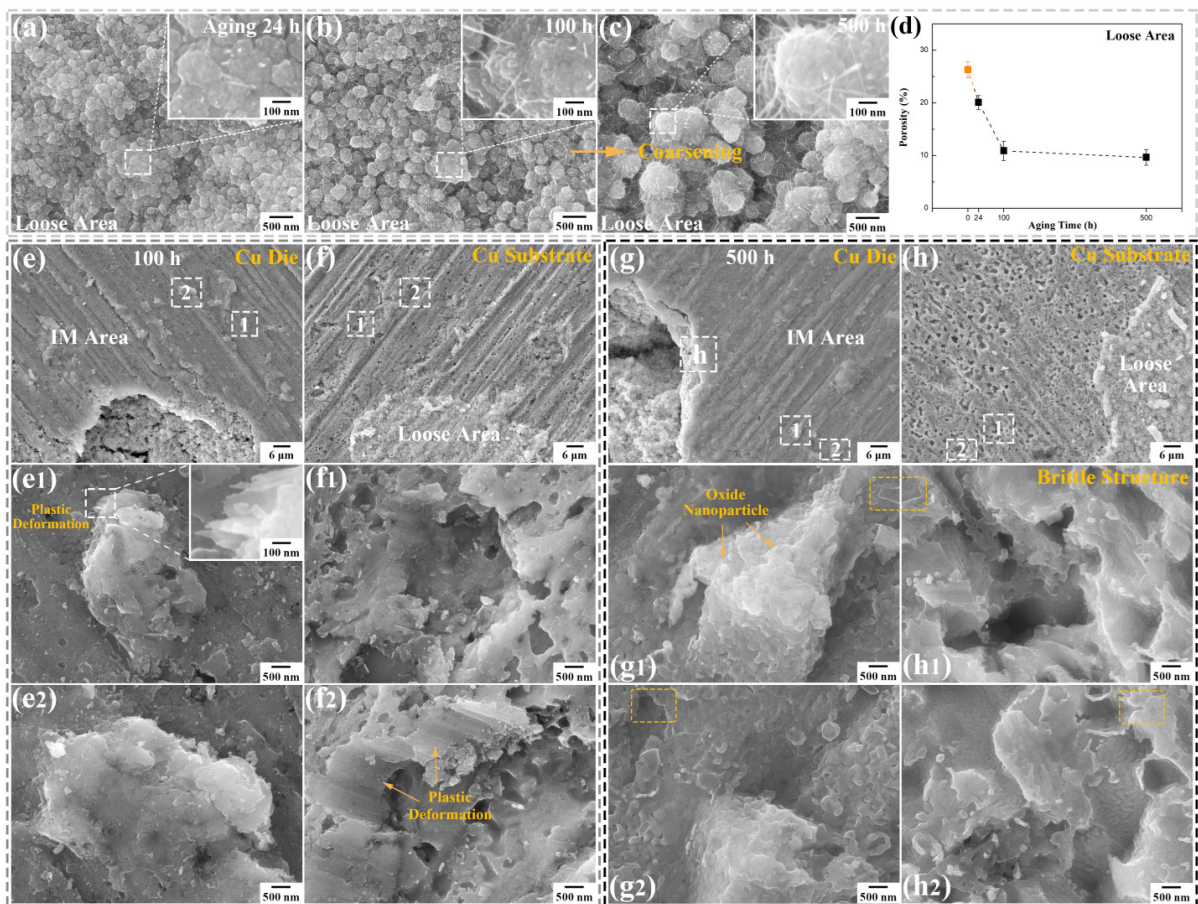


Figure 7. 4 SEM fracture surface images (a-c) and porosity (d) of loose sintered areas for different aging times. SEM fracture surface images of joint aged for 100 h (e-f) and 500 h (g-h). Areas on Cu die: (e-e2) and (g-g2), corresponding areas on Cu substrate: (f-f2) and (h-h2)

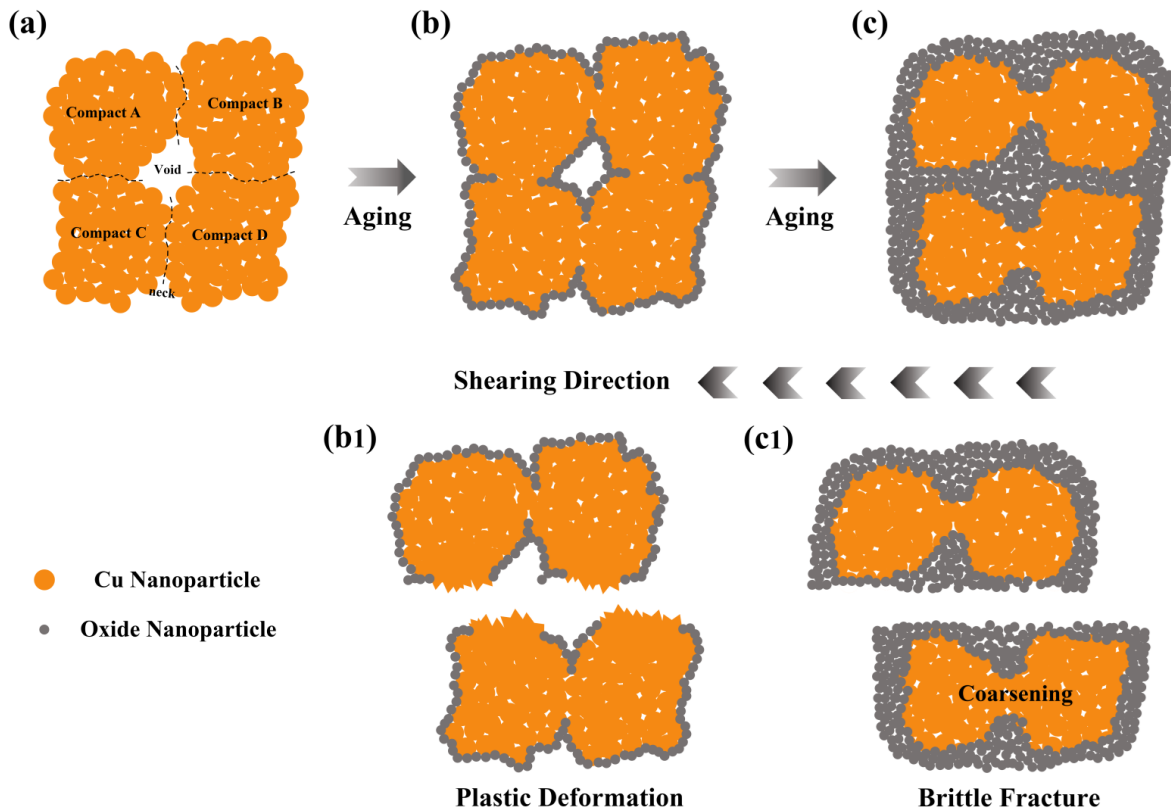


Figure 7. 5 Schematic illustration of the coarsening process of sintered Cu structure

7.4.4 Void growth during aging

From the fracture surface of joints aged for 100 h in **Fig. 7. 2 (b2)**, it can be seen that the strong and deformable Cu bonding in the IM areas is limited. Therefore, the correlation between the transition from a deformable structure at 100 h into a brittle structure at 500 h and the decreasing joint strength is not completely convincing. In order to investigate the effect of aging on the microstructure of dense sintered Cu, the joint cross section (dense area) was directly aged at 200 °C in air to investigate the dominant effect of oxidation and the oxide was removed adequately by ion beam milling after every aging step so that the original sintered Cu structure could be clearly seen. It is clear that the voids ranging from 10-30 nm diameter start to form in the sintered Cu structure after aging for 3 h as shown in **Fig. 7. 6 (a3)**. These voids are much smaller than the voids caused by incomplete sintering and can be easily distinguished.

Meanwhile, it is found that the oxides tend to form in the interspace of sintered Cu and decrease the porosity as shown in **Fig. 7. 6 (b)**, which is consistent to the porosity result in **Fig. 7. 4 (d)**.

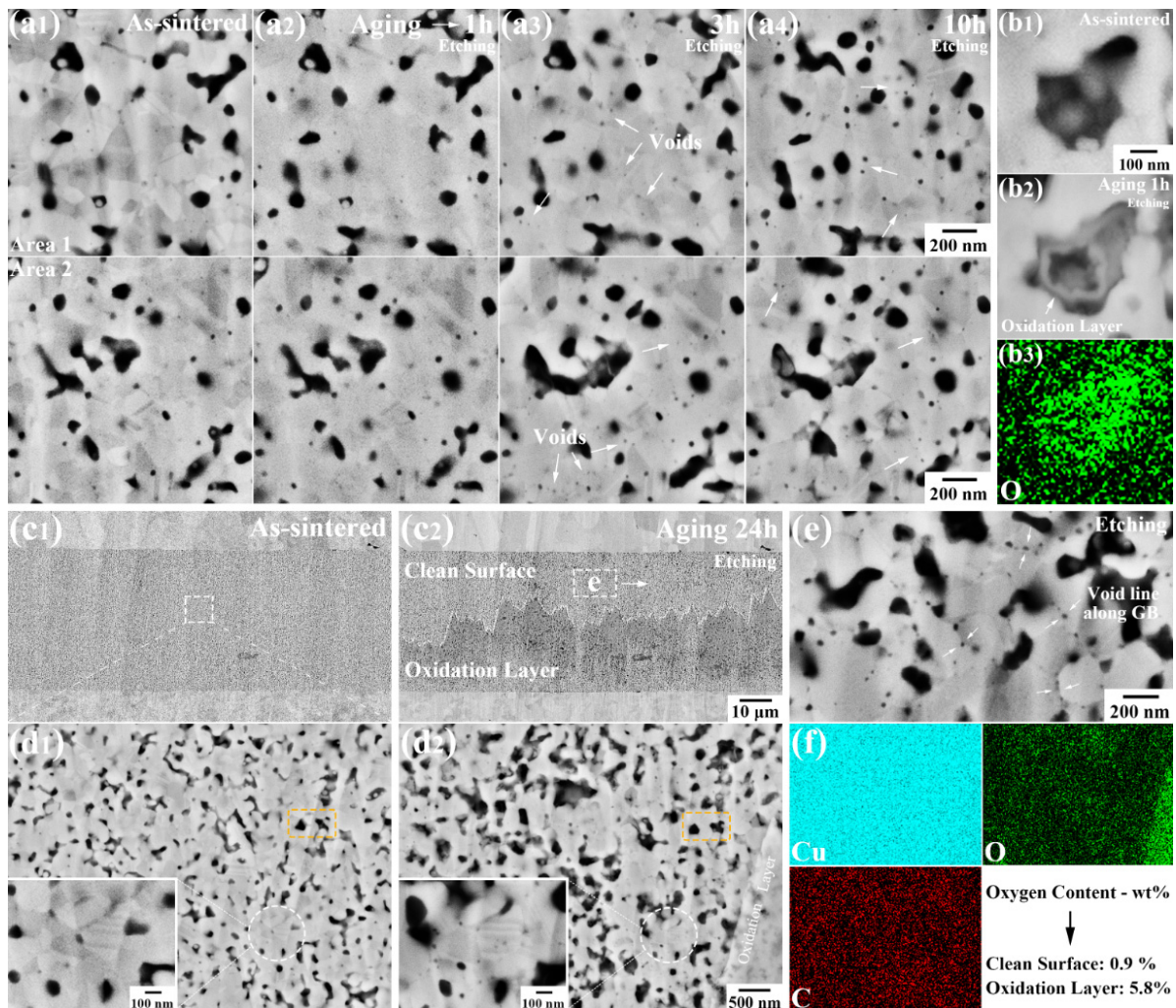


Figure 7. 6 Time sequences of SEM observation showing the formation of void (a, c, d) and oxide (b) in sintered Cu structure during aging. Representative SEM image of joint cross section showing the void line (e) along the GBs after aging for 24 h. Corresponding EDS mapping (b3) and (f) of image (b1) and (d2), respectively

Although the joint cross section structure shows void formation after aging for 3 h and 10 h, the preferential nucleating sites for oxide formation remains unclear. Therefore, the joint cross section (dense area) was also aged for 24 h to produce more voids. From **Fig. 7. 6 (d1)** and **(d2)**, it is clear that the voids occur mainly at the GBs and also inside the sintered Cu

nanoparticles. Meanwhile, a large number of voids distributing in a line along the GBs were found in the aged structure as shown in **Fig. 7. 6 (e)**. More SEM images of the joint cross section structure before and after aging are shown in **Fig. 7. 7 (a-c)**. In contrast, the joint cross section without aging was also etched and there are not many new voids formed after etching as shown in **Fig. 7. 8 (a)**, which indicates that these tiny voids in **Fig. 7. 6** and **Fig. 7. 7** are caused by the oxidation. It has been also reported that the GBs are the preferential nucleating sites for oxide formation and the oxide islands formed along the GBs show a faster growth rate than that on the Cu surface [102].

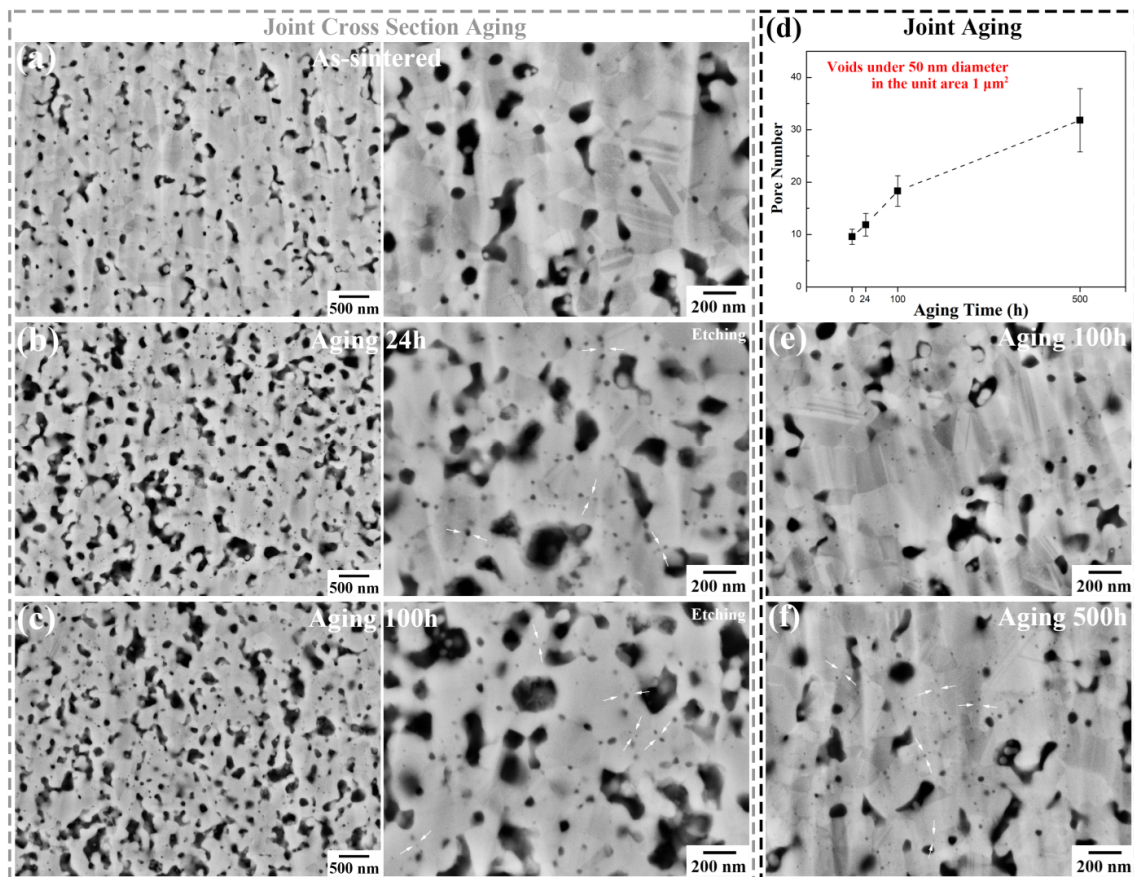


Figure 7. 7 SEM images of joint cross section before (a) and after aging for 24 h (b) and 100 h (c). Variation in pore number (d) of sintered Cu due to different aging times and representative SEM cross section images of joint after aging for 100 h (e) and 500 h (f)

In the case of the whole joint aging, the oxidation in the dense area was significantly suppressed by the low porosity of ~10 %. A large number of oxidation voids only occur after

aging for 500 h and the number of voids under 50 nm diameter in an unit area $1 \mu\text{m}^2$ increases from 9.6 at 0 h to 31.8 at 500 h as shown in **Fig. 7. 7 (d)**. GB is the interface between the particles with misaligned orientations and could be the weak point of the Cu bonding [140]. Kimura et al. [133] also found that the fracture cracks propagate along the GBs of sintered nanoparticle structure. Therefore, it can be inferred that the formation of voids along the GBs tend to weaken the bonding of sintered Cu nanoparticles and result in a decrease of joint strength after aging for 500 h.

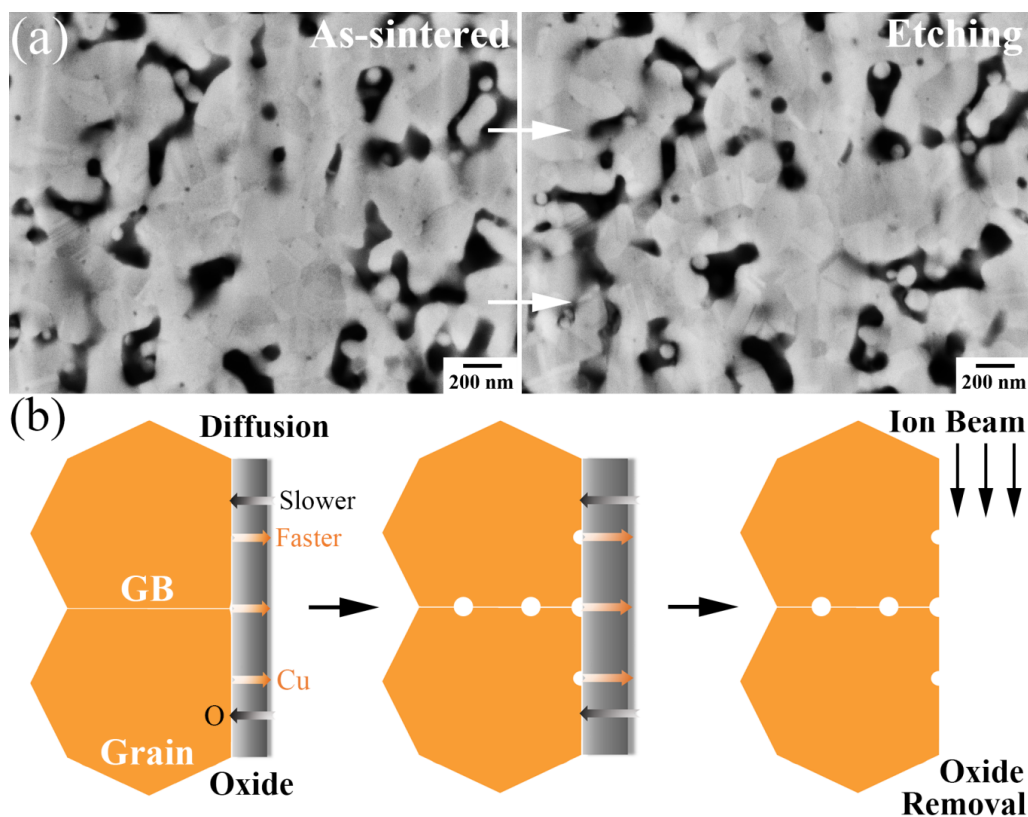


Figure 7. 8 Representative BSE cross section image (a) of sintered Cu before and after etching. Schematic illustration (b) of the Kirkendall void formation

This oxidation void formation can be explained by the Kirkendall effect [141, 142]. The sequence of oxidation reactions on a clean Cu particle surface is generally accepted to be oxygen chemisorption, nucleation and growth of surface oxide, and bulk oxide growth. The oxygen atoms first diffuse on the particle surface and would be incorporated into an oxide

island. These oxide islands nucleate and grow on the Cu surface until they coalesce into a homogeneous oxide layer separated from the Cu core by a nanoscale vacancy gap as shown in **Fig. 7. 6 (b2)** [99, 143]. This oxide layer then grows and prevents exposure of Cu to oxygen. Further oxidation of Cu occurs on both internal and external surfaces of the oxide layer and is a result of Cu atoms from the underlying Cu core diffusing outward through the oxide layer and oxygen atoms diffusing into Cu core. The higher diffusion rate of Cu atoms through the oxide layer compared to oxygen atoms will lead to the nucleation of small vacancies, which then accumulate to form nanoscale voids along the GBs and also inside the sintered Cu nanoparticles as shown schematically in **Fig. 7. 8 (b)**. The velocity of any given plane related to the flux of vacancies crossing it can be given by the Darken equation [14]:

$$v = (D_A - D_B) \frac{\partial C_A}{\partial x} \quad (17)$$

where D_A is the diffusion coefficient of Cu atoms and $\frac{\partial C_A}{\partial x}$ is the concentration gradient, D_B is the diffusion coefficient of oxygen atoms.

The formation of Kirkendall void in single Cu nanoparticle has been widely reported in synthesizing hollow oxide nanoparticles for sensor technologies and nanomedicine by means of in situ plasmonic nanospectroscopy [144, 145] and scanning transmission electron microscopy [138]. When holding at 200 °C in the presence of oxygen, the Kirkendall void is found to nucleate at the vacancy gap interface and then expand into the metal core. This expansion undergoes a transition from linear to angular void growth mode until the entire Cu particle is consumed. Unlike the single Cu nanoparticle oxidation, where the nanoparticle becomes a complete hollow oxide structure within several minutes. The Cu oxidation in the dense sintered Cu area was significantly suppressed by the low porosity, and the formation of Kirkendall voids was limited to a very early stage. Kirkendall voids, though a typical defect in solder joints, have rarely been reported in the context of sintered Cu interconnects. This study constitutes the first detailed experimental observation of nanoscale Kirkendall void formation

in the bulk sintered Cu during high temperature aging. This finding provides novel insights for understanding of the oxidation effect on the microstructure and strength of sintered Cu.

7.5 Conclusions

The complex oxidation effect on the porosity and grain size and strength of sintered Cu structure was revealed. The Cu oxides formed during aging tend to fill into the interspace of the poorly bonded Cu nanoparticles in the loose area and significantly decrease the porosity of sintered Cu from 26.3 % to 10.9 %, and the bonding interface of sintered Cu structure and Cu substrate becomes almost voidless. Thus, the joint fracture path shifts from the interface into the bulk sintered structure and the joint strength increases from 26.7 MPa at 0 h to 32.0 MPa at 100 h. However, the further growth of brittle oxide in the intermediate areas accompanied by a particle coarsening behavior would turn the plastically deformable Cu matrix into a brittle structure. Although the oxidation was significantly limited by the low porosity (near 10%) of dense area, the 200 °C aging (re-sintering) fails to further increase the density of sintered Cu and the grain size also changes little. Meanwhile, a large number of nanoscale Kirkendall voids are found to form mainly along the GBs and also inside the sintered Cu nanoparticles after a prolonged aging of 500 h. These voids induced by the different diffusion rate of Cu and oxygen atoms through the thin oxide layer, will weaken the Cu bonding and result in a decreasing joint strength of 26.5 MPa at 500 h. The similar original and 500 h aged joint strength indicates that the sintered Cu nanoparticle interconnection have a good thermal reliability and is a promising candidate to replace the current lead-free solders for high power electronics.

Chapter 8: Conclusions

8.1 In situ reduction-sintering

Chapter 4 and 5 present the in situ reduction-sintering process of both CuO and Cu nanoparticles by glycerol for fabricating strong Cu-Cu bonding for power electronics. The original oxide is reduced to Cu during the reduction process and the remaining organics further prevent the oxide formation during the pre-bonding process. The reduced Cu particles can be immediately sintered after the reduction and pre-bonding processes at the same temperature and the rapid sintering speed significantly depresses the formation of oxide during the subsequent sintering. The proposed method produces high sintered Cu joint strength (22 MPa of CuO for 15 min sintering and 33 MPa of Cu for 5 min sintering), but without the need for pressurized sintering or protective gas atmospheres.

The reduced Cu particle size resulting from CuO is very large (1 μm). These micron-sized particles have a better oxidation resistance than nanoparticles and oxide is only found to form after sintering for 15 min. The only oxide that forms after a longer sintering duration is Cu_2O , which shows morphological evolution from a laminar layer structure formed by growth and coalescence of Cu_2O nano-strips to a multiple layer structure formed by crossed and overlapping Cu_2O nano-grains. In contrast, the high surface activity of Cu nanoparticles results in a more sufficient sintering of Cu and also a faster oxidation speed. Therefore, the Cu nanoparticles were sintered for only 5 min to form the joint. The shape of the oxide grains is also found to change from spherical (Cu_2O) to rod (CuO) shaped during storage in air. Cu nanoparticles seem to be more promising than CuO nanoparticles as the interconnection material due to the stronger and deformable sintering structure. Meanwhile, the in situ reduction-sintering process eliminates the use of special storing condition for Cu nanoparticle, which comprises the merit of CuO (free of further oxidation).

8.1.1 Future work suggested from chapter 4 and 5 results

The use of pressure in pre-bonding or bonding process seems to be inevitable as it can significantly increase the sintering density and the thermal reliability of sintered Cu joint. The manufacturing cost can be further decreased by selecting cheaper materials. Cu nanoparticles under 50 nm diameter have high surface activity and sinterability. However, these ultra-small nanoparticles are difficult to synthesize and store. Cu submicro/microparticle and CuO nano/microparticle are good alternatives. For Cu submicro/microparticle, special surface modification (i.e. Ag or Sn cover) for increasing the sinterability are not the optimal solution due to the high cost. Cu submicro/microparticle can be slightly oxidized to create a thin oxidation film on the surface, and then using a specific reducing agent to reduce the oxide to nano-Cu. Reduction-sintering of CuO would be also promising if the reduced Cu size can reach the nanoscale. Therefore, future work in the field should focus on developing effective reduction-sintering process for Cu submicro/microparticle and CuO nano/microparticle.

8.2 Grain growth mechanism during sintering

Chapter 6 develops a specific quasi-in-situ method combining SEM observation and ion beam etching to investigate the mechanism of grain growth in the sintered Cu structure during sintering. The cross section of sintered Cu structure has to be slightly etched by ion beam miller after every heating step so that the GB could be clearly seen. The effect of sintering conditions on grain and pore size, porosity and strength of the sintered Cu structure was also studied. The grains are found to continuously grow accompanied by orientation unification which is attributed to grain boundary (GB) migration or dislocation motion at elevated temperature. Incomplete orientation unification during coalescence may produce twinning and the twin grains can also assimilate nearby grains and transform their crystal structure into twins. Decreasing porosity of sintered Cu structure during increasing sintering temperature or time is accompanied by the decreasing pore size in case of insignificantly changed grain size or the

decreasing pore number in case of increasing grain size. GB diffusion dominates during Cu nanoparticle sintering under 310 °C and the most important factor determining joint strength is porosity rather than grain or pore size. The assimilation of sintered grains by die/substrate grains results in the interfacial GB shifting away from the initial bonding interface, and away from the high concentration of voids at this interface, resulting in strengthening of the sintered Cu joint. This novel mechanism of GB shifting could provide new guidance for strengthening the sintered Cu interconnections for power electronics.

8.2.1 Future work suggested from chapter 6 results

The atomic scale mechanism of coherent twin boundary formation and the shifting of GB between sintered Cu grains and substrate grains still remain unclear. An in situ high resolution TEM observation could be useful to reveal the relevant mechanism. Meanwhile, the grain orientation is not visible in the SEM observation and the use of electron backscattered diffraction (EBSD) could be helpful for further elaboration of the mechanisms of grain growth and twin formation. Introduction of coherent nano-twins into sintered Cu structure can increase the joint strength, but the relevant research is currently limited. Therefore, future work should focus on atomic scale research of grain growth and twin formation and developing effective method to introduce coherent twin structure in sintered Cu joint.

8.3 Oxidation effect on microstructure of sintering Cu structure

The complex oxidation effects on the porosity and grain size and strength of sintered Cu structure during high temperature aging have been unraveled in Chapter 7 and conflicting findings in the literature reconciled. The Cu oxides formed during aging tend to fill into the interspace of the poorly bonded Cu nanoparticles in the loose area and initially increase both the density and strength of sintered Cu overall. However, the further growth of brittle oxide in the intermediate areas accompanied by particle coarsening behavior would turn the plastically deformable Cu matrix into a brittle structure. Meanwhile, a large number of nanoscale

Kirkendall voids are found to form mainly along the GBs and also inside the dense sintered Cu nanoparticles after a prolonged aging of 500 h. These voids induced by the different diffusion rate of Cu and oxygen atoms through the thin oxide layer, will weaken the Cu bonding and result in a decreasing joint strength at 500 h. The similar original and 500 h aged joint strength indicates that the sintered Cu nanoparticle interconnection have a good thermal reliability and is a promising candidate to replace the current lead-free solders for high power electronics.

8.3.1 Future work suggested from chapter 7 results

More tests related to the joint reliability need to be done (i.e. thermal cycle and shock). While, the conductivities of sintered Cu film were mostly measured and reported, the conductivities of the whole sandwich structure and the reliability of the sintered Cu interconnection in power devices have been less widely reported. Therefore, future work should focus on these topics.

Reference

- [1] F. Iacopi, M. Van Hove, M. Charles, K. Endo, Power electronics with wide bandgap materials: Toward greener, more efficient technologies, *MRS Bulletin* 40(5) (2015) 390-395.
- [2] X. Guo, Q. Xun, Z. Li, S. Du, Silicon Carbide Converters and MEMS Devices for High-temperature Power Electronics: A Critical Review, *Micromachines* 10(6) (2019) 406.
- [3] B. Ozpineci, L.M. Tolbert, Comparison of wide-bandgap semiconductors for power electronics applications, United States. Department of Energy 2004.
- [4] T.F. Chen, K.S. Siow, Comparing the mechanical and thermal-electrical properties of sintered copper (Cu) and sintered silver (Ag) joints, *Journal of Alloys and Compounds* 866 (2021).
- [5] V. Vasudevan, T. Schulz, M. Pei, F. Toth, A.E. Lucero, B. Zhou, S. Mukherjee, The state of Pb-free solder — A joint reliability overview, 2016 IEEE International Reliability Physics Symposium (IRPS), 2016, pp. 6B-6-1-6B-6-6.
- [6] G. Zeng, S. McDonald, K. Nogita, Development of high-temperature solders: Review, *Microelectronics Reliability* 52(7) (2012) 1306-1322.
- [7] N. Saud, R.M. Said, Transient liquid phase bonding for solder—a short review, *IOP Conference Series Materials Science and Engineering (Online)* 701(1) (2019) 7.
- [8] H. Jiang, S. Robertson, S. Liang, Z. Zhou, L. Zhao, C. Liu, Rapid formation of intermetallic joint using Cu-Sn nanocomposite interlayer based on patterned copper nanowire array, *Materials Letters* 307 (2022) 131074.
- [9] S. Liang, A. Kunwar, C. Liu, H. Jiang, Z. Zhou, Preferential growth of intermetallics under temperature gradient at Cu–Sn interface during transient liquid phase bonding: insights from phase field simulation, *Journal of Materials Research and Technology* 19 (2022) 345-353.

- [10] H.S. Chin, K.Y. Cheong, A.B. Ismail, A Review on Die Attach Materials for SiC-Based High-Temperature Power Devices, *Metallurgical and Materials Transactions B* 41(4) (2010) 824-832.
- [11] L. Liu, Z. Chen, C. Liu, Y. Wu, B. An, Micro-mechanical and fracture characteristics of Cu₆Sn₅ and Cu₃Sn intermetallic compounds under micro-cantilever bending, *Intermetallics* 76 (2016) 10-17.
- [12] J. Feng, C. Hang, Y. Tian, B. Liu, C. Wang, Growth kinetics of Cu₆Sn₅ intermetallic compound in Cu-liquid Sn interfacial reaction enhanced by electric current, *Scientific Reports* 8(1) (2018) 1775.
- [13] D.H. Jung, A. Sharma, M. Mayer, J.P. Jung, A Review on Recent Advances in Transient Liquid Phase (TLP) Bonding for Thermoelectric Power Module, *REVIEWS ON ADVANCED MATERIALS SCIENCE* 53(2) (2018) 147-160.
- [14] D. Kim, J.-h. Chang, J. Park, J.J. Pak, Formation and behavior of Kirkendall voids within intermetallic layers of solder joints, *Journal of Materials Science: Materials in Electronics* 22(7) (2011) 703-716.
- [15] K. Zeng, R. Stierman, T.-C. Chiu, D. Edwards, K. Ano, K.N. Tu, Kirkendall void formation in eutectic SnPb solder joints on bare Cu and its effect on joint reliability, *Journal of Applied Physics* 97(2) (2005).
- [16] C. Chen, C. Choe, D. Kim, Z. Zhang, X. Long, Z. Zhou, F. Wu, K. Suganuma, Effect of oxygen on microstructural coarsening behaviors and mechanical properties of Ag sinter paste during high-temperature storage from macro to micro, *Journal of Alloys and Compounds* 834 (2020) 155173.
- [17] J.W. Yoon, J.H. Back, Effect of Sintering Conditions on the Mechanical Strength of Cu-Sintered Joints for High-Power Applications, *Materials (Basel)* 11(11) (2018).

- [18] L.M.C. C. Schwarzer, M. Schnepf, T. Stoll, J. Franke, M. Kaloudis, U. Aschaffenburg, Investigation of copper sinter material for die attach, Proceedings of SMTA International (2018).
- [19] X. Liu, H. Nishikawa, Pressureless sintering bonding using hybrid microscale Cu particle paste on ENIG, pure Cu and pre-oxidized Cu substrate by an oxidation–reduction process, Journal of Materials Science: Materials in Electronics 28(7) (2017) 5554-5561.
- [20] T. Yamakawa, T. Takemoto, M. Shimoda, H. Nishikawa, K. Shiokawa, N. Terada, Influence of Joining Conditions on Bonding Strength of Joints: Efficacy of Low-Temperature Bonding Using Cu Nanoparticle Paste, Journal of Electronic Materials 42(6) (2013) 1260-1267.
- [21] H. Nishikawa, T. Hirano, T. Takemoto, N. Terada, Effects of Joining Conditions on Joint Strength of Cu/Cu Joint Using Cu Nanoparticle Paste, The Open Surface Science Journal 3(1) (2010) 60-64.
- [22] Y. Mou, Y. Peng, Y. Zhang, H. Cheng, M. Chen, Cu-Cu bonding enhancement at low temperature by using carboxylic acid surface-modified Cu nanoparticles, Materials Letters 227 (2018) 179-183.
- [23] J.J. Li, C.L. Cheng, T.L. Shi, J.H. Fan, X. Yu, S.Y. Cheng, G.L. Liao, Z.R. Tang, Surface effect induced Cu-Cu bonding by Cu nanosolder paste, Materials Letters 184 (2016) 193-196.
- [24] J. Liu, H. Chen, H. Ji, M. Li, Highly Conductive Cu-Cu Joint Formation by Low-Temperature Sintering of Formic Acid-Treated Cu Nanoparticles, ACS Appl Mater Interfaces 8(48) (2016) 33289-33298.
- [25] X. Liu, H. Nishikawa, Low-pressure Cu-Cu bonding using in-situ surface-modified microscale Cu particles for power device packaging, Scripta Materialia 120 (2016) 80-84.
- [26] J.C. Roberts, M.K. Rahim, J.C. Suhling, R.C. Jaeger, P. Lall, Z. Ron, J. Jones, Stress measurements in large area array flip chip microprocessor chips, 2008 58th Electronic Components and Technology Conference, 2008, pp. 1462-1471.

- [27] C. Van Nguyen, S.K. Sistla, S. Van Kempen, N.A. Giang, A. Bezold, C. Broeckmann, F. Lange, A comparative study of different sintering models for Al₂O₃, Journal of the Ceramic Society of Japan 124(4) (2016) 301-312.
- [28] M.A. Asoro, Coalescence and sintering in metallic nanoparticles : in-situ transmission electron microscopy (TEM) study, (2012).
- [29] C.B. Carter, M.G. Norton, Ceramic Materials: Science and Engineering, Springer New York 2013.
- [30] J.E. Blendell, W. Rheinheimer, Solid-State Sintering, in: M. Pomeroy (Ed.), Encyclopedia of Materials: Technical Ceramics and Glasses, Elsevier, Oxford, 2021, pp. 249-257.
- [31] R.J. Brook, Sintering: An Overview, in: R.J. Brook (Ed.), Concise Encyclopedia of Advanced Ceramic Materials, Pergamon, Oxford, 1991, pp. 438-440.
- [32] M.N. Rahaman, 2 - Kinetics and mechanisms of densification, in: Z.Z. Fang (Ed.), Sintering of Advanced Materials, Woodhead Publishing 2010, pp. 33-64.
- [33] P.R. Couchman, W.A. Jesser, Thermodynamic theory of size dependence of melting temperature in metals, Nature 269(5628) (1977) 481-483.
- [34] W. Rao, The effect of size on the melting point Cu and Ni nanoparticles, Shanghai University, 2006.
- [35] A.S. Zuruzi, K.S. Siow, Electrical conductivity of porous silver made from sintered nanoparticles, Electronic Materials Letters 11(2) (2015) 308-314.
- [36] J. Li, C.M. Johnson, C. Buttay, W. Sabbah, S. Azzopardi, Bonding strength of multiple SiC die attachment prepared by sintering of Ag nanoparticles, Journal of Materials Processing Technology 215 (2015) 299-308.
- [37] C. Chen, K. Suganuma, Microstructure and mechanical properties of sintered Ag particles with flake and spherical shape from nano to micro size, Materials & Design 162 (2019) 311-321.

- [38] B. Cheng, A.H.W. Ngan, The sintering and densification behaviour of many copper nanoparticles: A molecular dynamics study, *Computational Materials Science* 74 (2013) 1-11.
- [39] W. Wang, G. Zou, Q. Jia, H. Zhang, B. Feng, Z. Deng, L. Liu, Mechanical properties and microstructure of low temperature sintered joints using organic-free silver nanostructured film for die attachment of SiC power electronics, *Materials Science and Engineering: A* 793 (2020) 139894.
- [40] J. Li, Q. Liang, C. Chen, T. Shi, G. Liao, Z. Tang, Cu-Cu Bonding by Low-Temperature Sintering of Self-Healable Cu Nanoparticles, 2019 IEEE 69th Electronic Components and Technology Conference (ECTC), 2019, pp. 661-666.
- [41] J. Liu, H. Ji, S. Wang, M. Li, The low temperature exothermic sintering of formic acid treated Cu nanoparticles for conductive ink, *Journal of Materials Science: Materials in Electronics* 27(12) (2016) 13280-13287.
- [42] Y. Yuan, H. Wu, J. Li, P. Zhu, R. Sun, Cu-Cu joint formation by low-temperature sintering of self-reducible Cu nanoparticle paste under ambient condition, *Applied Surface Science* 570 (2021).
- [43] X. Wang, Z. Zhang, Y. Feng, F. Xiao, Anti-oxidative copper nanoparticle paste for Cu–Cu bonding at low temperature in air, *Journal of Materials Science: Materials in Electronics* (2021).
- [44] Y. Zhang, P. Cao, W. Lin, Q. Liu, Z. Chen, J. Cao, G. Yang, C. Cui, Synergy effect of mixed sintering accelerator on the deoxidation and sintering property improvement of Cu nanoparticles at low temperature, *Applied Physics A* 127(10) (2021).
- [45] Y. Gao, W. Li, C. Chen, H. Zhang, J. Jiu, C.-F. Li, S. Nagao, K. Suganuma, Novel copper particle paste with self-reduction and self-protection characteristics for die attachment of power semiconductor under a nitrogen atmosphere, *Materials & Design* 160 (2018) 1265-1272.

- [46] P.-W. Chou, J.-M. Song, Z.-Y. Xie, M. Akaike, T. Suga, M. Fujino, J.-Y. Lin, Low temperature de-oxidation for copper surface by catalyzed formic acid vapor, *Applied Surface Science* 456 (2018) 890-898.
- [47] R. Gao, S. He, Y.-A. Shen, H. Nishikawa, Effect of Substrates on Fracture Mechanism and Process Optimization of Oxidation–Reduction Bonding with Copper Microparticles, *Journal of Electronic Materials* 48(4) (2019) 2263-2271.
- [48] A. Satta, D. Shamiryan, M.I.R. Baklanov, C.M. Whelan, Q. Toan Le, G.P. Beyer, A. Vantomme, K. Maex, The Removal of Copper Oxides by Ethyl Alcohol Monitored In Situ by Spectroscopic Ellipsometry, *Journal of The Electrochemical Society* 150(5) (2003).
- [49] Y. Yasuda, E. Ide, T. Morita, Evaluation of Copper Oxide-Based Interconnecting Materials, *The Open Surface Science Journal* 3(1) (2010) 123-130.
- [50] S. Krishnan, A.S.M.A. Haseeb, M.R. Johan, Preparation and Low-Temperature Sintering of Cu Nanoparticles for High-Power Devices, *IEEE Transactions on Components, Packaging and Manufacturing Technology* 2(4) (2012) 587-592.
- [51] M.L. Ceron, B. Herrera, P. Araya, F. Gracia, A. Toro-Labbe, The mechanism of methanol decomposition by CuO. A theoretical study based on the reaction force and reaction electronic flux analysis, *J Mol Model* 17(7) (2011) 1625-33.
- [52] A. Soltani, B. Khorramdel Vahed, A. Mardoukhi, M. Mantysalo, Laser sintering of copper nanoparticles on top of silicon substrates, *Nanotechnology* 27(3) (2016) 035203.
- [53] M. Zenou, O. Ermak, A. Saar, Z. Kotler, Laser sintering of copper nanoparticles, *Journal of Physics D: Applied Physics* 47(2) (2014).
- [54] J. Kwon, H. Cho, H. Eom, H. Lee, Y.D. Suh, H. Moon, J. Shin, S. Hong, S.H. Ko, Low-Temperature Oxidation-Free Selective Laser Sintering of Cu Nanoparticle Paste on a Polymer Substrate for the Flexible Touch Panel Applications, *ACS Appl Mater Interfaces* 8(18) (2016) 11575-82.

- [55] H.R. Wallage, J.H. Watterson, Formic acid and methanol concentrations in death investigations, *J Anal Toxicol* 32(3) (2008) 241-7.
- [56] J.Y. Kim, J.A. Rodriguez, J.C. Hanson, A.I. Frenkel, P.L. Lee, Reduction of CuO and Cu₂O with H₂: H embedding and kinetic effects in the formation of suboxides, *J Am Chem Soc* 125(35) (2003) 10684-92.
- [57] S. Nakayama, T. Kaji, M. Shibata, T. Notoya, T. Osakai, Which Is Easier to Reduce, Cu₂O or CuO?, *Journal of The Electrochemical Society* 154(1) (2007).
- [58] J.A. Rodriguez, J.Y. Kim, J.C. Hanson, M. Pérez, A.I. Frenkel, Reduction of CuO in H₂: In Situ Time-Resolved XRD Studies, *Catalysis Letters* 85(3/4) (2003) 247-254.
- [59] T. Ogura, T. Yagishita, S. Takata, T. Fujimoto, A. Hirose, Bondability of Copper Joints Formed Using a Mixed Paste of Ag₂O and CuO for Low-Temperature Sinter Bonding, *Materials Transactions* 54(6) (2013) 860-865.
- [60] T. Yao, T. Matsuda, T. Sano, C. Morikawa, A. Ohbuchi, H. Yashiro, A. Hirose, In Situ Study of Reduction Process of CuO Paste and Its Effect on Bondability of Cu-to-Cu Joints, *Journal of Electronic Materials* 47(4) (2018) 2193-2197.
- [61] S.K. Bhogaraju, O. Mokhtari, F. Conti, G. Elger, Die-attach bonding for high temperature applications using thermal decomposition of copper(II) formate with polyethylene glycol, *Scripta Materialia* 182 (2020) 74-80.
- [62] K.-M. Huang, H. Tsukamoto, Y. Yong, H.-L. Chiu, M.T. Nguyen, T. Yonezawa, Y.-C. Liao, Stabilization of the thermal decomposition process of self-reducible copper ion ink for direct printed conductive patterns, *RSC Advances* 7(40) (2017) 25095-25100.
- [63] Y. Kamikoriyama, H. Imamura, A. Muramatsu, K. Kanie, Ambient Aqueous-Phase Synthesis of Copper Nanoparticles and Nanopastes with Low-Temperature Sintering and Ultra-High Bonding Abilities, *Scientific Reports* 9(1) (2019) 899.

- [64] Y. Zuo, J. Shen, J. Xie, L. Xiang, Influence of Cu micro/nano-particles mixture and surface roughness on the shear strength of Cu-Cu joints, *Journal of Materials Processing Technology* 257 (2018) 250-256.
- [65] S. Yamada, J. Kanno, M. Miyauchi, Multi-sized Sphere Packing in Containers: Optimization Formula for Obtaining the Highest Density with Two Different Sized Spheres, *IPSJ Online Transactions* 4 (2011) 126-133.
- [66] O.U. Uche, F.H. Stillinger, S. Torquato, Concerning maximal packing arrangements of binary disk mixtures, *Physica A: Statistical Mechanics and its Applications* 342(3) (2004) 428-446.
- [67] Y. Zuo, J. Shen, H. Xu, R. Gao, Effect of different sizes of Cu nanoparticles on the shear strength of Cu-Cu joints, *Materials Letters* 199 (2017) 13-16.
- [68] C. Schwarzer, L.M. Chew, M. Schnepf, T. Stoll, J. Franke, M. Kaloudis, U. Aschaffenburg, INVESTIGATION OF COPPER SINTER MATERIAL FOR DIE ATTACH, *SMTA International Conference Proceedings*, 2018.
- [69] T. Hu, H. Chen, M. Li, Die attach materials with high remelting temperatures created by bonding Cu@Sn microparticles at lower temperatures, *Materials & Design* 108 (2016) 383-390.
- [70] J.-W. Yoon, S. Bae, B.-S. Lee, S.-B. Jung, Bonding of power device to ceramic substrate using Sn-coated Cu micro paste for high-temperature applications, *Applied Surface Science* 515 (2020).
- [71] E.B. Choi, J.-H. Lee, Pressure-assisted sinter bonding method at 300 °C in air using a resin-free paste containing 1.5 μm Cu@Ag particles, *Applied Surface Science* 546 (2021).
- [72] C. Tuo, Z. Yao, W. Liu, S. Liu, L. Liu, Z. Chen, S. Huang, C. Liu, X. Cao, Fabrication and characteristics of Cu@Ag composite solder preform by electromagnetic compaction for power electronics, *Journal of Materials Processing Technology* 292 (2021) 117056.

- [73] Y. Zuo, J. Shen, Y. Hu, R. Gao, Improvement of oxidation resistance and bonding strength of Cu nanoparticles solder joints of Cu–Cu bonding by phosphating the nanoparticle, *Journal of Materials Processing Technology* 253 (2018) 27-33.
- [74] K.S. Tan, K.Y. Cheong, Mechanical properties of sintered Ag–Cu die-attach nanopaste for application on SiC device, *Materials & Design* 64 (2014) 166-176.
- [75] J. Yan, G. Zou, A. Wu, J. Ren, A. Hu, Y.N. Zhou, Polymer-Protected Cu-Ag Mixed NPs for Low-Temperature Bonding Application, *Journal of Electronic Materials* 41(7) (2012) 1886-1892.
- [76] J. Yan, G. Zou, Y. Zhang, J. Li, L. Liu, A. Wu, Y.N. Zhou, Metal-Metal Bonding Process Using Cu+Ag Mixed Nanoparticles, *Materials Transactions* 54(6) (2013) 879-883.
- [77] T. Ishizaki, R. Watanabe, Pressureless Bonding by Use of Cu and Sn Mixed Nanoparticles, *Journal of Electronic Materials* 43(12) (2014) 4413-4420.
- [78] W. Wang, G. Zou, Q. Jia, H. Zhang, B. Feng, Z. Deng, L. Liu, Mechanical properties and microstructure of low temperature sintered joints using organic-free silver nanostructured film for die attachment of SiC power electronics, *Materials Science and Engineering: A* 793 (2020).
- [79] Y.-c. Liu, S.-k. Lin, H. Zhang, S. Nagao, C. Chen, K. Suganuma, Reactive wafer bonding with nanoscale Ag/Cu multilayers, *Scripta Materialia* 184 (2020) 1-5.
- [80] Y. Zhong, R. An, H. Ma, C. Wang, Low-temperature-solderable intermetallic nanoparticles for 3D printable flexible electronics, *Acta Materialia* 162 (2019) 163-175.
- [81] Y. Zhong, R. An, C. Wang, Z. Zheng, Z.Q. Liu, C.H. Liu, C.F. Li, T.K. Kim, S. Jin, Low Temperature Sintering Cu₆Sn₅ Nanoparticles for Superplastic and Super-uniform High Temperature Circuit Interconnections, *Small* 11(33) (2015) 4097-103.
- [82] S.E. Kim, S. Kim, Wafer level Cu–Cu direct bonding for 3D integration, *Microelectronic Engineering* 137 (2015) 158-163.

- [83] C. Okoro, R. Agarwal, P. Limaye, B. Vandeveld, D. Vandepitte, E. Beyne, Insertion bonding: A novel Cu-Cu bonding approach for 3D integration, 2010 Proceedings 60th Electronic Components and Technology Conference (ECTC), 2010, pp. 1370-1375.
- [84] H. Takagi, R. Maeda, T.R. Chung, N. Hosoda, T. Suga, Effect of Surface Roughness on Room-Temperature Wafer Bonding by Ar Beam Surface Activation, *Japanese Journal of Applied Physics* 37(Part 1, No. 7A) (1998) 4197-4203.
- [85] T.H. Kim, M.M.R. Howlader, T. Itoh, T. Suga, Room temperature Cu-Cu direct bonding using surface activated bonding method, *Journal of Vacuum Science & Technology A: Vacuum, Surfaces, and Films* 21(2) (2003) 449-453.
- [86] Y.-P. Huang, Y.-S. Chien, R.-N. Tzeng, K.-N. Chen, Demonstration and Electrical Performance of Cu-Cu Bonding at 150 °C With Pd Passivation, *IEEE Transactions on Electron Devices* 62(8) (2015) 2587-2592.
- [87] Y.-P. Huang, Y.-S. Chien, R.-N. Tzeng, M.-S. Shy, T.-H. Lin, K.-H. Chen, C.-T. Chiu, J.C. Chiou, C.-T. Chuang, W. Hwang, H.-M. Tong, K.-N. Chen, Novel Cu-to-Cu Bonding With Ti Passivation at 180° in 3-D Integration, *IEEE Electron Device Letters* 34 (2013) 1551-1553.
- [88] C.-M. Liu, H.-W. Lin, Y.-S. Huang, Y.-C. Chu, C. Chen, D.-R. Lyu, K.-N. Chen, K.-N. Tu, Low-temperature direct copper-to-copper bonding enabled by creep on (111) surfaces of nanotwinned Cu, *Scientific Reports* 5(1) (2015) 9734.
- [89] J.-Y. Juang, C.-L. Lu, K.-J. Chen, C.-C.A. Chen, P.-N. Hsu, C. Chen, K.N. Tu, Copper-to-copper direct bonding on highly (111)-oriented nanotwinned copper in no-vacuum ambient, *Scientific Reports* 8(1) (2018) 13910.
- [90] L. Guo, W. Liu, X. Ji, Y. Zhong, C. Hang, C. Wang, Robust Cu-Cu Bonding with Multiscale Coralloid Nano-Cu₃Sn Paste for High-Power Electronics Packaging, *ACS Applied Electronic Materials* 4(7) (2022) 3457-3469.

- [91] Y. Qiao, H. Ma, F. Yu, N. Zhao, Quasi-in-situ observation on diffusion anisotropy dominated asymmetrical growth of Cu-Sn IMCs under temperature gradient, *Acta Materialia* 217 (2021).
- [92] S.R.K. Malladi, F.D. Tichelaar, Q. Xu, M.Y. Wu, H. Terryn, J.M.C. Mol, F. Hannour, H.W. Zandbergen, Quasi in situ analytical TEM to investigate electrochemically induced microstructural changes in alloys: AA2024-T3 as an example, *Corrosion Science* 69 (2013) 221-225.
- [93] G.M. Bremmer, L. Haandel, E.J.M. Hensen, J. Frenken, P. Kooyman, A Quasi In Situ HRTEM Study of the Air Stability of (Ni/Co)MoS₂ Hydrodesulfurization Catalysts, *Microscopy and Microanalysis* 21 (2015) 801-802.
- [94] P. Guo, Y. Gao, Coalescence of Au Nanoparticles without Ligand Detachment, *Physical Review Letters* 124(6) (2020) 066101.
- [95] J.C. Love, L.A. Estroff, J.K. Kriebel, R.G. Nuzzo, G.M. Whitesides, Self-Assembled Monolayers of Thiolates on Metals as a Form of Nanotechnology, *Chemical Reviews* 105(4) (2005) 1103-1170.
- [96] P.N. Amaniampong, Q.T. Trinh, J.J. Varghese, R. Behling, S. Valange, S.H. Mushrif, F. Jérôme, Unraveling the mechanism of the oxidation of glycerol to dicarboxylic acids over a sonochemically synthesized copper oxide catalyst, *Green Chemistry* 20(12) (2018) 2730-2741.
- [97] Q. Yang, Z. Guo, X. Zhou, J. Zou, S. Liang, Ultrathin CuO nanowires grown by thermal oxidation of copper powders in air, *Materials Letters* 153 (2015) 128-131.
- [98] M. Lee, A.J.H. McGaughey, Energetics and kinetics of the (2×2) to $(2\sqrt{2} \times \sqrt{2})R45^\circ$ transition during the early stages of Cu(100) oxidation, *Physical Review B* 83(16) (2011) 165447.
- [99] P.A. Mulheran, J.A. Blackman, The origins of island size scaling in heterogeneous film growth, *Philosophical Magazine Letters* 72(1) (1995) 55-60.

- [100] C. Gattinoni, A. Michaelides, Atomistic details of oxide surfaces and surface oxidation: the example of copper and its oxides, *Surface Science Reports* 70(3) (2015) 424-447.
- [101] L.I. Hung, C.K. Tsung, W. Huang, P. Yang, Room-temperature formation of hollow Cu₂O nanoparticles, *Adv Mater* 22(17) (2010) 1910-4.
- [102] G. Zhou, L. Wang, J.C. Yang, Effects of surface topology on the formation of oxide islands on Cu surfaces, *Journal of Applied Physics* 97(6) (2005).
- [103] J.C. Yang, M. Yeadon, B. Kolasa, J.M. Gibson, The Limited Role of Surface Defects as Nucleation Sites for Cu₂O on Cu(001), *Journal of The Electrochemical Society* 146(6) (1999) 2103-2106.
- [104] R.I. Made, C.L. Gan, L. Yan, K.H.B. Kor, H.L. Chia, K.L. Pey, C.V. Thompson, Experimental characterization and modeling of the mechanical properties of Cu–Cu thermocompression bonds for three-dimensional integrated circuits, *Acta Materialia* 60(2) (2012) 578-587.
- [105] L. Yuan, Y. Wang, R. Mema, G. Zhou, Driving force and growth mechanism for spontaneous oxide nanowire formation during the thermal oxidation of metals, *Acta Materialia* 59(6) (2011) 2491-2500.
- [106] <Effects of Joining Conditions on Joint Strength of CuCu Joint Using Cu Nanoparticle Paste.pdf>.
- [107] J. Mittal, K.-L. Lin, Exothermic low temperature sintering of Cu nanoparticles, *Materials Characterization* 109 (2015) 19-24.
- [108] E.-K. Yu, L. Piao, S.-H. Kim, Sintering Behavior of Copper Nanoparticles, *Bulletin of the Korean Chemical Society* 32(11) (2011) 4099-4102.
- [109] <Evaluation of Copper Oxide-Based Interconnecting Materials.pdf>.

- [110] C.-J. Wu, S.-L. Cheng, Y.-J. Sheng, H.-K. Tsao, Reduction-assisted sintering of micron-sized copper powders at low temperature by ethanol vapor, *RSC Advances* 5(66) (2015) 53275-53279.
- [111] C.-H. Hsiao, W.-T. Kung, J.-M. Song, J.-Y. Chang, T.-C. Chang, Development of Cu-Ag pastes for high temperature sustainable bonding, *Materials Science and Engineering: A* 684 (2017) 500-509.
- [112] G. Ferik, J. Stergar, M. Drogenik, D. Makovec, A. Hamler, Z. Jagličić, I. Ban, The synthesis and characterization of nickel-copper alloy nanoparticles with a narrow size distribution using sol-gel synthesis, *Materials Letters* 124 (2014) 39-42.
- [113] T. Ishizaki, R. Watanabe, A new one-pot method for the synthesis of Cu nanoparticles for low temperature bonding, *Journal of Materials Chemistry* 22(48) (2012) 25198.
- [114] M. Song, G. Zhou, N. Lu, J. Lee, E. Nakouzi, H. Wang, D. Li, Oriented attachment induces fivefold twins by forming and decomposing high-energy grain boundaries, *Science* 367(6473) (2020) 40-45.
- [115] D. Li, M.H. Nielsen, J.R. Lee, C. Frandsen, J.F. Banfield, J.J. De Yoreo, Direction-specific interactions control crystal growth by oriented attachment, *Science* 336(6084) (2012) 1014-8.
- [116] Z. Aabdin, J. Lu, X. Zhu, U. Anand, N.D. Loh, H. Su, U. Mirsaidov, Bonding Pathways of Gold Nanocrystals in Solution, *Nano Letters* 14(11) (2014) 6639-6643.
- [117] A.P. Lange, A. Samanta, H. Majidi, S. Mahajan, J. Ging, T.Y. Olson, K. van Benthem, S. Elhadj, Dislocation mediated alignment during metal nanoparticle coalescence, *Acta Materialia* 120 (2016) 364-378.
- [118] T. Kozawa, K. Yanagisawa, Grain growth of titania to submillimeter sizes using water vapor-assisted sintering, *Journal of Materials Research* 34(3) (2018) 474-480.

- [119] E.A. Olevsky, Theory of sintering: from discrete to continuum, *Materials Science and Engineering: R: Reports* 23(2) (1998) 41-100.
- [120] H. Youhua, L. Yimin, L. Jia, H. Hao, Z. Xiang, Effects of Sintering Temperature and Holding Time on Densification and Mechanical Properties of MIM HK30 Stainless Steel, *International Journal of Metallurgy and Metal Physics* 3(2) (2018).
- [121] H. Hao, Y. Wang, H.R. Jafari Nodooshan, Y. Zhang, S. Ye, Y. Lv, P. Yu, The Effects of Sintering Temperature and Addition of TiH₂ on the Sintering Process of Cu, *Materials (Basel)* 12(16) (2019).
- [122] R.M. German, S.J. Park, *Handbook of mathematical relations in particulate materials processing: ceramics, powder metals, cermets, carbides, hard materials, and minerals*, John Wiley & Sons 2009.
- [123] L. Ding, R.L. Davidchack, J. Pan, A molecular dynamics study of sintering between nanoparticles, *Computational Materials Science* 45(2) (2009) 247-256.
- [124] R. Theissmann, M. Fendrich, R. Zinetullin, G. Guenther, G. Schierning, D.E. Wolf, Crystallographic reorientation and nanoparticle coalescence, *Physical Review B* 78(20) (2008).
- [125] S. Zhang, Q. Wang, T. Lin, P. Zhang, P. He, K.-W. Paik, Cu-Cu joining using citrate coated ultra-small nano-silver pastes, *Journal of Manufacturing Processes* 62 (2021) 546-554.
- [126] A. Halder, N. Ravishankar, Ultrafine Single-Crystalline Gold Nanowire Arrays by Oriented Attachment, *Advanced Materials* 19(14) (2007) 1854-1858.
- [127] L. Lu, Y. Shen, X. Chen, L. Qian, K. Lu, Ultrahigh strength and high electrical conductivity in copper, *Science* 304(5669) (2004) 422-6.
- [128] R. Ristau, R. Tiruvalam, P.L. Clasen, E.P. Gorskowski, M.P. Harmer, C.J. Kiely, I. Hussain, M. Brust, Electron microscopy studies of the thermal stability of gold nanoparticle arrays, *Gold Bulletin* 42(2) (2009) 133-143.

- [129] L. Lu, X. Chen, X. Huang, K. Lu, Revealing the maximum strength in nanotwinned copper, *Science* 323(5914) (2009) 607-10.
- [130] Z.Z. Fang, H. Wang, Densification and grain growth during sintering of nanosized particles, *International Materials Reviews* 53(6) (2013) 326-352.
- [131] S.H. Huo, M. Qian, G.B. Schaffer, E. Crossin, 21 - Aluminium powder metallurgy, in: R. Lumley (Ed.), *Fundamentals of Aluminium Metallurgy*, Woodhead Publishing 2011, pp. 655-701.
- [132] N. Heuck, S. Müller, G. Palm, A. Bakin, A. Waag, Swelling Phenomena in Sintered Silver Die Attach Structures at High Temperatures: Reliability Problems and Solutions for an Operation above 350°C, *Additional Conferences (Device Packaging, HiTEC, HiTEN, and CICMT) 2010(HITEC)* (2010) 000018-000025.
- [133] R. Kimura, Y. Kariya, N. Mizumura, K. Sasaki, Effect of Sintering Temperature on Fatigue Crack Propagation Rate of Sintered Ag Nanoparticles, *Materials Transactions* 59(4) (2018) 612-619.
- [134] Y. Zuo, S. Carter-Searjeant, M. Green, L. Mills, S.H. Mannan, Low temperature Cu joining by in situ reduction-sintering of CuO nanoparticle for high power electronics, *Advanced Powder Technology* 31(10) (2020) 4135-4144.
- [135] S. Koga, H. Nishikawa, M. Saito, J. Mizuno, Fabrication of Nanoporous Cu Sheet and Application to Bonding for High-Temperature Applications, *Journal of Electronic Materials* 49(3) (2020) 2151-2158.
- [136] J. Xie, J. Shen, J. Deng, X. Chen, Influence of Aging Atmosphere on the Thermal Stability of Low-Temperature Rapidly Sintered Cu Nanoparticle Paste Joint, *Journal of Electronic Materials* 49(4) (2020) 2669-2676.

- [137] Y. Gao, J. Jiu, C. Chen, K. Suganuma, R. Sun, Z.-Q. Liu, Oxidation-enhanced bonding strength of Cu sinter joints during thermal storage test, *Journal of Materials Science & Technology* 115 (2022) 251-255.
- [138] S. Nilsson, M. Nielsen, J. Fritzsche, C. Langhammer, S. Kadkhodazadeh, Unravelling Competing Oxidation Mechanisms in Single Cu Nanoparticles, *Research Square*, 2022.
- [139] Y. Zuo, S. Carter-Searjeant, M. Green, L. Mills, S.H. Mannan, High bond strength Cu joints fabricated by rapid and pressureless in situ reduction-sintering of Cu nanoparticles, *Materials Letters* 276 (2020).
- [140] Y. Zuo, C. Zhao, A. Robador, M. Wickham, S.H. Mannan, Quasi-in-situ observation of the grain growth and grain boundary movement in sintered Cu nanoparticle interconnects, *Acta Materialia* 236 (2022) 118135.
- [141] E. Kirkendall, Diffusion of zinc in alpha brass, *Trans. Aime* 147 (1942) 104-110.
- [142] E. Kirkendall, A. Smigelskas, Zinc diffusion in alpha brass, *Aime Trans* 171 (1947) 130-142.
- [143] M. Lee, A.J.H. McGaughey, Energetics and kinetics of the (2×2) to (22×2) $R45^\circ$ transition during the early stages of Cu(100) oxidation, *Physical Review B* 83(16) (2011).
- [144] S. Nilsson, D. Albinsson, T.J. Antosiewicz, J. Fritzsche, C. Langhammer, Resolving single Cu nanoparticle oxidation and Kirkendall void formation with in situ plasmonic nanospectroscopy and electrodynamic simulations, *Nanoscale* 11(43) (2019) 20725-20733.
- [145] D. Albinsson, S. Nilsson, T.J. Antosiewicz, V.P. Zhdanov, C. Langhammer, Heterodimers for in Situ Plasmonic Spectroscopy: Cu Nanoparticle Oxidation Kinetics, Kirkendall Effect, and Compensation in the Arrhenius Parameters, *The Journal of Physical Chemistry C* 123(10) (2019) 6284-6293.

Appendix

1. Etching treatment

Cu nanoparticles readily oxidize and the oxide will form during high temperature heating even under a high purity of N₂. For the quasi-in-situ observation, the Cu joint needs to be slightly etched by ion beam milling at 4 KV for only 2 minutes after every heating step to clean the slightly oxidized Cu surface and make the GB visible again. The etching time would vary with different sample size and polishing voltage, and some machines have a more powerful ion beam launcher which would also shorten the etching time. 2 minutes at 4 kV or 1 minutes at 5 kV are only based on my experience and the specific ion beam miller I used (JEOL SM-09010).

Basically, the minimum polishing time for most of ion beam millers is 1 minute and the swing mode needs to be turned on during the etching to avoid scratches. The updated ion beam miller (i.e. Hitachi IM4000) is able to finish one swing cycle even within 5 seconds. Therefore, one can stop the etching manually and bring the minimum polishing time down to 5 seconds. The suitable polishing voltage for metal is between 4-6 kV. It is suggested that using the minimum polishing time of the ion beam miller at 4 kV to find the suitable etching time and avoid damaging the sample surface. The sample need to be checked by SEM to see if the etching is finished and can be etched again when the GB is still invisible. There is no need to etch for those metals with good oxidation resistance (i.e. Ag or Au) and high vacuum or inert gas sintering condition. (relevant to Section 3.7)

2. EDS result

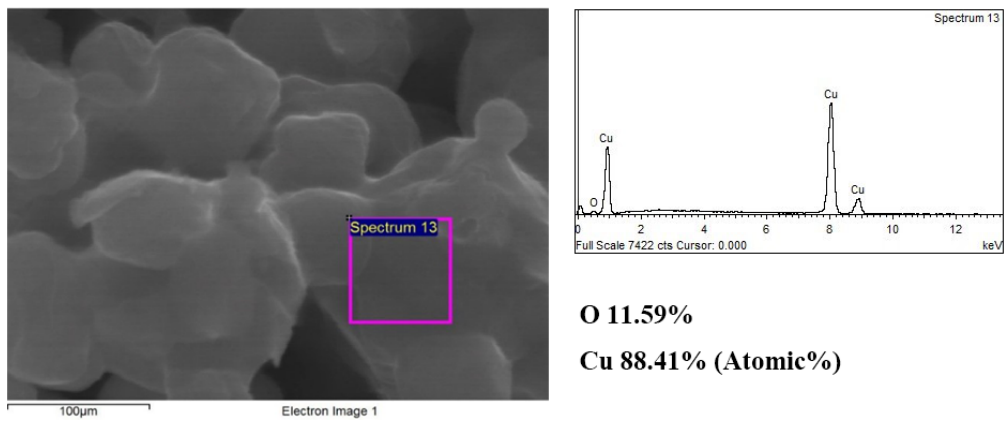


Figure A1 EDS results of reduced Cu particles after sintering at 220 °C for 15 min.

(relevant to Section 4.4.2)

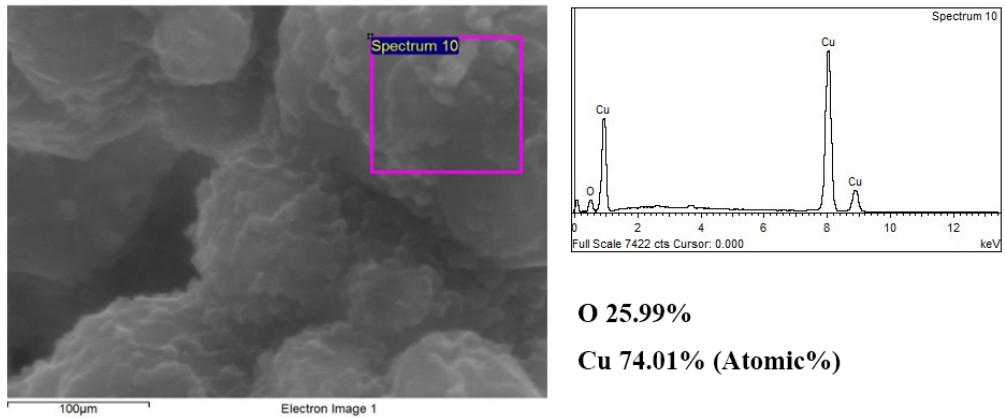


Figure A2 EDS results of reduced Cu particles after sintering at 220 °C for 40 min.

(relevant to Section 4.4.2)

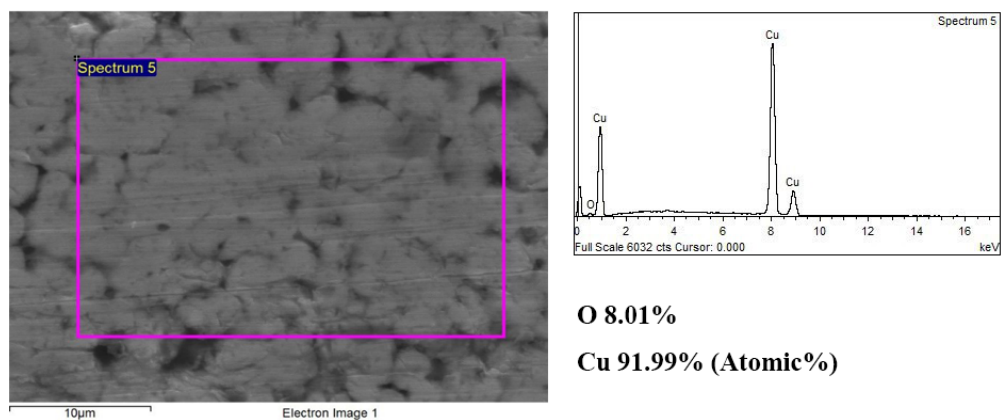
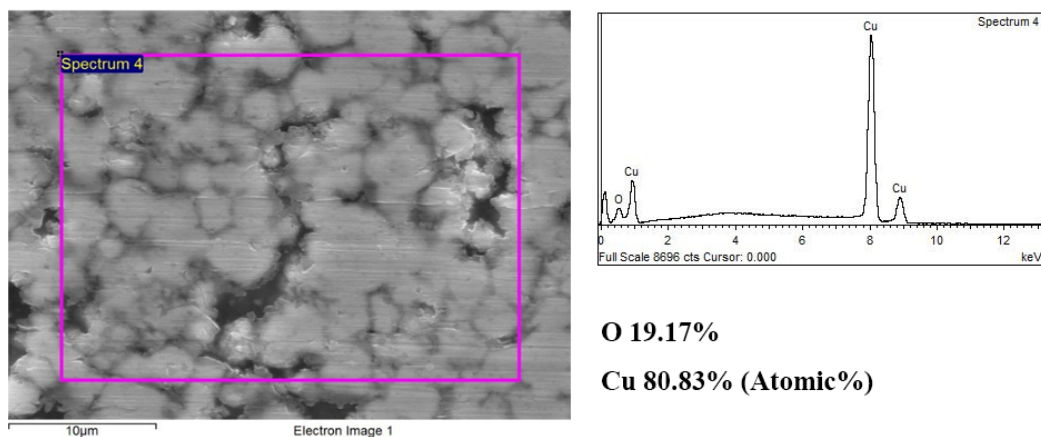


Figure A3 EDS results of cross section of joint after sintering at 220 °C for 15 min.

(relevant to Section 4.4.2)



**Figure A4 EDS results of cross section of joint after sintering at 220 °C for 40 min.
(relevant to Section 4.4.2)**

In order to eliminate the influence of C introducing from the environment and polishing process, clean Cu substrate cross section after ion beam polishing was first detected by EDS (Zeiss EVO LS15 SEM with EDS Analysis). The mean C and O content of ten different areas in the Cu substrate is 7.9 ± 0.3 wt.% and 0 wt.% as shown in the following image, respectively.

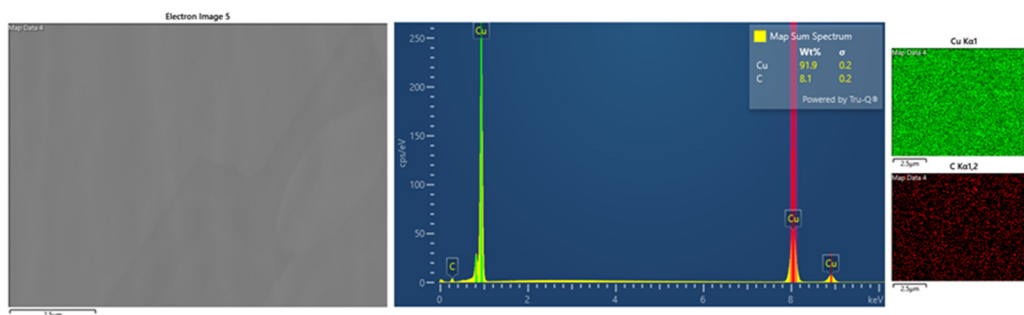


Figure A5 Representative EDS results of Cu substrate. (relevant to Section 6.4.1)

The mean C and O content of ten different areas of both the fracture surface and cross section of the sintered Cu structure at 220 °C and 20 min is 8.7 ± 0.6 wt.% and 0.4 ± 0.1 wt.% as shown in the following image, respectively. Therefore, the contents of organic residue and oxide are limited in the sintered Cu structure.

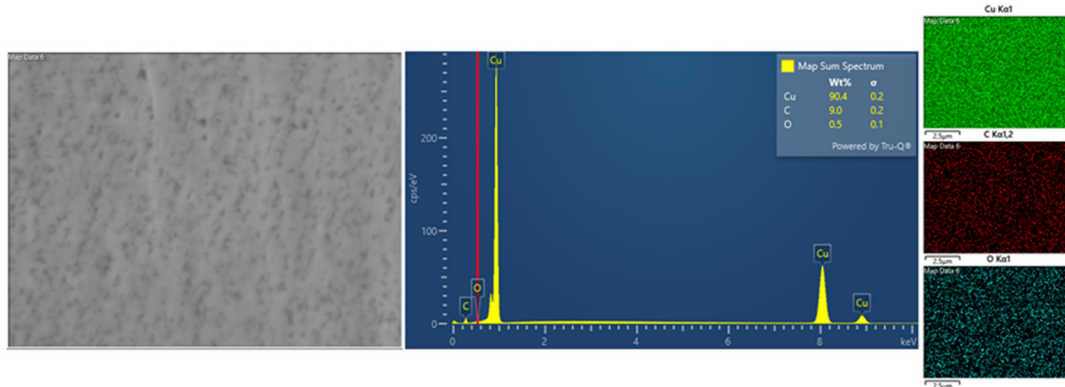


Figure A6 Representative EDS results of sintered Cu structure. (relevant to Section 6.4.1)

3. Grain size and pore size/shape distribution

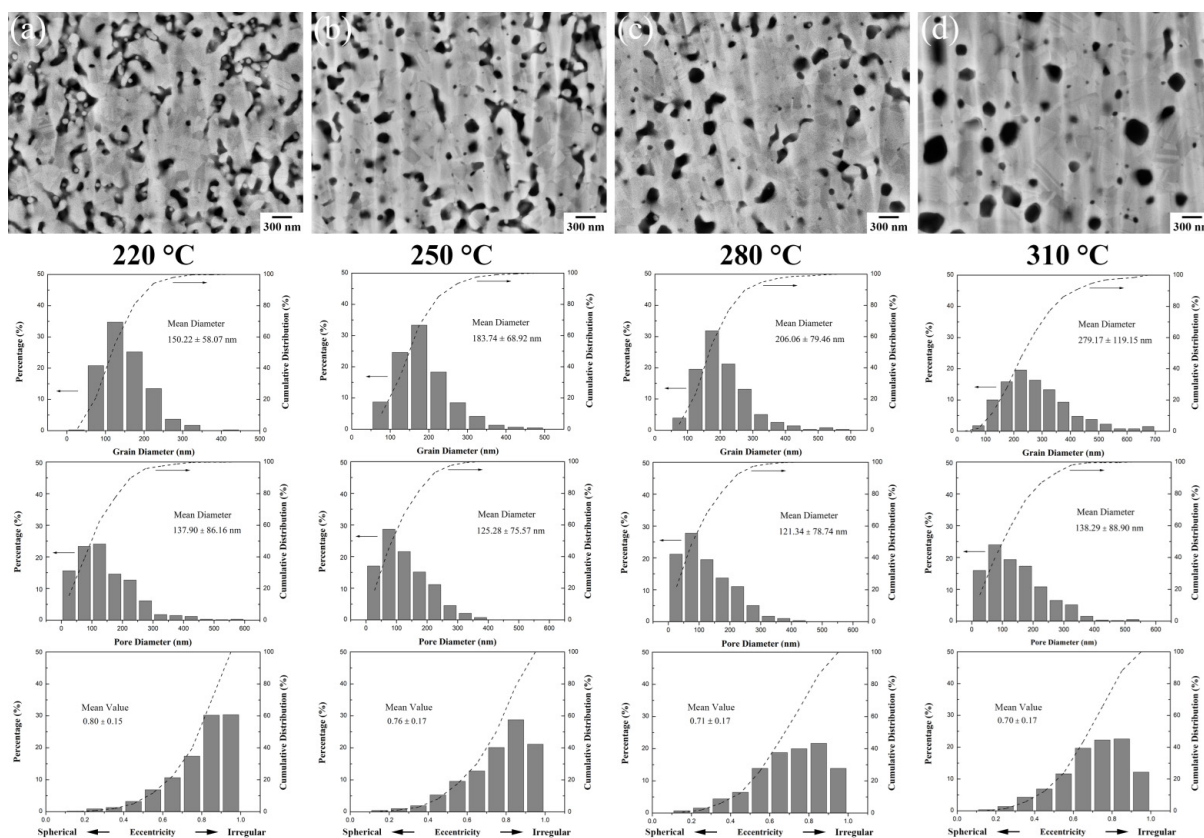
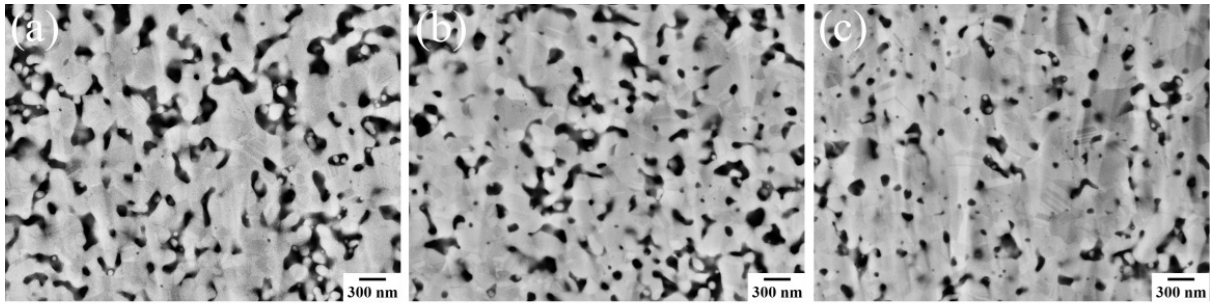


Figure A7 SEM cross section image and grain size and pore size/shape distribution of sintered Cu nanoparticles at 220 °C (a), 250 °C (b), 280 °C (c) and 310 °C (d) for 5 min. (relevant to Section 6.4.1)



220 °C 5 min

10 min

20 min

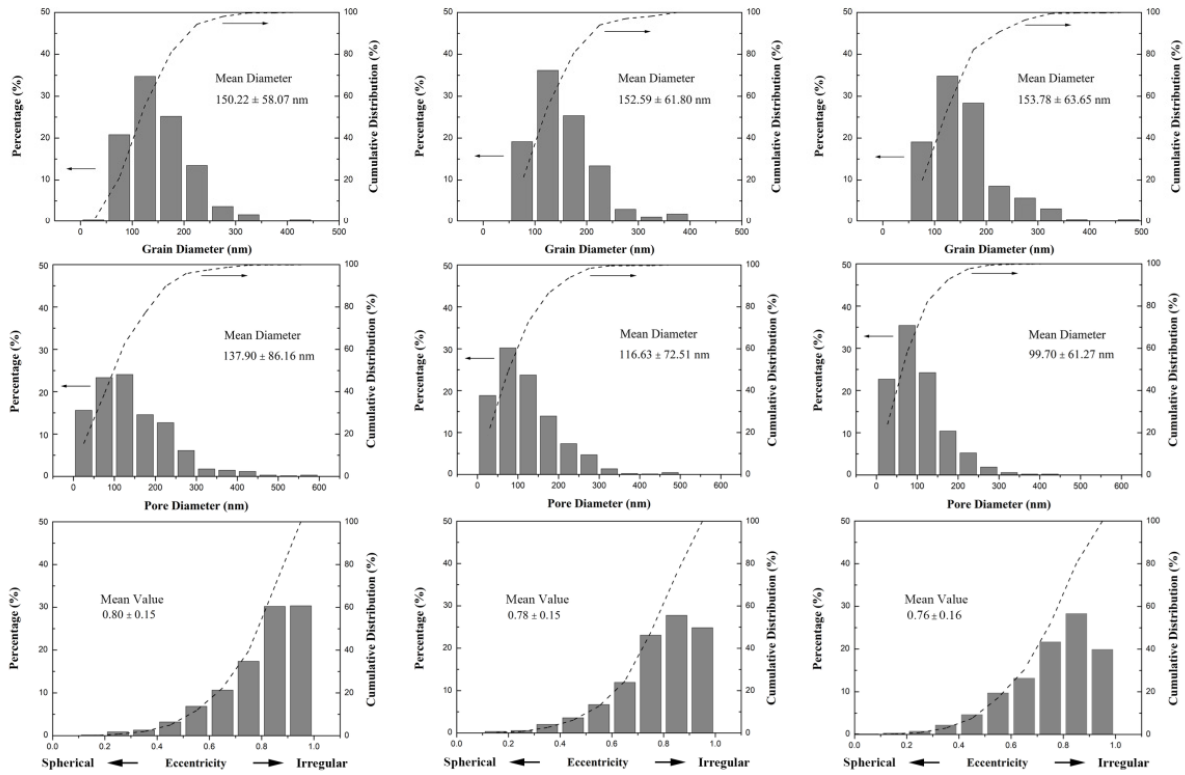


Figure A8 SEM cross section image and grain size and pore size/shape distribution of sintered Cu nanoparticles at 220 °C for 5 min (a), 10 min (b) and 20 min (c). (relevant to Section 6.4.2)

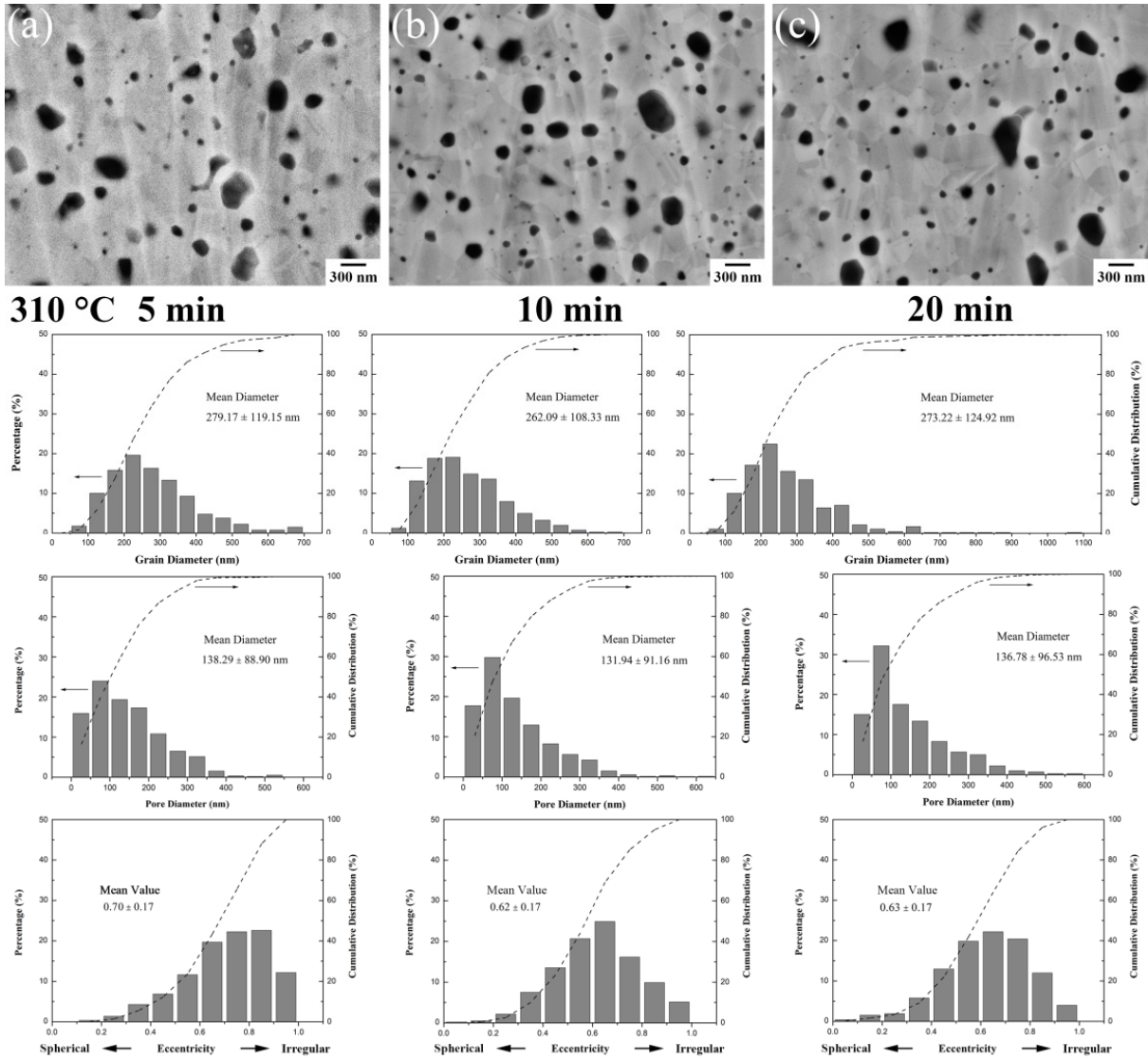


Figure A9 SEM cross section image and grain size and pore size/shape distribution of sintered Cu nanoparticles at 310 °C for 5 min (a), 10 min (b) and 20 min (c). (relevant to Section 6.4.2)

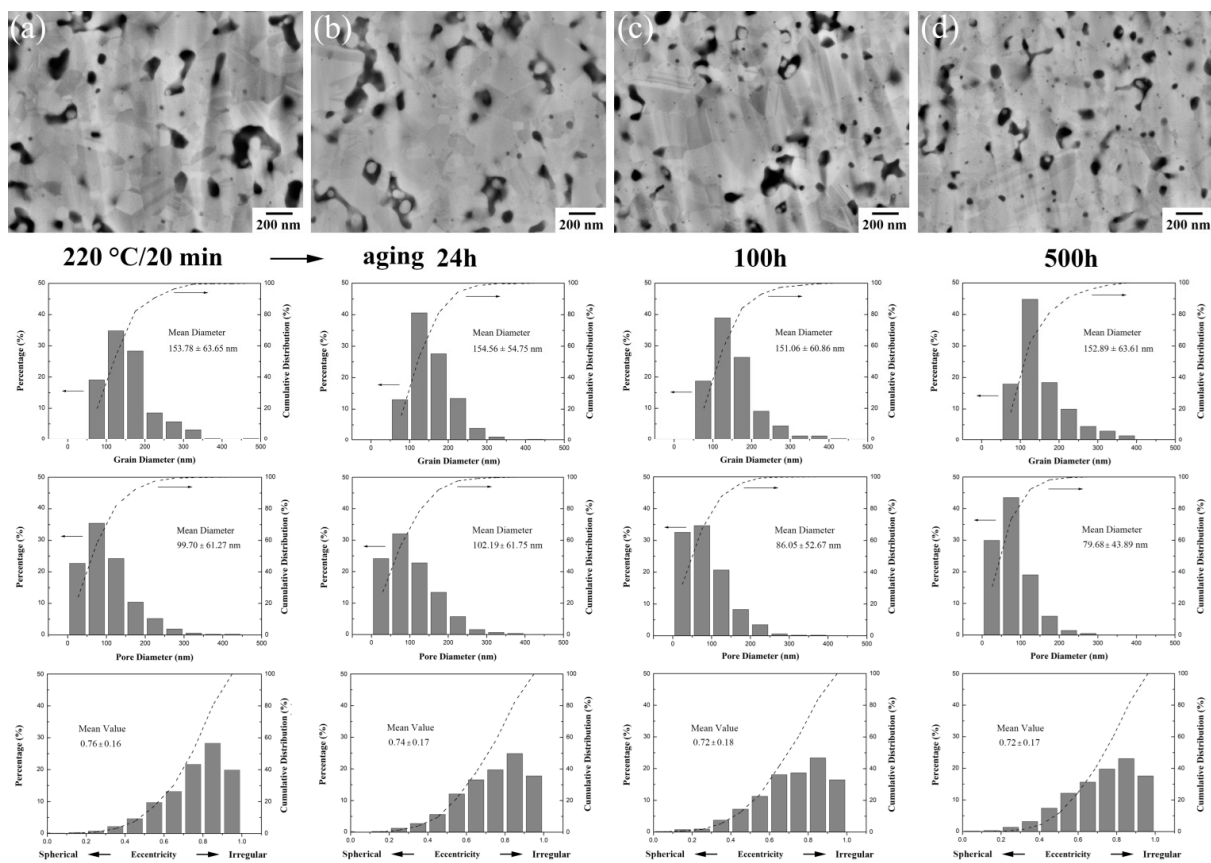


Figure A10 SEM cross section image and grain size, pore size/shape distribution of sintered Cu nanoparticles after aging for 0 h (a), 24 h (b), 100 h (c) and 500 h (d).

(relevant to Section 7.4.1)

4. Shear test

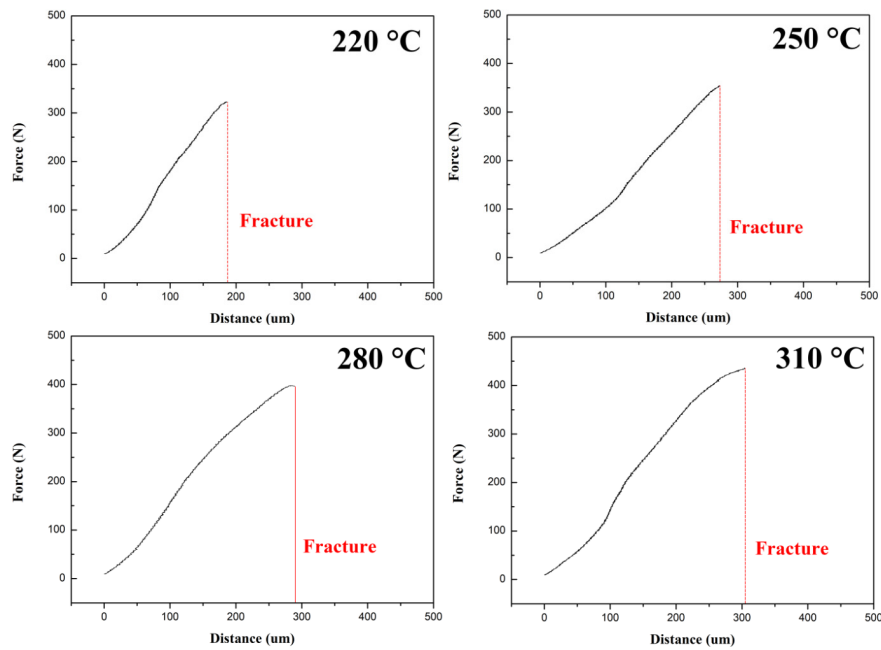


Figure A11 Force-displacement curves of joint with different temperatures during shearing force measurement. (relevant to Section 6.4.1)

5. Joint fracture

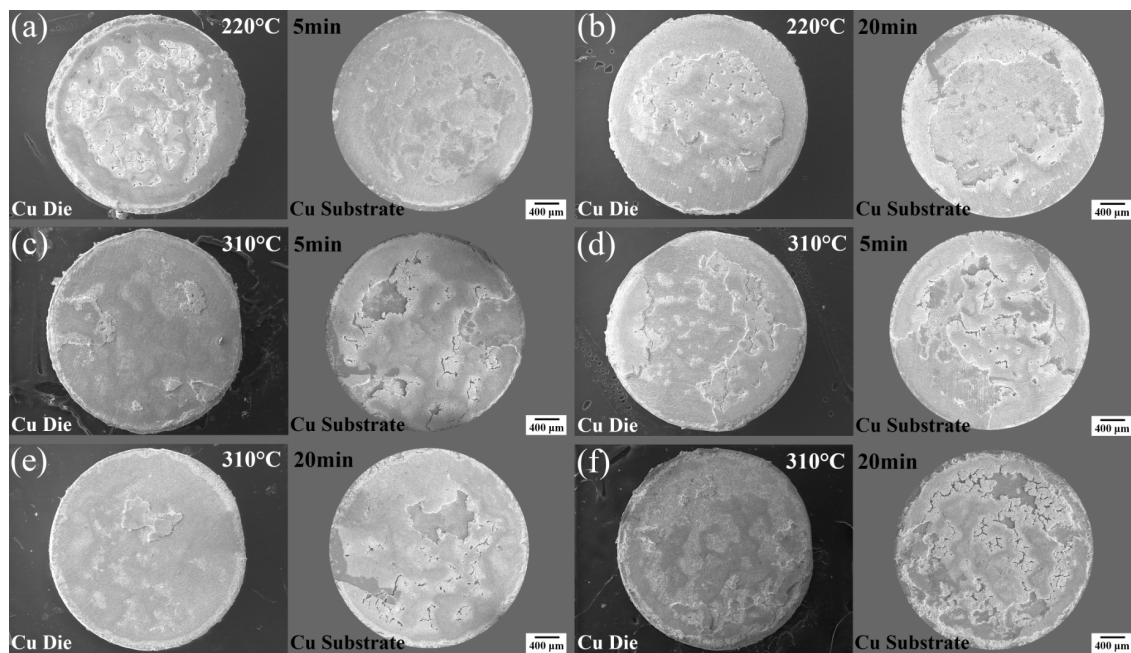


Figure A12 SEM fracture surface images of joints for different bonding conditions.

(relevant to Section 6.4.4)

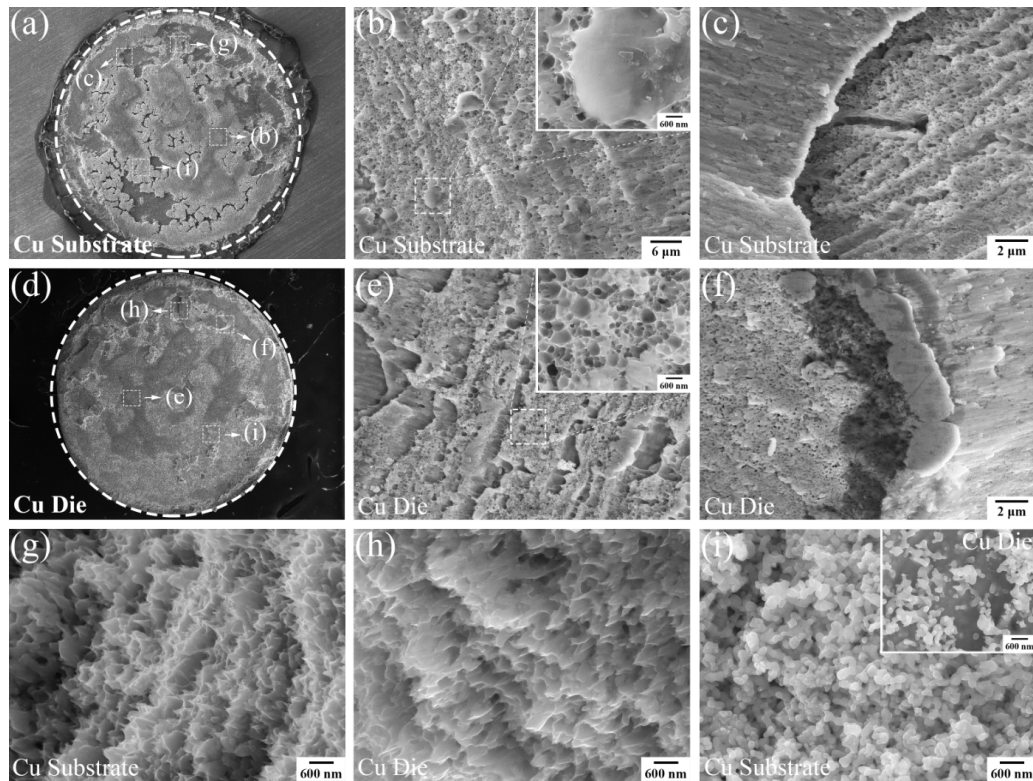


Figure A13 Representative SEM fracture surface image of joint bonded at 310 °C for 20 min. Areas on Cu substrate: (a), (b), (c), (g) and (i), corresponding areas on Cu die: (d), (e), (f), (h) and the inset of and (i). (relevant to Section 6.4.4)

6. Statistical Significance

T-tests were used to assess the means of grain size, pore size/number and strength of sintered Cu structure for different aging conditions. The calculation was conducted by Excel. T-tests are useful to check if two group means are different when they have significant different variances. It should be noted that the strength of joints increases and the porosity of sintered Cu decreases with the sintering temperature or time in most cases and these parameters will be analyze by the one tailed T-tests. And the data groups with similar mean value and standard deviation usually show insignificant difference in the means and there is no need for T-tests. For example, the pore sizes of sintered Cu aged for 0 h (99.70 ± 61.27 , nm) and 24 h (102.19 ± 61.75 , nm) in Chapter 7 share similar mean value and standard deviation. The relevant t-value and p-value

for standard two tailed T-test are -0.651494655 and 0.51481277, respectively. Since the p-value > 0.05 , there is insignificant difference in the mean pore size for 0 h and 24 h aging.

The t-value and p-value for one tailed T-test of shear strength in Chapter 6 for 220 °C/5 min (27.38 ± 2.79 , MPa) and 310 °C/5 min (30.54 ± 3.45 , MPa) sintering are -1.592933708 and 0.074920233, respectively. Since the p-value > 0.05 , there is insignificant difference in the mean shear strength for 220 °C/5 min and 310 °C/5 min. There is also insignificant difference in the mean shear strength for 310 °C/5 min (30.54 ± 3.45 , MPa) and 310 °C/20 min (32.70 ± 4.90 , MPa), $p: 0.224019053 > 0.05$, and for 220 °C/5 min (27.38 ± 2.79 , MPa) and 220 °C/20 min (30.88 ± 3.54 , MPa), $p: 0.060194522 > 0.05$. The possible reason for the insignificant difference in the mean joint shear strength under different sintering conditions could be the vulnerable joint and pressureless sintering process. The dummy Cu chip and substrate diameters are only 4 and 8 mm and the thicknesses are only 2 and 3 mm, respectively. Any slight change in the bonding process or shear test will cause different shear result. Meanwhile, these specific Cu chips/substrates are not customized from suppliers but are made from the mechanical cutting (diamond saw, small and simple machine in the lab) of Cu rod. The Cu discs after cutting were then polished by emery paper and their surfaces are not perfectly flat in both horizontal and vertical directions, which could cause a slight difference in the bonding strength even with same sintering conditions. These results could be responsible for the large variance of joint shear strength for each condition and insignificant difference in the mean shear strength for different conditions. Meanwhile, the assistance of pressure during sintering can significantly increase the strength of sintered Cu and also the gap between the strength for different sintering conditions, which could result in significant difference in the mean joint shear strength for different conditions. However, the sintering was carried out under zero pressure in this thesis. The statistical significance results may not fully support the conclusion that the joint strength increases with the sintering temperature or time, but the results of joint

strength in Chapter 6 are consistent with an increase in the shear strength and require further work to fully validate the conclusion.

The t-value and p-value for one tailed T-test of bulk sintered Cu porosity in Chapter 6 for 280 °C/5 min (12.89 ± 2.06 , %) and 310 °C/5 min (11.65 ± 1.35 , %) sintering are 1.94543534 and 0.031101588, respectively. Since $0.05 > p\text{-value} > 0.01$, there is significant difference in the mean porosity for 280 °C/5 min and 310 °C/5 min sintering. Therefore, the porosity decreases slightly when the temperature increases from 280 °C to 310 °C. The t-value and p-value for one tailed T-test of bulk sintered Cu porosity in Chapter 6 for 310 °C/5 min (11.65 ± 1.35 , %) and 310 °C/20 min (10.90 ± 1.66 , %) sintering are 1.480763696 and 0.073066484, respectively. Since the $p\text{-value} > 0.05$, there is insignificant difference in the mean porosity for 310 °C/5 min and 310 °C/20 min sintering. Therefore, the porosity changes little with increasing the sintering times at 310 °C.

The t-value and p-value for two tailed T-test of pore size in Chapter 6 for 220 °C/5 min (137.90 ± 86.16 , nm) and 220 °C/20 min (99.70 ± 61.27 , nm) sintering are -9.568721213 and 5.62E-21, respectively. Since the $p\text{-value} < 0.01$, there is highly significant difference in the mean pore size for 220 °C/5 min and 220 °C/20 min sintering. Therefore, the pore size decreases with increasing the sintering times.

The t-value and p-value for two tailed T-test of pore size in Chapter 7 for 0 h (99.70 ± 61.27 , nm) and 500 h (79.68 ± 43.89 , nm) aging are 8.049297 and 1.61315E-15, respectively. Since the $p\text{-value} < 0.01$, there is highly significant difference in the mean pore size for 0 h and 500 h aging. Therefore, the pore size decreases with increasing the aging times.

The t-value and p-value for one tailed T-test of porosity in Chapter 7 for 0 h (12.74 ± 2.18 , %) and 500 h (9.94 ± 1.56 , %) aging are 7.135663016 and 1.24031E-09, respectively. Since the $p\text{-value} < 0.01$, there is highly significant difference in the mean porosity for 0 h and 500 h aging. Therefore, the porosity decreases slightly with increasing the aging times.

The t-value and p-value for two tailed T-test of shear strength in Chapter 7 for 0 h (26.66 ± 4.63 , MPa) and 100 h (31.97 ± 1.75 , MPa) aging are -2.776279466 and 0.039073724 , respectively. Since $0.05 > p\text{-value} > 0.01$, there is significant difference in the mean shear strength for 0 h and 100 h aging. The t-value and p-value for two tailed T-test of shear strength in Chapter 7 for 100 h (31.97 ± 1.75 , MPa) and 500 h (26.53 ± 1.44 , MPa) aging are 5.740672416 and 0.000433611 , respectively. Since the $p\text{-value} < 0.01$, there is highly significant difference in the mean shear strength for 100 h and 500 h aging. Therefore, the shear strength of joints increases firstly with increasing the aging time then decreases as aging time rises to 500 h.